University of Alberta

Experiments on Sand Jets, Viscoplastic Fluids and Pumping

by

Jianan Cai

A thesis submitted to the Faculty of Graduate Studies and Research
in partial fulfillment of the requirements for the degree of

Doctor of Philosophy
in
Water Resources Engineering

Department of Civil and Environmental Engineering

Spring 2013
Edmonton, Alberta

Your file Votre référence
ISBN: 978-0-494-96412-5

Our file Notre référence
ISBN: 978-0-494-96412-5

To my daughter Chenyi,

Abstract

This study aims to improve our understanding of physical processes related to MFT and sand operations in tailings ponds. Laponite, a synthetic silicate that produces a transparent non-Newtonian gel, was used as a laboratory substitute of MFT.

This thesis first discussed the results of an experimental study of circular sand jets in air from nozzles of various sizes. The frontal speeds of the sand jets and the steady sand jet velocity accelerate due to gravity with negligible air resistance. The diameters of sand jets decrease but gradually approach an asymptotic value and the sand concentration in the jet decreases as the distance from the nozzle increases. Waves were observed at the periphery of the sand jet and some preliminary results of wave speed and wavelength were reported.

In second part of this thesis, experiments were carried out by depositing circular sand jets vertically into viscoplastic fluids. The deformation regimes of sand jets in the gel were investigated, including dispersed jetting, confined jetting and dripping. The penetration of sand drops at the gel surface was monitored and a simplified model was proposed to predict the yield stress. The yield-gravity parameter of the deformed sand drop in the gel was also computed.

Another set of experiments were performed to withdraw viscoplastic Laponite gel or water capped gel from a vertical circular pipe by a progressive cavity pump. The gel velocity field was computed from the images taken during

the process. Under the assumption of an axisymmetric flow condition, radial velocity was found to vary with the axial angle and maximum horizontal velocity occurs at a level below the intake pipe. For pumping a single layer of gel, an analytical solution was proposed to describe the radial velocity variation induced by pumping and it shows a good agreement with the experimental data when axial angle is less than 150°. For the selective withdrawal of water and gel, the interface deformation was inspected and critical submergence was found to be mainly controlled by the withdraw discharge. Water and gel discharges were discussed in terms of the subcritical and supercritical stages.

Acknowledgements

I would like to gratefully acknowledge the enthusiastic supervision of Dr. David Zhu and Dr. Nallamuthu Rajaratnam during my PhD study. I owe my thanks to Dr. Zhu for being a great supervisor and friend, being always caring and supportive. The hard working and research attitude of him is real life model to me and have been encouraging me all the way during my PhD. I am highly grateful to Dr. Rajaratnam for his patience, support and tremendous encouragement. His professional insight, passion for research has been always inspiring me and cheering me go forward.

This thesis study was funded by Oil Sands Tailings Research Facility (OSTRF), and I was also financial supported by the University of Alberta through the F.S. Chia scholarship and various teaching and research assistantships. I would like to express my greatest gratitude for their funding.

Many thanks to Perry Fedun, Chris Krath and Christine Hereygers for their invaluable technical support and help in the laboratory. My appreciation also goes to the other water resources graduate students who provided help.

Most of all I would like to thank all my family, who have always been giving me the endless love through my life. I specially want to thank my husband, Liming Zhao, for his encouragement and faith in me, and to my baby girl, Chenyi Zhao, for giving me so much joy and love, which always motivates me during my study.

Table of Contents

Chapter 1 General Introduction 1

1.1 Background 1

1.2 Thesis Outline 5

1.3 References 9

Chapter 2 Observations on Sand Jets in Air 12

2.1 Introduction 12

2.2 Experimental Setup 14

2.3 Results and Discussions 17

2.3.1 Jet frontal velocity U 18

2.3.2 Steady jet velocity V 19

2.3.3 Jet diameter d and sand concentration c 20

2.3.4 Waves 21

2.4 Summary 22

2.5 References 36

Chapter 3 Observations on Sand Jets in Viscoplastic Fluids 39

3.1 Introduction 39

3.2 Experiments 41

3.3 Results 43

3.3.1 Deformation regimes 43

3.3.2 Speed of the drop front 47

3.3.3 Sand drop penetration 49

3.3.4 Deformation size and yield-gravity parameter *51*

3.4 Summary 52

3.5 References 62

Chapter 4 Experimental Study on Pumping Viscoplastic Fluids 64

4.1 Introduction 64

4.2 Laboratory Methodology 66

4.2.1 Rheological properties *66*

4.2.2 Experiment design *68*

4.3 Results and Discussions 72

4.3.1 Stable state *72*

4.3.2 Velocity *73*

4.3.3 Deformed area *79*

4.4 The Numerical Solver 80

4.4.1 General description *80*

4.4.2 Discussions *82*

4.5 Summary 83

4.6 Notation 84

4.7 References 105

Chapter 5 Experimental Study on Pumping Water-capped Viscoplastic Fluids 108

5.1 Introduction 108

5.2 Experiment Design 110

5.3 Results and Discussions 113

5.3.1 Flow evolution *113*

5.3.2 Critical submergence *118*

5.3.3 Interface and discharge variation *122*

5.3.4 Velocity field *125*

5.3.5 Similarity to seepage flow *128*

5.3.6 Scour by water *129*

5.4 Summary 130

5.5 Notation 131

5.6 References 157

Chapter 6 Conclusions and Future Studies **160**

6.1 Conclusions 160

6.2 Recommendations 164

Appendix A Laponite Properties **166**

Appendix B PCP Efficiency **176**

References 180

List of Tables

Table 2-1 Experimental parameters 23

Table 3-1 Bingham plastic parameters of 3.0% Laponite gels. 54

Table 3-2 Experimental details and sand deformation types. 55

Table 4-1 Experimental parameters. 85

Table 5-1 Experimental parameters. 133

Table A-1 Rheological parameters for different Laponite samples based on the Bingham plastic model. 168

List of Figures

Figure 1-1 Reclamation methods proposed for oil sands tailings ponds. 7

Figure 1-2 A close view of a transparent sample of Laponite gel. 8

Figure 2-1 Experimental arrangement of sand jets in air. 24

Figure 2-2 Particle size distribution of three types of sands used in the experiments. 25

Figure 2-3 Pictures of sand jet fronts for d_e = 31.1 mm with time interval of 8 ms (2.58 m - 2.90 m down from nozzle exit). 26

Figure 2-4 Pictures of sand jets near the nozzle. 27

Figure 2-5 Mean velocities of sand jets at the nozzle. 28

Figure 2-6 (a) Frontal velocities of sand jets from different nozzles; (b) Variation of $(U^2-U_0^2)/g$ with L. 29

Figure 2-7 Comparison of steady and frontal velocities of a sand jet (d_e = 63.8 mm). 30

Figure 2-8 (a) Variations of steady sand jet diameters; (b) Dimensionless diameters along the steady sand jets. 31

Figure 2-9 Concentration variations along the steady sand jets. 32

Figure 2-10 Waves observed along sand jets with time interval of 4 ms. (a) for d_e = 63.8 mm (0.97 m – 1.32 m down from the nozzle exit); (b) for d_e = 31.1 mm (4.17 m - 4.47 m down from the nozzle exit). 34

Figure 2-11 Wave speed and wavelength along two steady jets. 35

Figure 3-1 The breakup regimes of a liquid jet into drops in another medium (Clift *et al.* 1978). 56

Figure 3-2 Example images of deformation types I to III of sand jets in Laponite gel. a) Run No. 1~3; b) Run No. 7~9; c) Run No.13~15; d) Run No. 10~12. 57

Figure 3-3 The frontal speed of sand drops in experiments. The solid markers are used for the lower viscous gel and the open markers are for higher viscosity. 58

Figure 3-4 The penetration of sand drop at the surface of gel (Run No 12 at a) 5 s, b) 15 s, c) 25 s, d) 35 s, e) 45 s and f) 47 s). 59

Figure 3-5 The simplification of the sand drop shape. 60

Figure 3-6 The relationship of buoyancy and the force due to yield stress of a sphere in gel. 61

Figure 4-1 Rheological measurements of 3.0% Laponite gel samples. 86

Figure 4-2 Yield stress measurements 3.0% Laponite samples. 87

Figure 4-3 Schematic of laboratory setup and the observation window. 88

Figure 4-4 Experimental raw images of Test No. 1 at 0 sec, 23 sec and 46 sec... 89

Figure 4-5 Velocity field of test No. 4 at different time during pumping. The contour plots of the velocity are in the unit of cm/s. 90

Figure 4-6 Variation of the field average velocity of all five tests. 91

Figure 4-7 Contour plots of steady velocity field and velocity contours: (a) ~ (e) is for Test No. 1 ~ No. 5 respectively. Velocity is in the unit of cm/s. 92

Figure 4-8 The Cartesian and spherical polar coordinate system. 93

Figure 4-9 Horizontal velocity components along the x-axis at different y locations for test No. 1 and No. 4. 94

Figure 4-10 The locations of maximum horizontal velocity components. 95

Figure 4-11 Radial velocity in the conical region of all five tests. 96

Figure 4-12 Radial velocity at different angular directions. 97

Figure 4-13 Radial velocity at different angles... 98

Figure 4-14 The variation of $f(\theta)$ with θ. 99

Figure 4-15 Maximum 2D shear rate contour plots for each experiment. 100

Figure 4-16 The beginning (a) and the end (b) of a random test. 101

Figure 4-17 A view of the unstructured mesh and the local refinement............. 102

Figure 4-18 Comparison between the experimental and simulated velocity profiles for Scenario 1. 103

Figure 4-19 Comparison between the experimental and simulated velocity profiles for Scenario 4. 104

Figure 5-1 Scheme of the experimental setup for water-gel pumping............... 134

Figure 5-2 The evolution of interface deformation of test No. 2 at a time interval of 30 seconds: a) 30 s, b) 60 s, c) 90 s, d) 119 s: the critical stage, e) 150 s, f) 180 s, g) 210 s, h) 240 s and i) 259 s: the end of the test. 135

Figure 5-3 The profiles of interface deformation in test No. 2 at different time corresponding to each sub-image in Figure 5-2.................................... 136

Figure 5-4 The estimated discharges of water and gel during pumping process in test No. 2, 3, 5 and 6. The blank blocks represent gel flow rate and the filled ones are for water. Labels are the percentage of water discharge. The superscript * indicates the critical stage. 138

Figure 5-5 Raw images taken at a) 0.1 s, b) 40, c) 80 s, d) 90 s, e) 120 s, f) 160 s, g) 200 s, h) 240 s, i) 280 s, j) 320 s, k) 360 s and l) 400 s for test No. 10. A ruler is attached to show the scale of these images. 139

Figure 5-6 The velocity contour plot of test No. 7 (in the unit of cm/s). 140

Figure 5-7 Variation of field averaged velocity of gel with time. The area used for calculation is the seeded area as shown in Figure 5-5. Two zones were blocked out: the area covered by the intake pipe and the area covered by water. 141

Figure 5-8 The drawdown curves of test No. 1 ~ 6 at the critical stage. 142

Figure 5-9 The dimensionless critical submergence is not dependent on the Froude number at the intake. 143

Figure 5-10 The depth of gel above the interface of gel and water varies with time. The filled symbols are used to indicate the critical stages of each test. The decreasing rate of this depth in subcritical stage is proportional to the pumping flow rate. 144

Figure 5-11 The profiles of the surface of gel at different time during withdrawal process in the test No. 3 of pumping single layer of gel. 145

Figure 5-12 Development of the interface of water and gel during pumping in test No. 10. 146

Figure 5-13 The vertical frontal velocity of water while travelling down in gel. 147

Figure 5-14 The interface profiles of water and gel at the critical stage in repeated test No. 7 and No. 9. 148

Figure 5-15 The discharges of gel and water change with the depth of gel above the interface........ 149

Figure 5-16 The locations of maximum horizontal velocity components. 150

Figure 5-17 Radial velocity at different angles........ 151

Figure 5-18 Variation of $f(\theta)$ with θ........ 152

Figure 5-19 The values of $f(\theta)$ change with the experimental process in test No. 10. Three stages presented here are: a) stable stage of withdrawing gel only; b) withdrawal of both gel and water; c) withdrawal of gel again after water has been all taken out by pump. All are compared with the result in chapter 4 for pumping from single gel layer........ 153

Figure 5-20 The relationship of average velocity and the hydraulic gradient. ... 154

Figure 5-21 The sketch of the water scouring in gel. 155

Figure 5-22 The erosion depth of water in gel increases linearly with the shear stress/rate of water. 156

Figure A-1 a) Single Laponite Crystal; b) Idealised Structural Formula........ 169

Figure A-2 Schematic stages of addiction Laponite to water........ 170

Figure A-3 Brookfield DV-II+ Programmable Viscometer........ 171

Figure A-4 The sets of vane spindles and disk spindles of Brookfield DV-II+ Viscometer........ 172

Figure A-5 a) A sample vane shear test measurement for 48 hours old 3.0% Laponite gel; b) The yield stress measurements of 2.5% and 3.0% Laponite gels........ 173

Figure. A-6 Laponite gel viscosity measurements: (a) 2.5% gel flow curve in different dispersion time; (b) 3.0% gel flow curve in different dispersion time. 174

Figure A-7 2.5% and 3.0% Laponite gels become more and more shear thinning with time. 175

Figure B-1 Comparison Flow rate measurements of pumping water and pumping pre-mixed 3.0% Laponite by different sizes of intake pipes. 179

Chapter 1 General Introduction

1.1 Background

Alberta's Oil Sands is the third-largest proven crude oil reserve in the world. In open-pit mining operations, hot water is used to separate bitumen from the sticky sand and the tailings are sent to the tailings ponds, where the sand settles to the bottom and water on the top is used for recycle. The middle layer is a mixture of water, clay, sand and residual bitumen, known as mature fine tailings (MFT) (Luo 2004). The challenge is that the fine solid particles in MFT do not settle within a reasonable timeframe. It can take up to 30 years to separate and dry out. As the area of the tailings ponds getting bigger, they present large impact on the landscape and environment (Government of Alberta).

Besides paste and some dry technologies, there are two other possible methods proposed to reclaim tailings ponds: water capping and soil capping (see Figure 1-1). In water capping, fresh water is added to cap MFT, and an end pit lake is created which is expected to support a healthy aquatic ecosystem. While in soil capping, sand and soil are used to cap the MFT and the reclaimed areas would be possible to support vegetation. Since the water capping is related to more environmental issues, the soil capping becomes a more favourable scheme to reclaim the tailings ponds after closure. In a case study of land reclamation over ultra-soft soil, the sand capping method is proved to be an effective method by Bo *et al.* (2005). However, the challenges of application in tailings ponds are to reduce the volume of the MFT and to increase the MFT's yield stress for soil capping. It requires a better understanding of the physical processes related to sand movement in MFT and the MFT pumping process as it is a way of manipulating and reducing the volume of the tailings.

Due to its high solids concentration (>30% by weight), MFT has a high viscosity but it cannot easily sustain any loads (Masliyah 2006). Banas (1991) reported that oil sands tailings sludge can be classified as a non-Newtonian fluid, which behaves like a Herschel-Bulkley model material in undisturbed state and a Bingham model fluid when remoulded. Based on this, MFT can be treated as a viscoplastic fluid, especially a Bingham plastic.

This thesis is a fundamental study of sand jets and non-Newtonian fluids. Potentially it could help advance our knowledge of sand deposition on soft foundation which is related to the sand capping process in oil sands tailings ponds reclamation. In this study, Laponite® is used to make non-Newtonian gels (see Figure 1-2). It is a rheological additive to make transparent clay, which also behaves like a viscoplastic fluid and can be made by mixing Laponite with tap water or deionized water at different concentrations (Southern Clay Products 2006). The properties of Laponite gels at various concentrations and suspension time can be found in Appendix A.

As an essential stage, sand streams have to travel through air before they can be deposited to a foundation. The behaviors of sand jets in air need to be investigated to better understand the sand capping process. Some works have been done regarding free falling granular jets, powder or particulate jets under gravity. where the fluctuations at the jet surface (Amarouchene *et al.* 2008), the liquid-like clustering behaviours (Möbius 2006; Royer *et al.* 2009) and the velocity profiles (Ogata *et al.* 2001) are studied. The first part of this study aims to provide more practical results of sand jets in air for large scale industry applications.

The phenomena of sand and slurry in different fluids have been extensively studied for their broad applications in science and technology. For sand jets in water, there are some early works concerning the spreading rate of the sand jet velocity (Brush 1962) and more recent studies about jet spreading rate using photography (Mazurek *et al.* 2002), the velocities of water and sand using Particle Image Velocimetry (Jiang *et al.* 2005) and the concentration and velocity profiles by fibre optical probe (Hall *et al.* 2010). Although there is a body of knowledge available surrounding the deposition of sand and slurry into water, little is known about deposition of sand and slurry into viscoplastic media. The second part of this study aims to broaden our understanding of sand movements as groups in non-Newtonian media. It could provide information for a comprehensive knowledge of sand capping on MFT.

Another challenge in oil sands tailings management is to transport tailings from the tailings ponds. The difficulty is how to efficiently withdraw MFT from the ponds without taking water from the surface layer. In stratified fluids, the minimum submerged depth for the intake in the lower layer fluid to not drain the upper layer fluid is known as "critical submergence". When non-dimensionalized with a characteristic parameter of the size of the intake, for instance, the internal diameter in case of a circular intake, the critical submergence is found to increase with the densimetric Froude number for bottom withdrawing (Harleman *et al.* 1959; Lubin and Springer 1967; Sharp and Parchure 1993; Davidian and Glover 1956; Wilhelms *et al.* 1985). Investigations have also been made to determine the critical submergence using soft computing technologies, such as Artificial Neural Network (ANN) and Neuro-Fuzzy model (Kocabaş *et al.* 2006, 2009). With respect to withdrawing non-Newtonian fluids, one of few studies is made by Zhou and Feng (2010a; 2010b). They observed the surface deformation of non-Newtonian fluid-gas sink flow and showed that the effects of elasticity on the critical submergence. The third part of this study applies an innovative experimental method to investigate the pumping process of lifting viscoplastic fluids alone or with water capping, which is to simulate a water layer sitting on top of MFT in the tailings ponds. The objective is to get a better understanding of selective withdrawal from two-layer non-Newtonian system. The results of the physical model study will also provide valuable data for calibrating and validating computational fluid dynamics (CFD) model. These CFD models can then be used to optimize the operations of tailings ponds.

1.2 Thesis Outline

This thesis includes studies of the observations on sand jets in air and in viscoplastic gels, as well as the withdrawal experiments of Laponite gel with or without water capping. All these subjects make up the four main chapters of this thesis, which follows a paper-based format.

Chapter 2 contains observations and discussions on experimental circular sand jets in air from nozzles of various sizes. A charge-coupled device (CCD) camera was engaged to capture the movements of sand jets free falling in air. The frontal velocity and steady velocity of sand jets were investigated. The diameter and sand concentrations of the jets were analysed based on the observation. Various particle sizes and nozzle sizes were used for a comprehensive understanding of the fundamentals of the phenomenon. This chapter provides a basic view of sand jets and is a preparation for the later ones.

Chapter 3 presents the results of experimental study on sand jets depositing into viscoplastic fluids. By changing dynamic parameters, sand jets were put into Laponite Gel with different rheological behaviors to study the deposition patterns, erosion and mixing properties. Three deformation regimes of sand jets in the gel were reported. The penetration of sand drops at the gel surface was monitored and a simplified model was proposed to predict the yield stress. Other aspects such as deformation size and yield-gravity parameter of the deformed sand drop in the gel were also computed.

Chapter 4 discusses the results of withdrawal tests of viscoplastic Laponite gel. The velocity field was studied and an analytical solution was proposed to describe the radial velocity variation induced by pumping. Numerical modeling was also conducted and compared with the experiments.

Chapter 5 is an extension of chapter 4. It presents the results of experimental withdrawal tests of water-capped gel, which is to mimic the water capping condition in the tailings ponds. The critical submergence of the pump intake, interface deformation process, velocity distribution and water scouring in gel were studied under different pumping discharges and for various intake sizes.

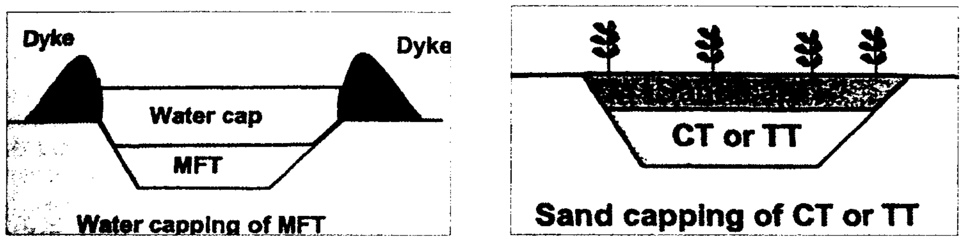

Figure 1-1 Reclamation methods proposed for oil sands tailings ponds.

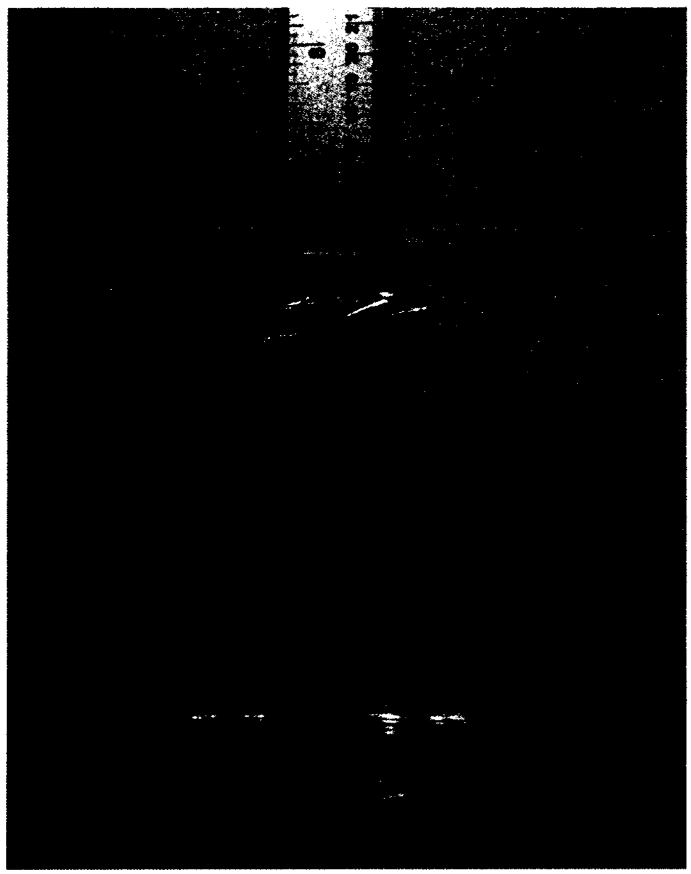

Figure 1-2 A close view of a transparent sample of Laponite gel.

1.3 References

Amarouchene, Y., Boudet, J. -., and Kellay, H. (2008). "Capillarylike fluctuations at the interface of falling granular jets." *Phys.Rev.Lett.*, 100(21),.

Banas, L. C. (1991). "Thixotropic behaviour of oil sands tailings sludge". M.Sc. University of Alberta, Canada.

Bo, M. W., Choa, V., and Wong, K. S. (2005). "Reclamation and soil improvement on ultra-soft soil." *Ground Improvement*, 9(1), 23-31.

Brush, L. M. (1962). "Exploratory study of sediment diffusion." *J.Geophys.Res.*, 67(4), 1427-1433.

Davidian, J., and Glover, J. E. (1956). "Development of the non-circulatory waterspout." *Proc Am Soc Civ Eng*, (HY 4), 1038.

Government of Alberta. "Alberta's Oil Sands." http://www.oilsands.alberta.ca/ 2013.

Hall, N., Elenany, M., Zhu, D. Z., and Rajaratnam, N. (2010). "Experimental study of sand and slurry jets in water." *J.Hydraul.Eng.*, 136(10), 727-738.

Harleman, D. R. F., Morgan, R. L., and Purple, R. A. (1959). "Selective withdrawal from a vertically stratified fluid." *Proc.Int.Assoc.Hyd.Res., 8th Congress, Montreal*, .

Jiang, J., Law, A. W., and Cheng, N. (2005). "Two-phase analysis of vertical sediment-laden jets." *J.Eng.Mech.*, 131(3), 308-318.

Kocabaş, F., Kişi, Ö., and Ardiçlioğlu, M. (2009). "An artificial neural network model for the prediction of critical submergence for intake in a stratified fluid medium." *Civ.Eng.Environ.Syst.*, 26(4), 367-375.

Kocabaş, F., and Ülker, S. (2006). "Estimation of critical submergence for an intake in a stratified fluid media by neuro-fuzzy approach." *Environmental Fluid Mechanics*, 6(5), 489-500.

Lubin, B. T., and Springer, G. S. (1967). "The formation of a dip on the surface of a liquid draining from a tank." *J.Fluid Mech.*, 29(PART 2), 385-390.

Luo, G. (2004). "Investigation of CT beneath MFT deposition for oil sands tailings disposal". M.Sc. University of Alberta, Canada.

Masliyah, J. H. (2006). "Tailings and water management." .

Mazurek, K. A., Christison, K., and Rajaratnam, N. (2002). "Turbulent sand jets in water." *Journal of Hydraulic Research*, 40(4), 527-530.

Möbius, M. E. (2006). "Clustering instability in a freely falling granular jet." *Physical Review E - Statistical, Nonlinear, and Soft Matter Physics*, 74(5),.

Ogata, K., Funatsu, K., and Tomita, Y. (2001). "Experimental investigation of a free falling powder jet and the air entrainment." *Powder Technol*, 115(1), 90-95.

Royer, J. R., Evans, D. J., Oyarte, L., Guo, Q., Kapit, E., Möbius, M. E., Waitukaitis, S. R., and Jaeger, H. M. (2009). "High-speed tracking of rupture and clustering in freely falling granular streams." *Nature*, 459(7250), 1110-1113.

Sharp, J. J., and Parchure, T. M. (1993). "Selective withdrawal using circular partly submerged intake structures." *J.Hydraul.Eng.*, 119(5), 615-627.

I. Southern Clay Products. (2006). "Product Bulletin/Laponite®." http://www.laponite.com/index.asp (March. 2008).

Wilhelms, S. C., Holland, J. P., and Smith, D. R. (1985). "Advances in Selective Withdrawal Through a Point Sink." *21st IAHR Congress,* Melbourne, Australia, 281-286.

Zhou, D., and Feng, J. J. (2010a). "Selective withdrawal of polymer solutions: Computations." *J.Non Newtonian Fluid Mech.,* 165(15-16), 839-851.

Zhou, D., and Feng, J. J. (2010b). "Selective withdrawal of polymer solutions: Experiments." *J.Non Newtonian Fluid Mech.,* 165(15-16), 829-838.

Chapter 2 Observations on Sand Jets in Air[1]

2.1 Introduction

Sand jets in air and in water have wide engineering applications. While there have been a number of experimental measurements on sand jets in water (e.g., Mazurek *et al.* 2002; Hall *et al.* 2009), the studies on sand particles in air have been mostly related to the particles driven by wind as in sand cloud blowing over a gravel surface (Dong *et al.* 2002), sand particle dispersion in a wind tunnel (Wang *et al.* 2006), as well as particulate solids pickup in gas flow in pipes (Rabinovich and Kalman 2007).

Though no studies have been reported on sand jets, there are a variety of works done regarding free falling granular jets/streams, powder or particulate jets. The surface of a granular jet in air is not smooth because of the interactions between the granular material and the air. The fluctuations at the jet surface are tracked by Amarouchene *et al.* (2008) and the experimental results suggest that the instability is related to the capillary force. The liquid-like clustering behaviour is observed in a freely falling granular jet of 100 μm glass spheres (Möbius 2006) as well as the granular jets of 130 μm glass grains (Royer *et al.* 2009), where the formation of clusters is shown to be correlated with the nanometre-range cohesive

[1] A version of this chapter has been published. Cai, J., Hall, N., Elenany, M., Zhu, D. Z., and Rajaratnam, N. (2010). "Observations on Sand Jets in Air." *J.Eng.Mech.*, 136(9), 1181-1186.

forces. Note that the nozzle diameters are only 4 mm in both studies of Möbius and Royer *et al.*, while in the real cases typically larger nozzles will be applied.

Ogata *et al.* (2001) have tested bigger sized nozzles, but the granular streams turns to be scattering in air further down the jet while the velocity profile is found to be uniform near the orifice but became disturbed afterward, similar to the numerical simulated results by Uchiyama (2004). However, in these two studies, the particle sizes are relatively bigger compared with other experiments where the falling jets broke into clusters (Möbius 2006; Royer *et al.* 2009). For the purpose of engineering applications, it would be worth to examine the behaviour of granular jets composed of natural particles produced from large scaled nozzles.

Moreover, the settling velocity of individual grain particulars and particles in air has been reported in a number of studies. The measured settling velocities of natural sand are significantly lower than those of spheres (Cui *et al.* 1983) as the particle shape is found to have a strong influence on the settling characteristics when turbulent boundary layers develop around the grains (Smith and Cheung 2003). Pye (1994) summarized that for particles of constant density, grain size and the particle shape are the most important factors determining the fall velocity. Le Roux (2005) provided empirical equations for predicting the settling velocities for both spherical and non-spherical particles in air. For sand jets in air, it is expected that the jet formation and particle interactions will have significant effects on the dynamics of sand particles and their speeds.

In this study, we made some observations on the motion of circular sand jets moving vertically downwards in air. In these experiments, sand jets were produced by a hopper located at the bottom of a conical sand feeder. High-speed digital video camera was used to observe these sand jets. For granular flow through hoppers, Rao and Nott (2008) concluded that the mass flow rate out of the hopper is approximately independent of the depth inside the hopper, provided the depth is large compared to the width of the exit slot; it only depends on the dimensions of the exit slot and the slope of the wall. Some recent studies also investigated the velocity field of granular materials inside a hopper with sharp walls (Ulissi *et al.* 2009) and the effect of a tube attached to a hopper (Grift and Crespi 2008).

2.2 Experimental Setup

The experimental arrangement is shown in Figure 2-1 wherein sand jets were produced by a conical hopper filled with dry sand. During all our experiments, the sand was maintained over a depth more than 0.4 m above the bottom of the hopper, and the slope of the hopper wall is around 31°. Experiments were done with the circular nozzle diameter d_e equal to 19.2 mm, 31.1 mm and 63.8 mm. The jet was created by removing a rubber bung from the 19.2 mm nozzle where a short 20 mm pipe was connected to the hopper, or by opening a spring loaded plate from underneath the 31.1 and 63.8 mm nozzles where no pipe was attached. All experiments have been performed with fine blasting sands from Sil Industrial Minerals Inc (http://www.sil.ab.ca/home.htm). They are sub-angular grain, crystalline silica sand with size D or D_{50} (50% finer than this size) equal to 0.21 mm and the density of 2,541 kg/m^3. To test the effects of particle sizes, a medium sand (D_{50} = 0.38 mm) and a coarse sand (D_{50} = 0.52 mm) were also used in the experiments with d_e = 19.2 mm. Figure 2-2 is a plot of the particle size distribution of the fine, medium and coarse sands used. With the attempt to evaluate the uniformity of the particle sizes, lognormal probability curves are applied to fit with the sand particle size distribution data, where the geometric standard deviations of each sand category is obtained as it is defined as

$$\sigma_g = \sqrt{\frac{D_{84.1}}{D_{15.9}}} = \frac{D_{84.1}}{D_{50}} = \frac{D_{50}}{D_{15.9}} \tag{2-1}$$

Here, $D_{84.1}$ and $D_{15.9}$ are the particle sizes at the 84.1% and 15.9% point of the cumulative axis of lognormal distribution curves. According to Breuser and Raudkivi (1991), if σ_g is less than about 1.35, the sand could be assumed to approximately uniform. Our fine and medium sized sands therefore can be treated as uniformly distributed, given their σ_g equal to 1.31 and 1.27, but the coarse sand is non-uniform because it has a σ_g = 1.47.

Primary details of these experiments are listed in Table 2-1, in which L_m is the maximum length of the jet in the experiments; V_e, m_e and R_e are, respectively, the mean velocity, the mass flux and the Reynolds number of the sand jet at the nozzle exit. The mass flux m_e was directly measured, from which the mean velocity and Reynolds number were calculated as, $V_e = m_e / \left[\pi (d_e/2)^2 (1-n)\rho_s\right]$, $R_e = V_e d_e / v_e$, where $n = 0.4$ is the porosity of the sand, ρ_s is the density of sand and υ_e is the kinematic viscosity of sand-air mixture at the nozzle exit, which was obtained from a formula by Wasp *et al.* (1977).

The sand jets from the nozzles were photographed using a PULNIX TM-1400CL camera at the rate of 30 frames per second for the 19.2 mm nozzle, and a REDLAKE IMAGING camera (MotionScope 1000S) at 250 frames per second for the 31.1 and 63.8 mm nozzles. One set of typical pictures at different times are shown in Figure 2-3. Pictures of the sand jets at varying distance from the nozzle were obtained by keeping the camera fixed, and raising the height of the sand hopper. From the photographical observations, the frontal speed U of these sand jets at different distances was obtained (Run No. 1 to No. 5). Over the entire distance of observation, the diameter of a sand jet in air can be estimated from pictures of the jet after the frontal head had passed the camera and became stable (Run No. 6 and No. 7). Figure 2-4 shows a close-up view of two sand jets near the nozzle.

2.3 Results and Discussions

In our experiments, four of the sand jets (Run No. 4 to No. 7) were directly produced from conical nozzles and their mean vertical velocities V_e were obtained from the measurements of sand mass over a given time. Figure 2-5 shows that the obtained V_e can be well approximated as $0.68\sqrt{gd_e}$. According to Rao and Nott (2008) the mean velocity V_e at the exit of a hopper can be estimated as $V_e = 0.74\sqrt{gd_e}$ provided the size of the granular material is relatively small compared with the size of the nozzle and the wall of the hopper is not very steep. Our result is close to the value estimated from $0.74\sqrt{gd_e}$ and the error is within 10%. For the sand jets from the 19.2 mm nozzle, the obtained V_e is increased by 15.6%. This difference is due to the attached short pipe in the 19.2 mm nozzle as reported by Rao and Nott (2008) that the flow rate of granular material from a hopper can be increased by the use of an extended pipe.

Given the contractions observed near the exits of two conical nozzles (d_e = 31.1 mm and 63.8 mm) as shown in Figure 2-3, we took the section $2d_e$ below the nozzle exit as the initial section of the sand jet as in orifice flows. The steady jet diameter and the jet frontal velocity at this initial section are defined as d_0 and U_0, respectively. However, for the 19.2 mm nozzle, the attached short pipe caused the sand jet to develop at the pipe exit, thus, $d_0 = d_e$. Note that in this study, the sand jets were considered to develop from this initial section.

2.3.1 *Jet frontal velocity* U

The observations on the front speed of the sand jets are shown in Figure 2-6(a). The front velocity U increases continuously with the length of the jet front from the initial section, L, in all experiments. The size of the sand particles (from 0.21 mm to 0.52 mm) does not appear to affect the speed of the front. If the air resistance is negligible, the sand particles will have an acceleration of g, thus $U = U_0 + gt$, and the velocity of the jet front U will be related to the travel distance L as follows:

$$U^2 - U_0^2 = 2gL \tag{2-2}$$

A plot of the present results in Figure 2-6(b) indicates that Equation (2-2) describes the observations very well; thus the jet front is being accelerated with negligible air resistance.

It would be of interest to compare the above velocity to the terminal velocity of single sand particles. For particles of ideally spherical shapes, the terminal velocity can be computed from the balance of the air resistance (i.e. drag force) and the particle weight in air. Standard drag coefficients for spherical particles can be found in most fluid mechanics textbooks. The terminal velocities of equivalent spheres, which have the same volume and weight of individual sand particles of D = 0.21mm, 0.38 mm and 0.52 mm, are found to be 1.44 m/s, 2.57 m/s and 4.21 m/s, respectively. According to the experimental study of Cui *et al.*

(1983). the settling velocities of natural sand particles of three sizes in our experiment can be estimated as 0.91 m/s, 1.68 m/s and 2.29 m/s. Notice that the sand front velocity in Figure 2-6(a) reaches over 10 m/s even for particles of D = 0.21 mm, which has individual particle terminal velocity of 0.91 m/s. It indicates that the effects of particle groups on reducing the air resistance are significant and within our observed distance, the air resistance can be neglected.

2.3.2 Steady jet velocity V

In our experiments, the diameter of the sand jets did not appear to be spreading due to any interaction with the surrounding air, so it is reasonable to assume that the velocity distribution in the sand jet might be approximately uniform as opposed to turbulent submerged jets where the distribution is approximately Gaussian (Rajaratnam 1976) or thin granular jets produced by Ogata *et al.* (2001). The steady jet velocities V at a distance x along the jet are measured using particle tracking method from the images taken with the high-speed camera, and the results are presented in Figure 2-7.

To compare with Ogata's results, we reduced the nozzle diameter to 2.3 mm which has an equivalent particle-nozzle size ratio of their setup. The diffusion is remarkable in the air for the jet from this nozzle whereas no obvious spreading observed for bigger nozzles. In our cases, the diameter of the nozzles is hundreds of times bigger than that of the sand particles. It could be the reason why our sand jets did not widen in the air.

For turbulent submerged jets (water jets in water or air jets in air), the frontal velocity is known to be about 0.61 times the maximum velocity of the corresponding steady jet at the same section (Rajaratnam and Yasmin 1992). For sand jets in air, this ratio is expected to be larger because of the reduced resistance to the movement of the front. This idea is tested also in Figure 2-7 wherein the velocity in the steady sand jet behind the front are plotted against the distance L from the initial section, along with the frontal speed variation, from the experiments for the largest nozzle (d_e = 63.8 mm). The comparison of steady and frontal velocities shows an interesting result that these two velocities follow the same line. Therefore what we have discussed for frontal velocity is also applicable for the steady velocities in sand jets.

2.3.3 *Jet diameter* d *and sand concentration* c

The variation of the jet diameter d of the steady sand jet at a distance x from the initial section is plotted in Figure 2-8(a), and the dimensionless value d/d_0 is plotted with the normalized distance x/d_0 in Figure 2-8(b). It is clear that d/d_0 decreases at the beginning and approaches a constant value of about 0.4, at a distance about $120d_0$ away from the initial section.

Assuming that the concentration of the sand as well as the velocity in the traveling sand jet is approximately uniform, the concentration c at any distance x from the initial uniform section can be obtained if the diameter of the jet is known and the mass flux is constant at different distances. Using the measured diameter,

c/c_0 is found to decrease with x/d_0 with a ratio of about 0.0025 (Figure 2-9) up to the length scale x/d_0 = 120, which corresponds to a porosity of about 0.68. The loss of sand particles in air as jet travelling down will decrease the mass flux, thus might affect the sand concentration.

2.3.4 Waves

In our experiments, waves were observed along the sand jets. Figure 2-10 shows two examples captured by the high-speed camera. The time interval between two sequential pictures is 1/250 s. In Figure 2-10(a), some sand particles were observed at one side of the jet, as a result of the ambient air having a horizontal velocity blowing from the left to the right in these pictures. In Figure 2-10(b), there was no ambient wind velocity, and the scatted particles were seen on both sides of the sand jet.

The traveling speed of these waves was obtained from their positions between two sequential images. A plot of the speed of waves is presented in Figure 2-11. It is shown that waves along the jet were travelling at almost the same speed as the jet itself. That is to say, the waves were stationary with respect to the carrying jet; once they were generated, the sand particles stayed together to keep the wave shape and accelerating with the jet. At different locations, various wavelengths were observed. The variation of wavelength λ along the jets is also plotted in Figure 2-11. For the 63.8 mm jet, λ is varying from the minimum value 5.24 cm at x = 131.9 cm to the maximum 6.87 cm at x = 180.4 cm; and for the

31.1 mm jet. it is in a range of 5.35 cm (x = 570.5 cm) to 9.00 cm (x = 489.2 cm). The frequency of the wave was then calculated by the wave speed over wavelength. Except for one set of images, the frequency is found to increase as jet traveling down, which indicates new waves were continuously generated as the stale waves moving downwards. While we have reported some preliminary observations on these waves, further study might be needed.

2.4 Summary

An experimental study of circular sand jets in air was conducted from three nozzles of diameter of 19.2 mm, 31.1 mm and 63.8 mm and sands with median size of 0.21 mm, 0.38 mm and 0.52 mm. The frontal speed of these sand jets increases with the distance of the front L with negligible air resistance and its variation is independent of the dimension of the nozzle and the size of the sand particles, but only depends on the acceleration purely due to gravity. However, the nozzle and particle size ratio also plays an important role that the jet could be spreading in air when the ratio is too small.

As these sand jets travel vertically downwards from the nozzle, their steady velocities increase while sand concentration decreases. Their diameters become smaller until approaching an asymptotic value at the location about $120d_0$ from the initial uniform section. Waves along the jets were found to travel as the same speeds as the jets themselves while the wavelengths are varying at different distances.

Table 2-1 Experimental parameters

Run No.	d_e (mm)	D_{50} (mm)	m_e (kg/s)	V_e (m/s)	R_e	L_m (m)
1	19.2	0.21	0.161	0.37	9066	2.56
2	19.2	0.38	0.161	0.37	9066	0.93
3	19.2	0.52	0.161	0.37	9066	0.96
4	31.1	0.21	0.427	0.37	14685	5.86
5	63.8	0.21	2.631	0.54	43969	5.75
6	31.1	0.21	0.427	0.37	14685	4.87
7	63.8	0.21	2.631	0.54	43969	5.93

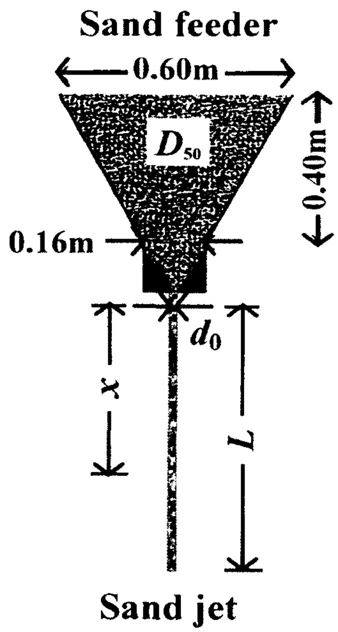

Figure 2-1 Experimental arrangement of sand jets in air.

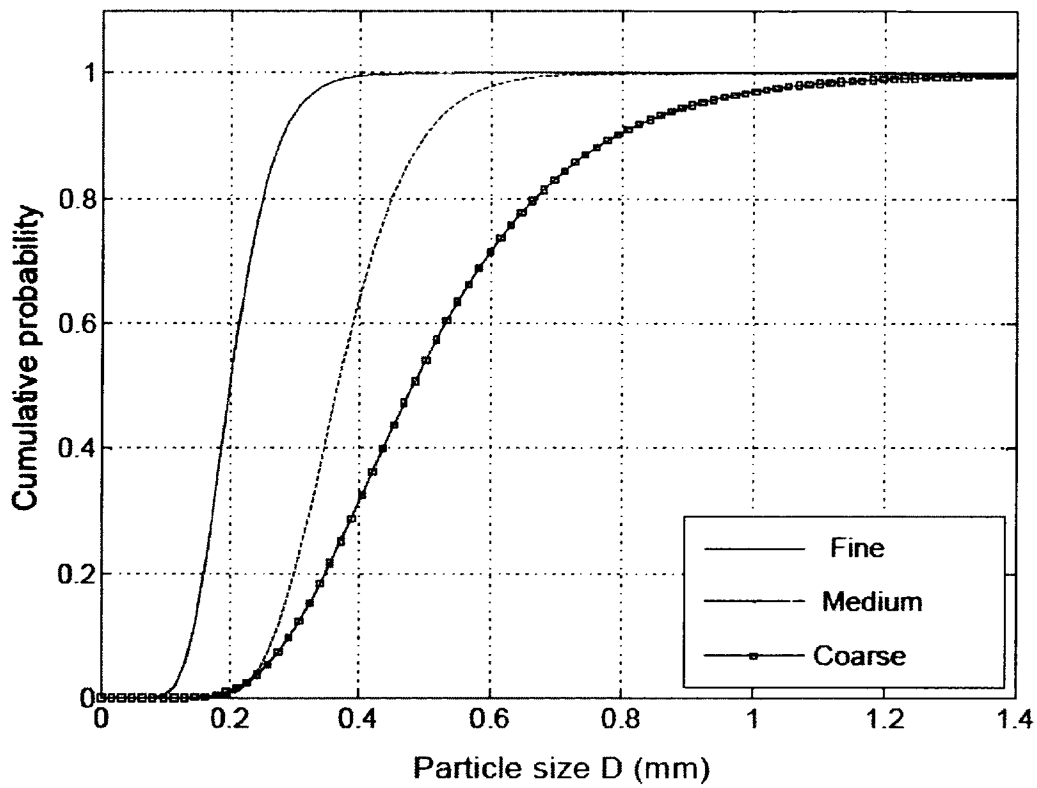

Figure 2-2 Particle size distribution of three types of sands used in the experiments.

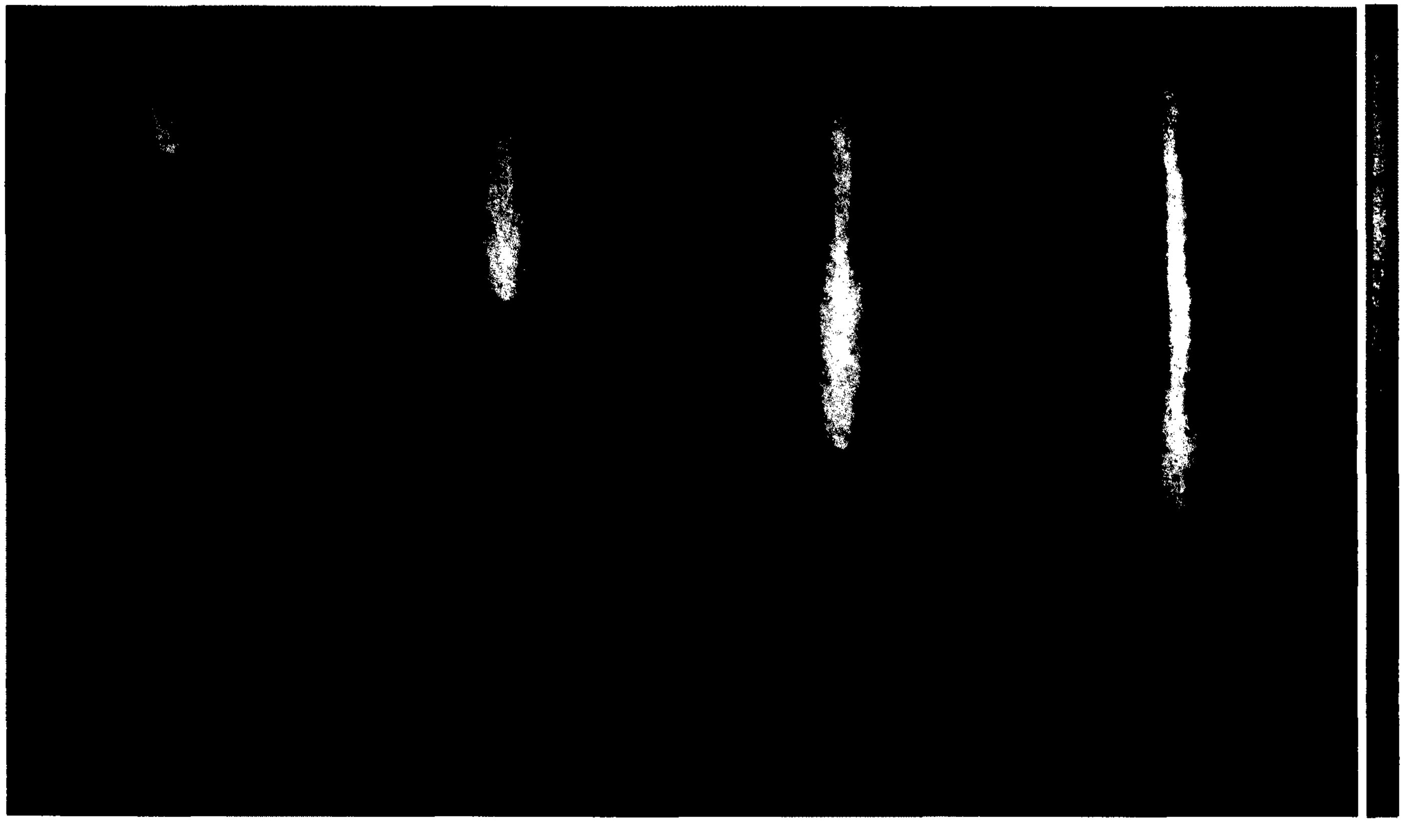

Figure 2-3 Pictures of sand jet fronts for d_e = 31.1 mm with time interval of 8 ms (2.58 m - 2.90 m down from nozzle exit).

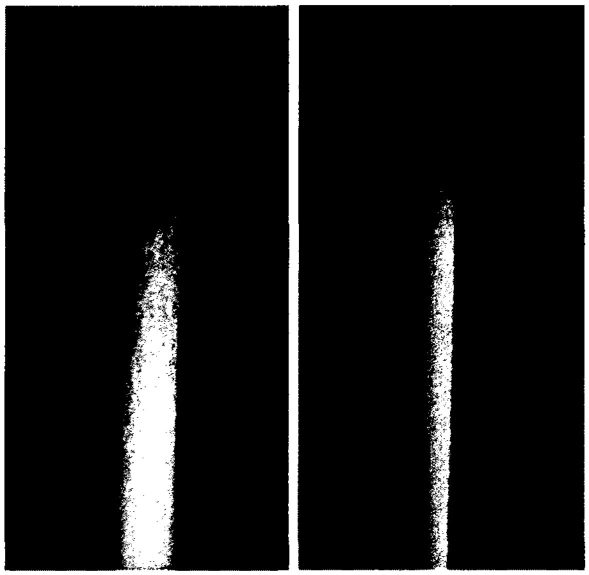

(a) d_e = 63.8 mm (b) d_e = 31.1 mm

Figure 2-4 Pictures of sand jets near the nozzle.

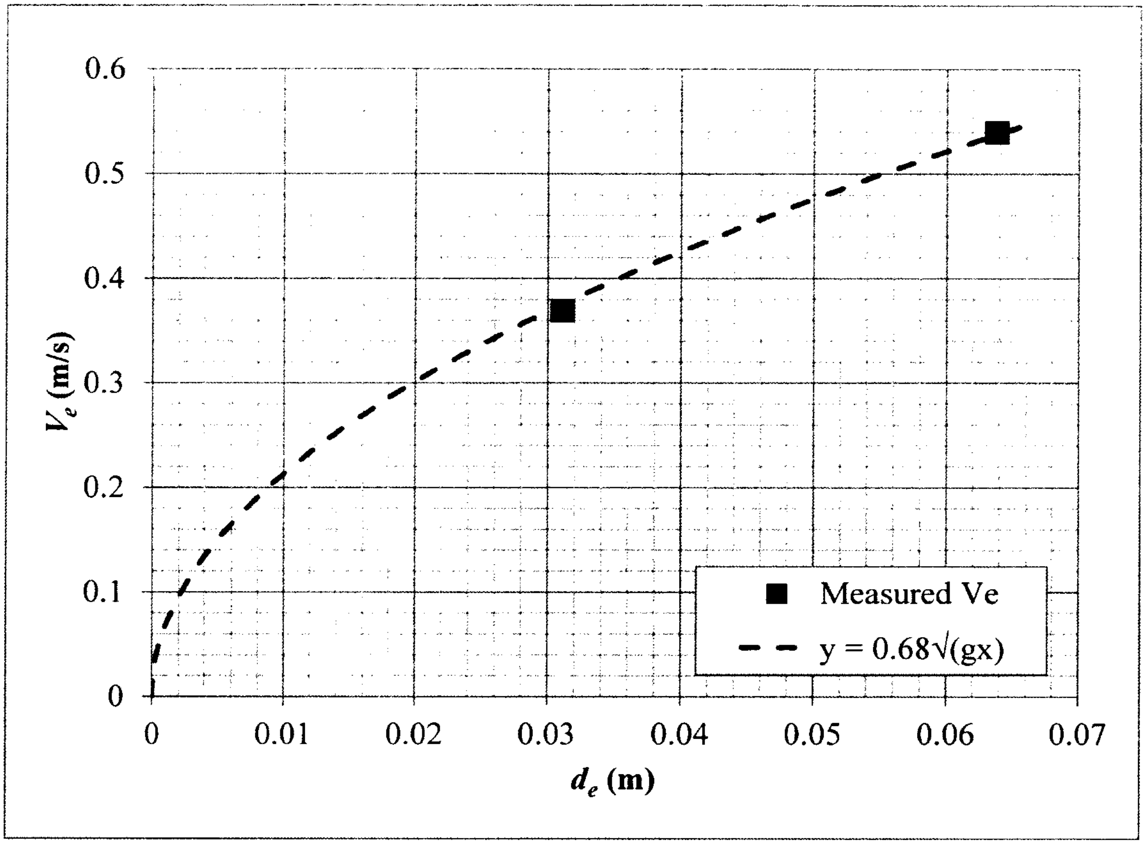

Figure 2-5 Mean velocities of sand jets at the nozzle.

(a)

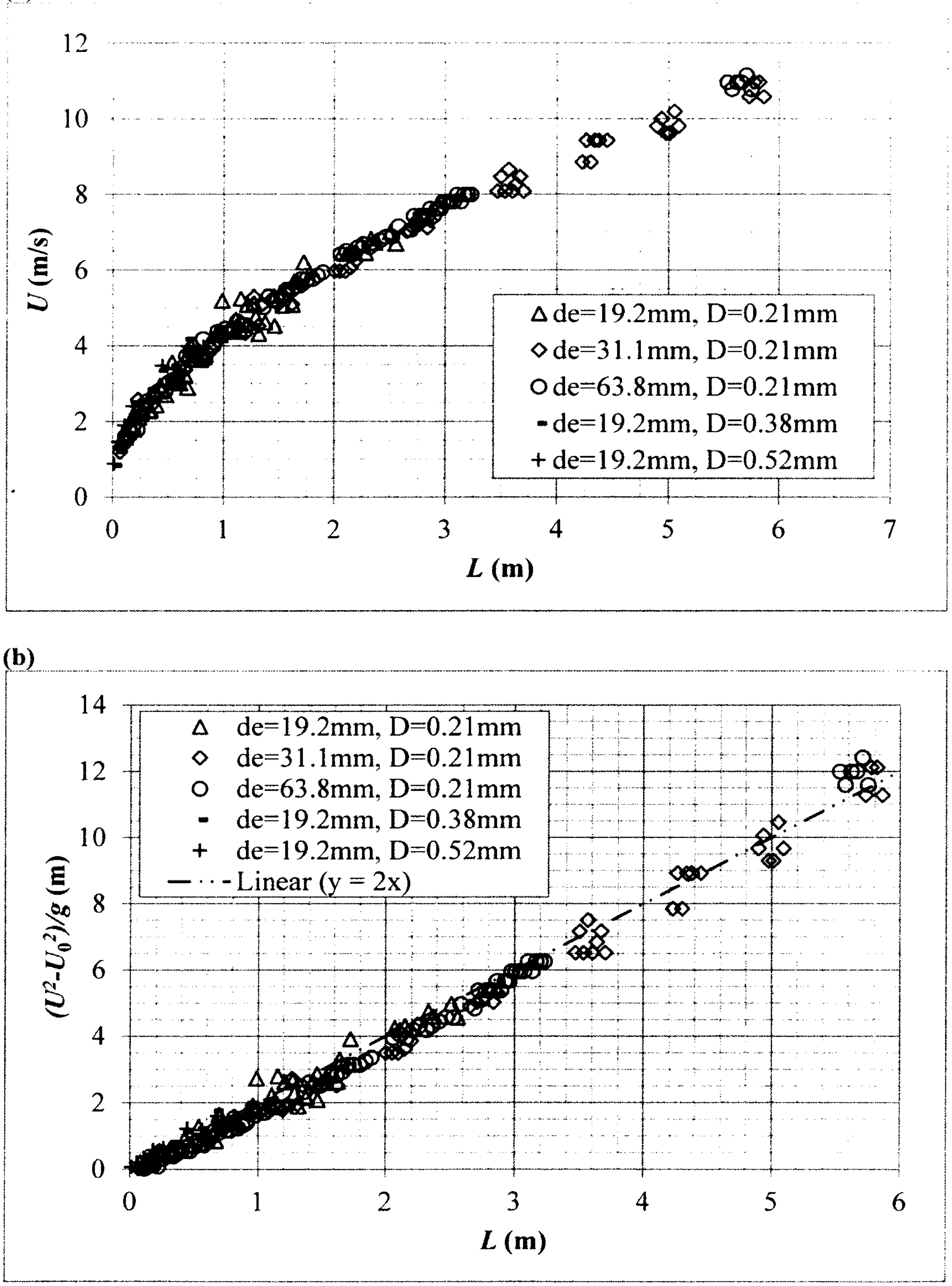

Figure 2-6 (a) Frontal velocities of sand jets from different nozzles; (b) Variation of $(U^2-U_0^2)/g$ with L.

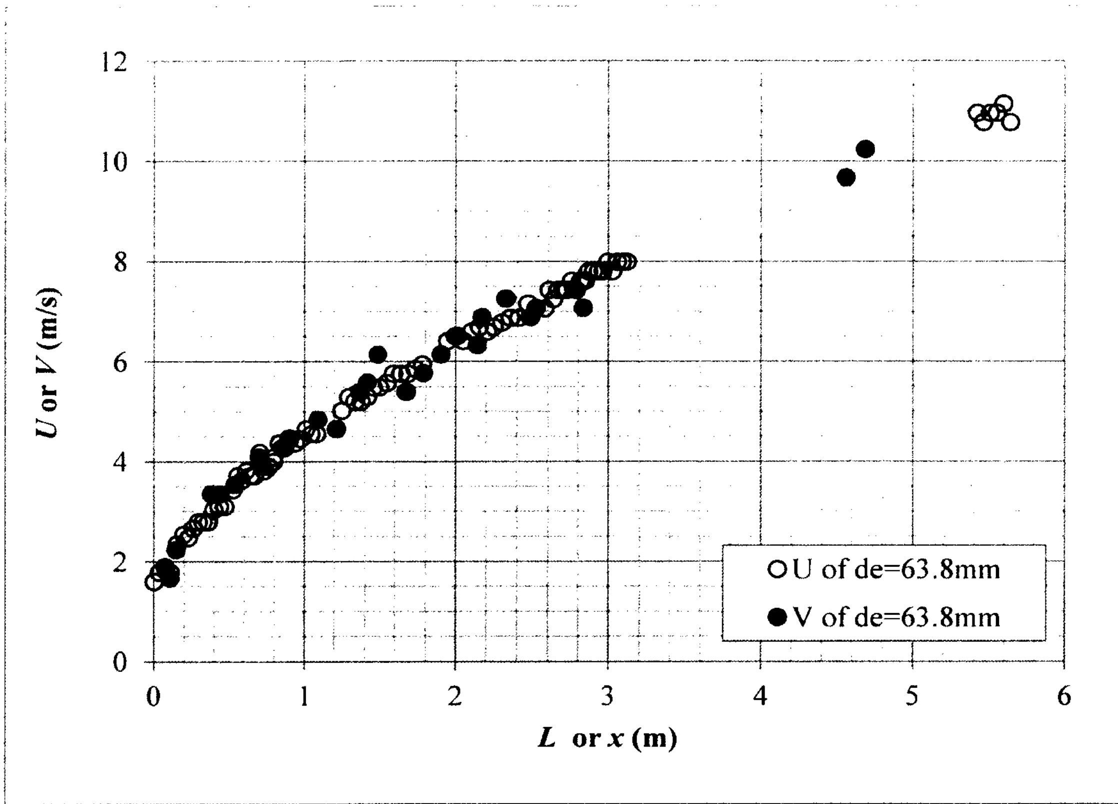

Figure 2-7 Comparison of steady and frontal velocities of a sand jet (d_e = 63.8 mm).

(a)

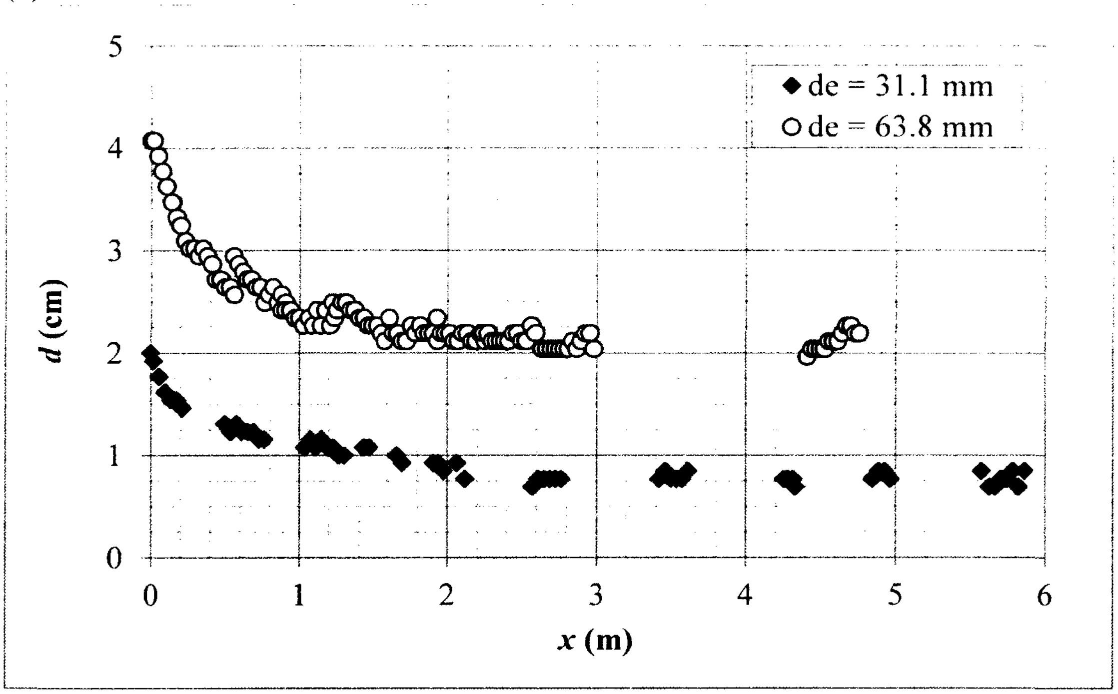

(b)

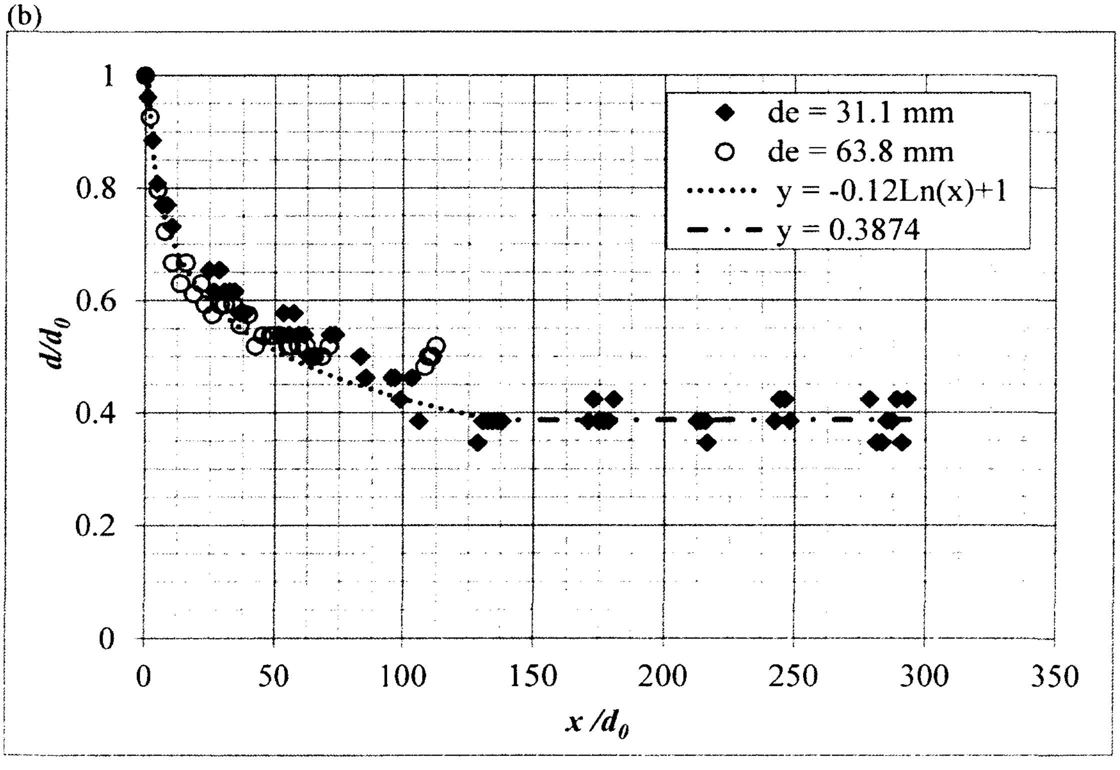

Figure 2-8 (a) Variations of steady sand jet diameters;

(b) Dimensionless diameters along the steady sand jets.

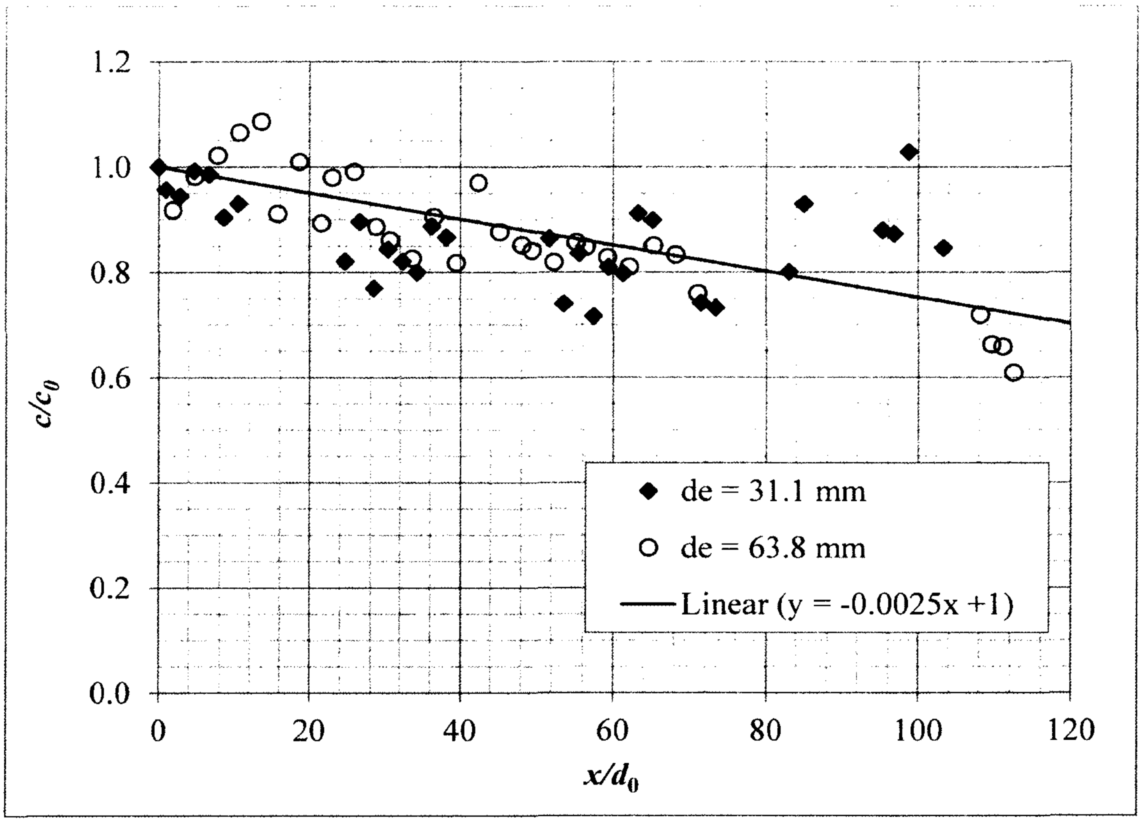

Figure 2-9 Concentration variations along the steady sand jets.

(a)

(b)

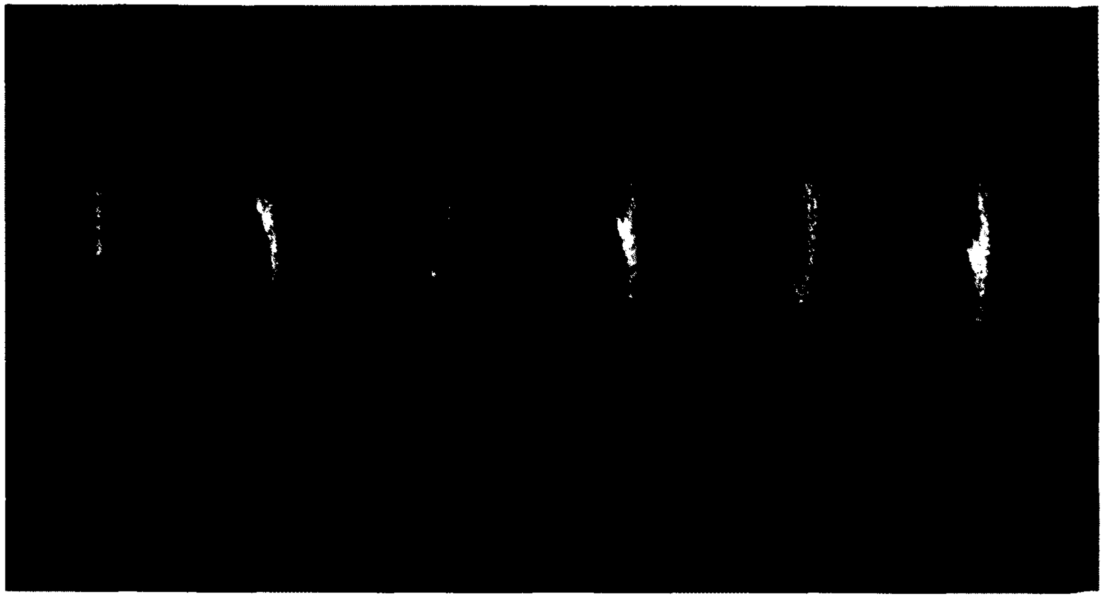

Figure 2-10 Waves observed along sand jets with time interval of 4 ms. (a) for d_e = 63.8 mm (0.97 m – 1.32 m down from the nozzle exit); (b) for d_e = 31.1 mm (4.17 m - 4.47 m down from the nozzle exit).

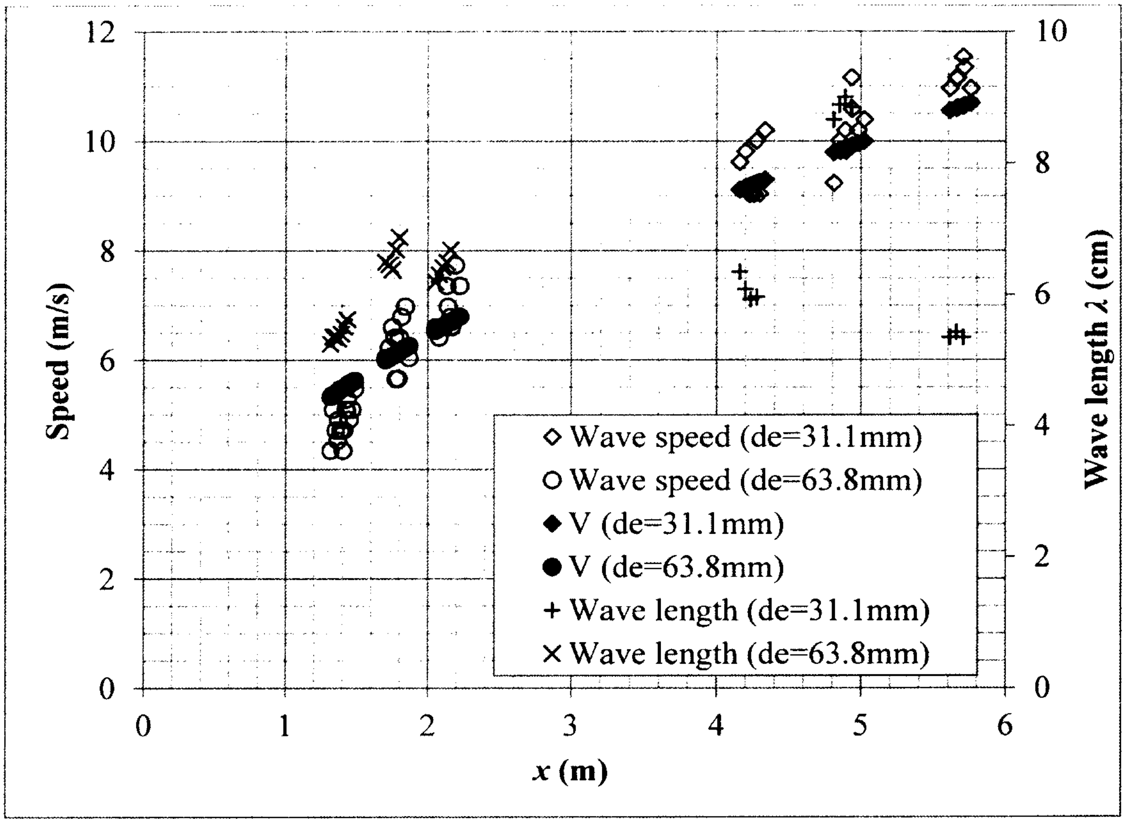

Figure 2-11 Wave speed and wavelength along two steady jets.

2.5 References

Amarouchene, Y., Boudet, J., and Kellay, H. (2008). "Capillarylike fluctuations at the interface of falling granular jets." *Phys.Rev.Lett.*, 100(21),.

Breusers, H. N. C., Raudkivi, A. J., and International Association for Hydraulic Research. (1991). *Scouring.* A.A. Balkema, Rotterdam, The Netherlands; Brookfield, Vt.

Cui, B., Komar, P. D., and Baba, J. (1983). "Settling velocities of natrual sand grains in air." *Journal of Sedimentary Petrology,* 53(4), 1205-1211.

Dong, Z., Wang, H., Liu, X., Li, F., and Zhao, A. (2002). "Velocity profile of a sand cloud blowing over a gravel surface." *Geomorphology,* 45(3-4), 277-289.

Grift, T. E., and Crespi, C. M. (2008). "Estimation of the flow rate of free falling granular particles using a Poisson model in time." *Biosystems Engineering,* 101(1), 36-41.

Hall, N. A., Elenany, M., Zhu, D. Z., and Rajaratnam, N. (2009). "Experimental study of sand and slurry jets in water." *Submitted to ASCE Journal of Hydraulic Engineering.*

Le Roux, J. P. (2005). "Grains in motion: A review." *Sediment.Geol.,* 178(3-4), 285-313.

Mazurek, K. A., Christison, K., and Rajaratnam, N. (2002). "Turbulent sand jets in water." *Journal of Hydraulic Research,* 40(4), 527-530.

Möbius, M. E. (2006). "Clustering instability in a freely falling granular jet." *Physical Review E - Statistical, Nonlinear, and Soft Matter Physics,* 74(5),.

Ogata, K., Funatsu, K., and Tomita, Y. (2001). "Experimental investigation of a free falling powder jet and the air entrainment." *Powder Technol,* 115(1), 90-95.

Pye, K. (1994). "Shape sorting during wind transport of quartz silt grains - Discussion." *Journal of Sedimentary Research A,* 64 704-705.

Rabinovich, E., and Kalman, H. (2007). "Pickup, critical and wind threshold velocities of particles." *Powder Technol,* 176(1), 9-17.

Rajaratnam, N. (1976). *Turbulent Jets.* Elsevier scientific publishing company, New York.

Rajaratnam, N., and Yasmin, N. (1992). "Fronts of circular turbulent jets." *Proceedings of the Institution of Civil Engineers: Water, Maritime and Energy,* 96(1), 59-61.

Rao, K. K., and Nott, P. R. (2008). *An introduction to granular flow.* Cambridge University Press, Cambridge; New York.

Royer, J. R., Evans, D. J., Oyarte, L., Guo, Q., Kapit, E., Möbius, M. E., Waitukaitis, S. R., and Jaeger, H. M. (2009). "High-speed tracking of rupture and clustering in freely falling granular streams." *Nature,* 459(7250), 1110-1113.

Smith, D. A., and Cheung, K. F. (2003). "Settling characteristics of calcareous sand." *J.Hydraul.Eng.,* 129(6), 479-483.

Uchiyama, T. (2004). "Numerical analysis of particulate jet generated by free falling particles." *Powder Technol,* 145(2), 123-130.

Ulissi, F., Ippolito, I., and Calvo, A. (2009). "PIV Technique applied to granular flows in hoppers." *Journal of Physics: Conference Series*, 166.

Wang, H. T., Zhang, X. H., Dong, Z. B., and Ayrault, M. (2006). "Experimental determination of saltating glass particle dispersion in a turbulent boundary layer." *Earth Surf.Process.Landforms*, 31(14), 1746-1762.

Wasp, E. J., Kenny, J. P., and Gandhi, R. L. (1977). *Solid-liquid flow slurry pipeline transportation.* Trans Tech Publications, Clausthal, Ger.

Chapter 3 Observations on Sand Jets in Viscoplastic Fluids[2]

3.1 Introduction

Sand jets depositing into non-Newtonian fluids have a number of industrial and engineering applications. One example is the reclamation of oilsands tailings ponds using soil capping: sand and soil are used to cap the mature fine tailings, a by-product of oil sand industry, which can be classified as a viscoplastic, especially a Bingham plastic fluid (Banas 1991). Another application is sand deposit into soft mud at the bottom of rivers or estuaries, which is also one type of non-Newtonian fluid. Though we know much about liquid jet breakup in another liquid and sand depositing into water, there is limited information available regarding sand jets in non-Newtonian materials.

A number of studies examined Newtonian liquid jets into Newtonian or non-Newtonian liquids (Kitamura and Takahashi 1982; Kitamura *et al.* 1982; Dravid *et al.* 2008), including jet instabilities, breakup length, drop formation and sizes. Clift *et al.* (1978) schematically described the breakup of a liquid jet into drops in another medium by several breakup modes (Figure 3-1). Depending on the flow rate at the nozzle, drops can be formed by dripping, jetting or

[2] A version of this chapter has been published. Cai, J., Zhu, D. Z., and Rajaratnam, N. (2012). "Observations on sand jets in viscoplastic fluids." *Theor.Appl.Mech.Lett.*, 2(5), 052001.

atomization. With respect to drops formed by particles or fluid-particle suspensions, one of few studies found in the literature was done by Furbank (2004). He considered three different conditions for drop formation by particulate suspension: dripping, transition from dripping to jetting, and jetting. Nicolas (2002) used three non-dimensional numbers to define different regimes of gravity-driven dense suspension jets into Newtonian fluids. The parameters involved are a dimensionless number indicating the ratio of gravity force to the viscous force, a particle Reynolds number and Stokes number. In the case of granular material discharging into non-Newtonian, no studies have been reported.

For sand-water two-phase jet, although there is a body of knowledge available surrounding the deposition of sand and slurry into water (Jiang *et al.* 2005; Hall *et al.* 2010), little is known about deposition of sand and slurry into viscoplastic media. Moreover, most of the studies were aimed at investigating the behaviour of single particles or suspensions in viscoplastic fluids (Ferroir *et al.* 2004; Merkak *et al.* 2006); and few studies analyzed agitated movements or particle movements as groups.

Because of the existence of the yield stress, an undisturbed viscoplastic medium has capacity to support the weight of an embedded particle. Once the buoyancy force exceeded the force due to the yield stress, the embedded particle will start moving, which can be described by a yield-gravity parameter, Y_G. The critical values of Y_G to define the balance between gravity and yield stress have been reported ranging from 0.04 to 0.212 by different researchers (Chhabra 2007). If granular particles are continuously deposited into a viscoplastic fluid as a granular jet, the behaviour is expected to be different from one single particle due to the particle-fluid and particle-particle interactions.

In this study, circular sand jets were deposited vertically into viscoplastic fluids. The size and height of the jet, the viscosity of the fluid were varied to study different deformation regimes. The penetration process, the frontal speed and the yield-gravity parameter of the deformed sand drop in the gel were also reported.

3.2 Experiments

Laponite® dispersion is used to make the viscoplastic gel for the experiments. Laponite is a rheological additive to make transparent clay, which also behaves like a viscoplastic fluid and can be made by mixing Laponite with water. As described in Appendix-A, Laponite powder was mixed with demineralised water to form a 3.0 wt% transparent gel. With different dispersion time, the rheology of the gel varied. However, Bingham plastic non-Newtonian model can be used to fit all obtained rheological data.

$$\tau = \tau_0 + \mu_p \dot{\gamma} \tag{3-1}$$

wherein τ and $\dot{\gamma}$ are respectively the shear stress and the shear rate of flow; τ_0 is the yield stress and μ_p is known as plastic viscosity. The best fitted parameters for different samples are presented in Table 3-1, in which τ_0' is the measured value of the yield stress. A set of experiments were conducted in a rectangular glass tank, 32 cm wide, 46 cm long and 50 cm deep. The tank was filled with 3.0% Laponite gel up to 31.5 cm.

Sand jets were set up to discharge vertically into the gel. These jets were produced by a hopper fixed at a range of heights and the outlet nozzle size was varied. The hopper was initially fully filled with dry silica sand from Sil Industrial Minerals, with a median diameter D_{50} of 206 ± 54 μm and a density ρ_s of 2,541 kg/m^3. The sand jet was formed by releasing the stop at the bottom of the hopper, and allowing the sand free falling into quiescent gel in the tank.

Depending on the rheology of the gel and the momentum flux of the grains, these sand jets would penetrate the gel or build mounds over the gel surface then sink as droplets. Different deformation types were observed and quantified by tracking the images of the whole process using a CCD camera (PULNIX TM-1400CL). It has a resolution of 1392×1040 pixels, and the recording rate was set to 30 frames per second.

According to Rao and Nott (2008), the mass flux of granular material is mainly controlled by the exit size of a sand feeder. In our case, it is the diameter of the exit of the hopper. Discharging from three nozzles of different sizes, the mass flux of sand jet was obtained by collecting sand grains at the exit of the hopper with increasing time intervals. Assuming the porosity of sand is 0.4, the velocity of sand jet at the exit can be computed. The velocity of a sand jet when it deposited into the gel were then calculated based on the experimental observation by Cai *et al.* (2010). All experimental details are listed in Table 3-2, where V_e, d_e and V_0, d_0 are respectively the velocity and diameter of a sand jet at the exit of the hopper and the surface of the gel; H is the distance between the bottom of the hopper and gel surface.

In our experiments, the sand jet either accumulated on the gel surface followed by the deformation or continuous jetting in the gel depending upon the age (i.e., rheology) of the gel and the height of the jet. The observed deformation types (see Figure 3-2) for a sand jet depositing into Laponite gel include: I - dispersed jetting; II - confined jetting; and III- dripping. For type I, gel was entrained by sand jet which spreads out while shooting down. Type II was characterized by jet with connected drops or smooth confined jet. In type III, sand jets were broken down into single drops or drops followed by a satellite.

3.3 Results

3.3.1 Deformation regimes

Granular particles in motion sometimes are similar to those of flowing fluids. The deformation types shown in our experiments are in agreement with the tendency of liquid-liquid breakup described by Clift *et al.* (1978). It is changing as the mean entry velocity or the sand discharge increases. The sand jet broke up in the gel and formed drops when it was at low velocity from smaller nozzle and the viscosity of the gel was high (type III). However, the jet penetrated the gel as a confined jet in the case of relatively high velocity and bigger nozzle (type II). Finally it entrained and mixed with less viscous gel while the velocity was very high and the nozzle was much bigger (type I).

Figure 3-2 contains images of different deformation types, wherein groups (a) to (c) demonstrate the impact of entrance velocity and the nozzle diameter. These three sets of sand jets were all performed in the lower viscous gel (Experiment run No. 1 ~ 3, 7 ~ 9, 13 ~ 15). They were individually from the nozzle with a diameter of (a) 9.6 mm, (b) 5.4 mm and (c) 3.3 mm. So within each group, the sand jets were from the same nozzle, but the distance between the exit of the nozzle and the surface of the gel was varied. For group (a) 1~3, with the distance decreasing and the entrance velocity slowing down, it changed from a dispersed jet with tremendous mixing, to an oscillating non-axisymmetric jet, further to a confined jet without any interaction with the surrounding gel. In this case, the particle Reynolds number is defined as $Re_p = \rho_g V_0 D_{50}/\mu_g$, where ρ_g and μ_g are respectively the density and the viscosity of the gel. This dimensionless number can be used as a criterion to identify the transition from dispersed jet to confined jet (Nicolas 2002). When the inertial force dominates over viscous force in the scale of the particle size, or $Re_p > 1$, the jet will spread out and mix with the surrounding fluid; otherwise, it maintains the cylindrical shape. For Newtonian fluid, the viscosity is a constant and the particle Reynolds number can be easily computed. However, for a Bingham plastic fluid, the viscosity changes with the shear rate of the flow and the calculation is complicated. In group (b), with a medium size nozzle, d_e = 5.4 mm, we observed confined jetting when the jet was positioned higher, in contrast drops started to form for a lower jet due to the lack of momentum to penetrate the gel at its surface. For sand jets from the 3.3 mm nozzle, only drops were noticed as the jet entered the gel as shown in Figure 3-2(c). In addition, the viscosity of the gel also plays an important role in the deformation of sand jet. In viscous gel, sand jets were more likely deformed into drops (Figure 3-2 (d)), while for lower viscosity the jet was continuing from the air in the gel (Figure 3-2 (b)).

Bingham plastic fluid is characterized by the existence of the yield stress, which has to be overcome before the flow starts to shear. The critical status for sand stream whether jetting into the gel (type I and II) or creating drops (type III) depends on the balance of the momentum flux of the sand grains and the friction due to the gel. If we assume that the sand jet was a cylinder with a diameter of d_0 when its head hit the gel surface, and it dug a path through the gel keeping the same size, the forces applied on the sand cylinder in the gel, with a length of l, a velocity of V and a porosity of Φ, include the thrust from the incoming jet F_t, the negative buoyancy F_b, and the friction of gel acting on the sand jet surface, F_t. $\dot{m}$ is the mass flux of the sand jet, then

$$F_t = \dot{m}V_0 - \dot{m}V \tag{3-2}$$

$$F_b = \frac{\pi}{4} d_0^2 l[\rho_g - (1 - \Phi)\rho_s]g \tag{3-3}$$

$$F_\tau = \pi d_0 l\left(\tau_0 - \mu_p \frac{dV}{dr}\right) \tag{3-4}$$

where r is the transverse direction. When the three forces balanced out,

$$F_t = F_b + F_\tau \tag{3-5}$$

the maximum penetration depth or breakup length of the sand jet l_m in gel was reached, and the velocity of the jet become zero. So V = 0 m/s, dV/dr = 0, ρ_g = 1,003 kg/m^3, ρ_s = 2,541 kg/m^3, Φ = 0.4, and g = 9.81 m/s^2. Combine Equation (3-2) ~ (3-5), l_m can be solved as

$$l_m = \frac{\dot{m} V_0}{\pi d_0 (\tau_0 - 1279 d_0)} \tag{3-6}$$

The final results of l_m for each jet are all listed in Table 3-2. It shows the same trend of the jet breakup length as in Figure 3-1. Although l_m is just a conceptual parameter, it can be used as an index to classify the behavior of sand jets in gel. When l_m is below 10 cm, the sand jets will form a drop at the gel surface (type III); as l_m increases up to more than 180 cm, sand jets will continuously develop in gel which comes into type II; but it decreases again when type I appears.

3.3.2 *Speed of the drop front*

In the experiments with the formation of sand drops. the front of the penetrated sand drop in the gel can be located in the images. and the speed of the front was calculated based on the difference in two frames in sequence. In this way, the front speed was tracked during the process of all these tests.

Laponite is a Bingham plastic non-Newtonian fluid; hence it can support some weight of sand at its surface before the yield stress was overcome. For the deformation type III, as the jet pouring more and more sand grains, a small pile was built up and the contact area was bent by it to form the front of a sand drop in the gel. However, once the maximum bearing force was achieved, the drop fell suddenly and accelerated in the gel. As a result, the speed of the front was close to 0 at the beginning, followed with an abrupt rise in the middle as demonstrated in Figure 3-3. However, due to the boundary effect, the frontal speed decreased again when the drop approaching the bottom of the container. Within the limit of the depth of the tank, the terminal velocity of the sand drop was not reached. In Figure 3-3, open markers are used to denote the sand jets deformed in gel with higher viscosity. It shows all sand drops, no matter what the size is, followed the same pattern. Their fronts started to speed up at a depth of 11 cm, and then slowed down at 18 cm.

Based on the discussion of Chhabra (2007) in his book, the drag coefficient C_D of a sphere in viscoplastic fluid can be calculated as $C_D = 34 / Q_{AS}$, where $Q_{AS} = \mathrm{Re}_B/(1+\frac{7\pi}{24}Bi)$. The Bingham Reynolds number is defined as $\mathrm{Re}_B = \rho_g vD/\mu_p$, where ρ_g is the density of the gel; D is the diameter of the sand drop. Bingham number $Bi = \tau_0 D/\mu_p v$. So if the drop is idealized as a sphere, the drag force acting on it is

$$F_D = \frac{1}{8}\pi D^2 \rho_g v^2 C_D = \frac{17}{96}\pi D\left(24\mu_p v + 7\pi D\tau_0\right) \tag{3-7}$$

The Buoyancy is

$$F_B = \frac{\pi}{6}D^3\left[\rho_g - (1-\Phi)\rho_s\right]g \tag{3-8}$$

The initial velocity of the drop is negligible compared with the velocity during the acceleration period. The kinetic energy of the drop gained during a distance l is equal to the work done by the drag and the buoyancy, which are both in the opposite direction of the velocity. So the energy equation turns out to be

$$\left(-F_B - F_D\right)l = \frac{1}{2}mv^2 = \frac{1}{6}\pi D^3(1-\Phi)\rho_s v^2 \tag{3-9}$$

Combine Equation (3-7), (3-8) and (3-9), it becomes

$$v^2 + \frac{51\mu_p}{D^2(1-\Phi)\rho_s} vl + \left[\frac{119\pi\tau_0}{8D(1-\Phi)\rho_s} + \frac{2\rho_g g}{(1-\Phi)\rho_s} - 2g\right] l = 0$$

The velocity of the sand drop, v, is found to increase with the distance l once it starts to accelerate, which agrees with the results presented in Figure 3-3.

3.3.3 Sand drop penetration

One example of sand drop penetrating through the gel is presented in Figure 3-4. The penetration process is shown at every 10 seconds starting from 5 s to 45 s and then at 47 s, for which the 0 s is taken when the front of the sand jet entered gel. In this run, acceleration of the sand drop front happened at 45 s, when the yield stress acting on the drop surface was exceeded by the negative buoyancy. These images indicate that the deformation developed in three stages. At the first stage, the front of the sand drop began to form and grew wider while slowly moving down until the maximum diameter was obtained. The first three images a) to c) in Figure 3-4 represent this period. The next two images d) and e) describe the second stage, during which the sand drop narrowed down but still sank gradually till the third stage started. In this final stage, the sand drop accelerated in a sudden and pinched off rapidly.

To simplify the process, a hemisphere is used to represent the shape built during the first stage, and a reversed cone is assumed to act for the volume formed in the second stage. The diameter of the hemisphere is defined as the deformation size of the sand jet, and denoted as D. Other definitions are shown in Figure 3-5. Then the force due to the yield stress for these two shapes is

$$F_{\tau_0 1} = \int_0^{\frac{\pi}{2}} \tau_0 \sin\theta dS = \tau_0 \int_0^{\frac{\pi}{2}} \frac{\pi D^2}{2} \sin^2\theta d\theta = \frac{\pi^2 D^2}{8} \tau_0 \tag{3-10}$$

$$F_{\tau_0 2} = \frac{1}{8} \pi D^2 \cot\frac{\varphi}{2} \tau_0 \tag{3-11}$$

Two buoyancies are

$$F_{B1} = \frac{1}{24} \left[\rho_g - (1-\Phi)\rho_s\right] g\pi D^3 \tag{3-12}$$

$$F_{B2} = \frac{1}{48} \left[\rho_g - (1-\Phi)\rho_s\right] g\pi D^3 \cot\frac{\varphi}{2} \tag{3-13}$$

If we neglect the thrust from the sand jet stream, the acceleration of the drop will happen when the negative buoyancy balanced out by the force due to the yield stress acting on the drop: $F_{\tau_0 1} + F_{\tau_0 2} + F_{B1} + F_{B2} = 0$, which yields $\tau_0 = \frac{1}{6}\left[(1-\Phi)\rho_s - \rho_g\right] gD \frac{2+\cot\varphi/2}{\pi + \cot\varphi/2}$. Based on our observation, $\varphi = 30^\circ$. Since the thrust by the sand stream is ignored, the smallest jet from the lowest height is employed for yield stress calculation, which gives a value of 16.9 Pa for the 24 hours old gel and 34.9 Pa for the 48 hours old. The measured value of the yield stress τ_0'. see Table 3-1, is 9.8 Pa and 12.7 Pa, respectively. Given the above simplified model, the comparison is satisfactory.

3.3.4 Deformation size and yield-gravity parameter

For the deformation type I of a sand jet in gel, a drop initially started to form just below the surface of the gel and continued receiving incoming sand grains from the jet until the maximum size was obtained, and then it would accelerate and sink rapidly towards the bottom of the tank. The maximum diameter of the first drop from a sand jet, *D*, was defined as the deformation size of the sand jet, which was measured for each run and also listed in Table 3-2.

Assuming there is no shear, the volume and the force due to yield stress of a drop are respectively k_1 and k_2 times of those of a perfect sphere in the gel, then the forces acting on a drop are:

$$F_i = \dot{m} V_0 \tag{3-14}$$

$$F_b = k_1 F_b^* = k_1 \frac{\pi}{6} D^3 \left[\rho_g - (1 - \Phi)\rho_s\right] g \tag{3-15}$$

$$F_{\tau_0} = k_2 F_{\tau_0}^* = k_2 \frac{\pi^2}{4} D^2 \tau_0 \tag{3-16}$$

The superscript * indicates the corresponding force for a sphere. These forces were balanced before the deformation size was achieved. For deformation type I, F_t is negligible compared to other two forces, so

$$F_{\tau_0} + F_b = 0 \tag{3-17}$$

The yield-gravity parameter is defined as

$$Y_G = \frac{\tau_0}{gD[\rho_g - (1-\Phi)\rho_s]} \tag{3-18}$$

Substituting Equation (3-15), (3-16) and (3-18) into Equation (3-17), we obtain $Y_G = 0.212k_1 / k_2 = kY_G^*$, where $k = k_1 / k_2 = F_{\tau_0}^* /(-F_b^*)$; Y_G^* = 0.212 is the yield-gravity parameter of a sphere. Figure 3-5 shows the variation rate of $F_{\tau_0}^*$ with $-F_b^*$, which also indicates the range of k. Computed directly from Equation (3-18), Y_G is found to fall into two groups: one is in the range of 0.04 ~ 0.08, and the other is between 0.2 ~ 0.45. This is in good agreement with the results summarized by Chhabra (2007).

3.4 Summary

The deformation of vertical sand jets depositing into non-Newtonian viscoplastic fluid can be categorized into three types. For different entry velocity and size, the jet was dripping, jetting or mixing with the receiving fluid. When the jet is small and the velocity is low. a drop will form at the surface of the fluid: while for big jet with high velocity. it will jet continuously from the air into the fluid. Especially. when the velocity is extremely high and the size of the jet is very big, dispersion and agitation is observed in the receiving fluid. On the other hand, the viscosity of the fluid is also an important factor, as drops are more likely to form in viscous fluid with higher yield stress. In our experiments, the frontal speed of the sand drops in the gel was proportional to the distance away from the gel surface. The yield-gravity parameter of the deformed drops was found to fall into two groups.

Table 3-1 Bingham plastic parameters of 3.0% Laponite gels.

Time (hours)	τ_0' (Pa)	τ_0 (Pa)	μ_p (mPa·s)
24	9.8	10.4	33.6
48	12.7	15.2	18.2

Table 3-2 Experimental details and sand deformation types.

3.0%	d_e (mm)	V_e (m/s)	H (cm)	V_0 (m/s)	d_0 (mm)	Type	l_m* (cm)	D (mm)	Run No
24 h	9.6	0.22	27.3	2.33	4.4	I	87.8	4.1	1
	9.6	0.22	14.6	1.71	5.0	I	67.4	4.7	2
	9.6	0.22	6.1	1.11	7.6	II	184.9	10.7	3
48 h	9.6	0.22	26.5	2.29	4.5	II	42.5	130.6	4
	9.6	0.22	14.4	1.70	5.4	II	29.9	62.9	5
	9.6	0.22	3.6	0.87	8.2	II	17.7	64.4	6
24 h	5.4	0.09	26.8	2.29	1.7	II	16.9	4.0	7
	5.4	0.09	14.7	1.70	2.4	II	10.0	4.5	8
	5.4	0.09	5.5	1.04	3.0	III	5.5	21.8	9
48 h	5.4	0.09	26.0	2.26	1.8	III	10.0	79.4	10
	5.4	0.09	16.0	1.78	2.0	III	7.3	67.1	11
	5.4	0.09	3.2	0.80	3.2	III	2.3	55.4	12
24 h	3.3	0.08	28.2	2.35	1.1	III	7.9	39.9	13
	3.3	0.08	16.3	1.79	1.5	III	4.8	19.7	14
	3.3	0.08	6.9	1.16	1.7	III	2.8	23.7	15
48 h	3.3	0.08	27.4	2.32	1.2	III	4.9	70.2	16
	3.3	0.08	17.5	1.85	1.4	III	3.3	57.2	17
	3.3	0.08	4.9	0.99	2.0	III	1.3	49.1	18

* l_m is calculated using Equation 3-6.

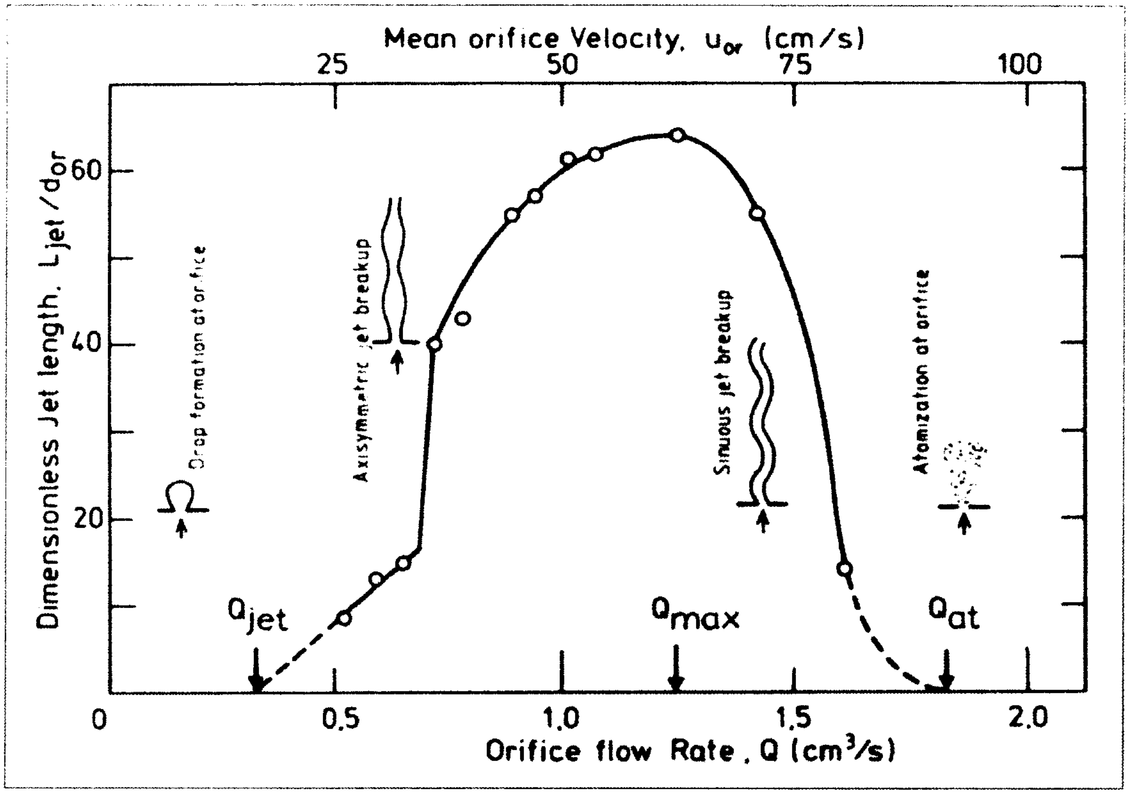

Figure 3-1 The breakup regimes of a liquid jet into drops in another medium (Clift *et al.*1978).

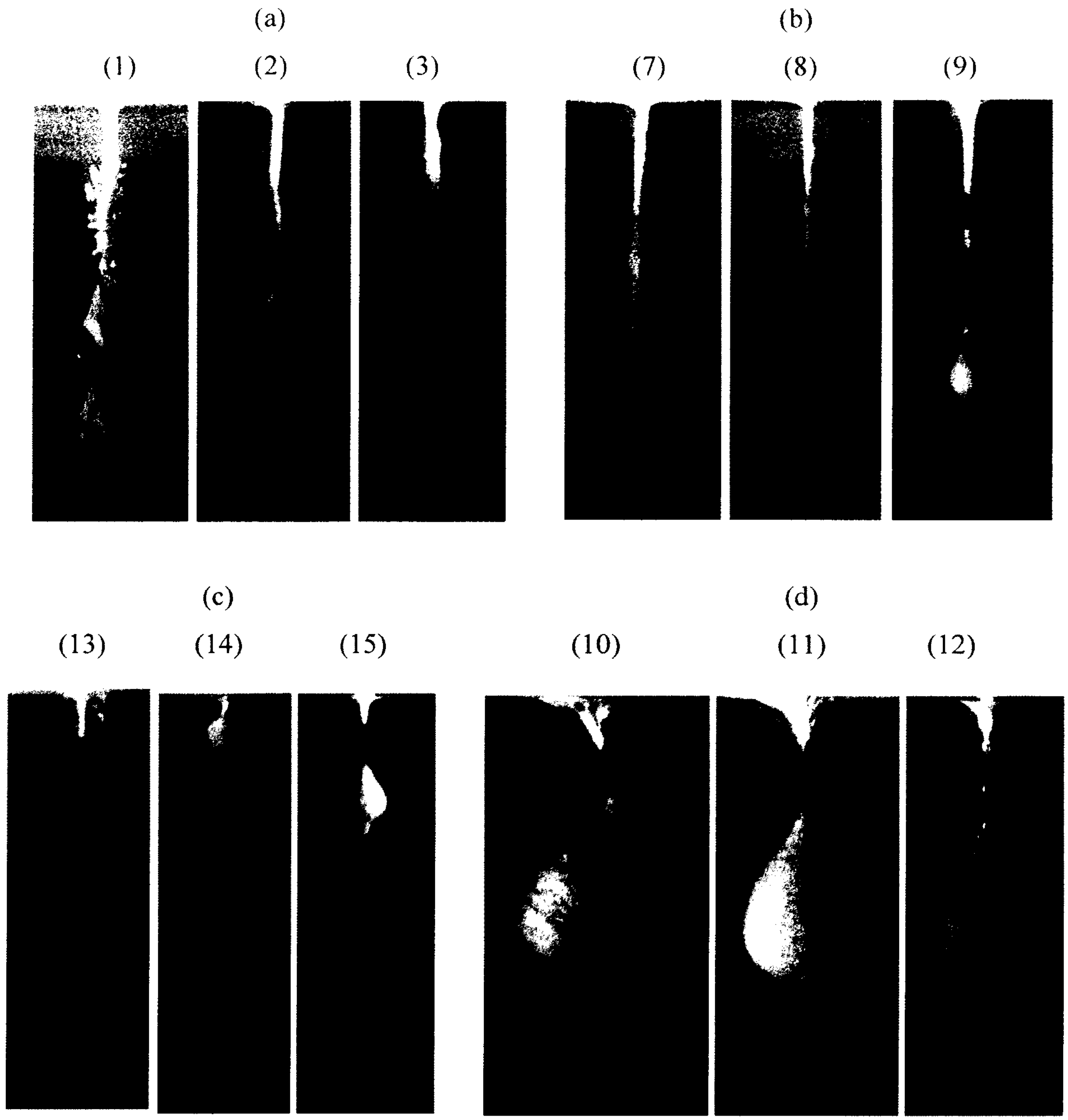

Figure 3-2 Example images of deformation types I to III of sand jets in Laponite gel. a) Run No. 1~3; b) Run No. 7~9; c) Run No.13~15; d) Run No. 10~12.

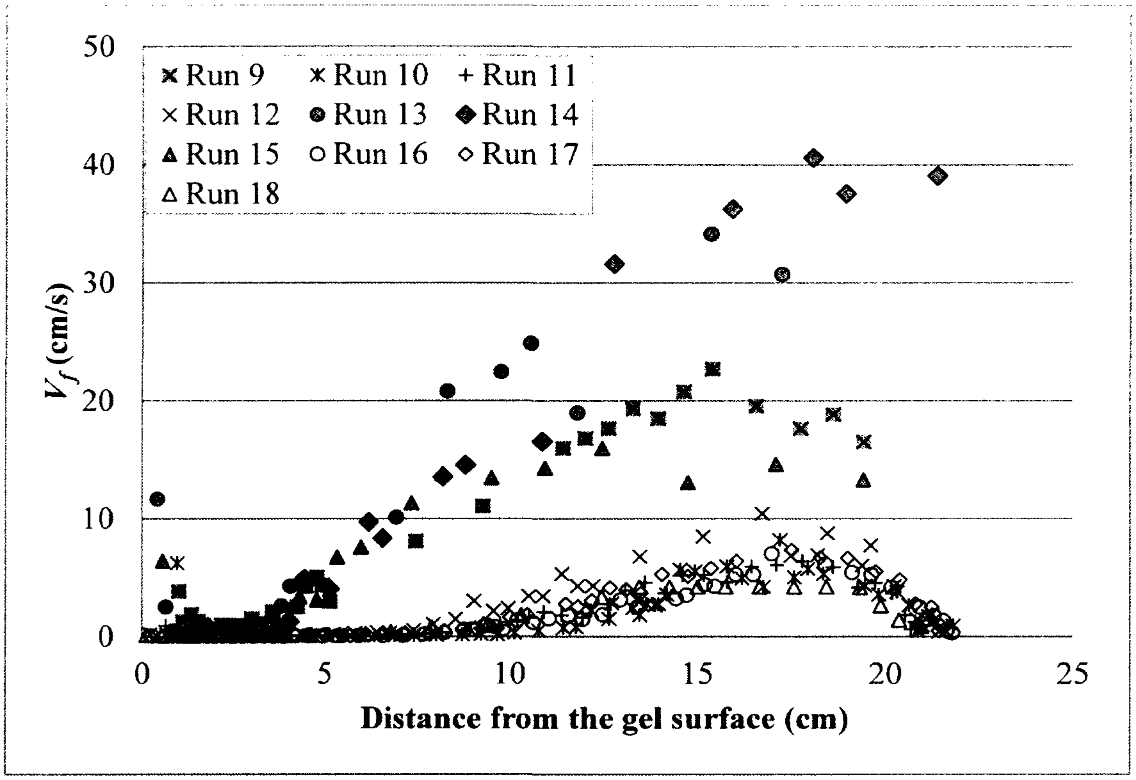

Figure 3-3 The frontal speed of sand drops in experiments. The solid markers are used for the lower viscous gel and the open markers are for higher viscosity.

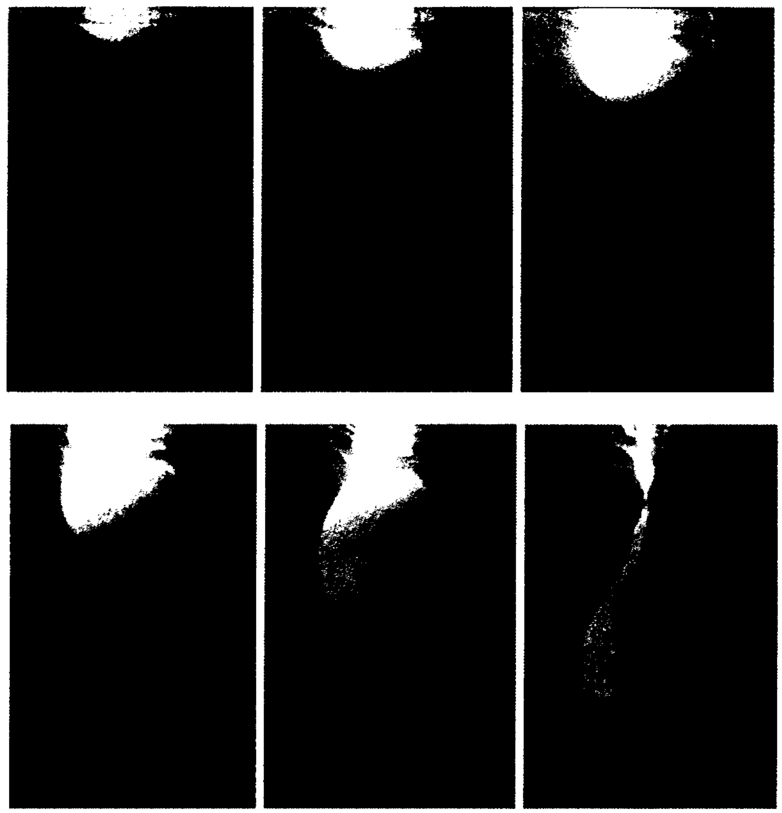

Figure 3-4 The penetration of sand drop at the surface of gel (Run No 12 at a) 5 s, b) 15 s, c) 25 s, d) 35 s, e) 45 s and f) 47 s).

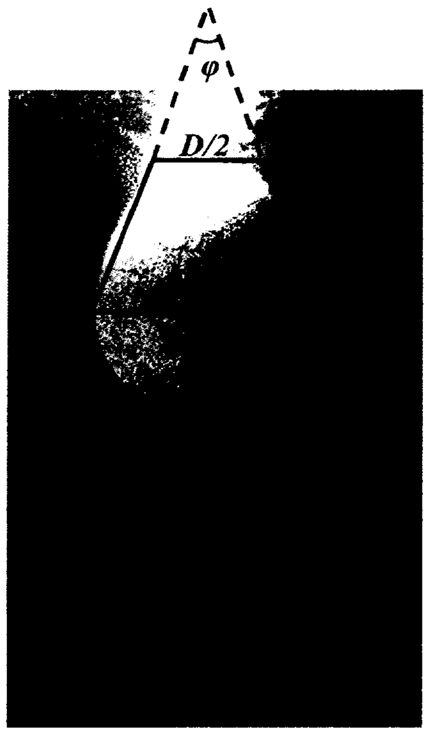

Figure 3-5 The simplification of the sand drop shape.

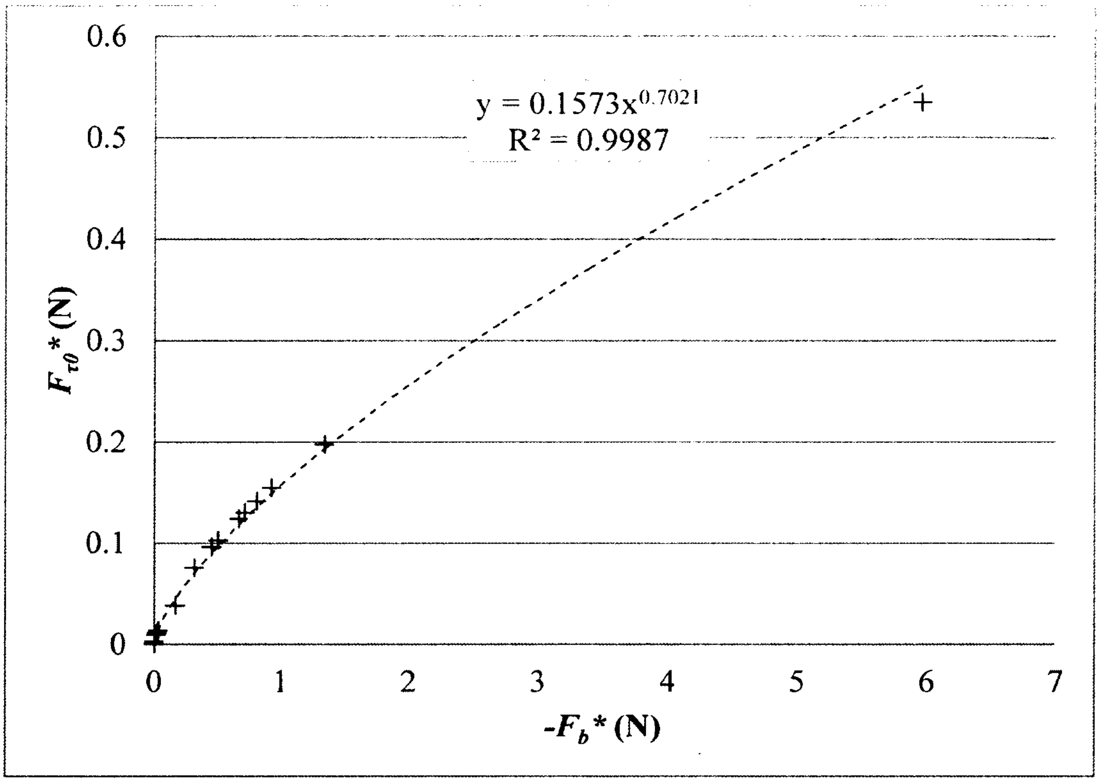

Figure 3-6 The relationship of buoyancy and the force due to yield stress of a sphere in gel.

3.5 References

Banas, L. C. (1991). "Thixotropic behaviour of oil sands tailings sludge." PhD thesis, University of Alberta, Canada.

Cai, J., Hall, N., Elenany, M., Zhu, D. Z., and Rajaratnam, N. (2010). "Observations on Sand Jets in Air." ASCE *J. Eng. Mech.*, 136(9), 1181-1186.

Chhabra, R. P. (2007). *Bubbles, drops, and particles in non-Newtonian fluids.* CRC Taylor & Francis, Boca Raton, FL.

Clift, R., Grace, J. R., and Weber, M. E. (1978). *Bubbles, Drops, and Particles.* Academic press, Inc., New York.

Dravid, V., Loke, P. B., Corvalan, C. M., and Sojka, P. E. (2008). "Drop formation in non-Newtonian jets at low Reynolds numbers." *Journal of Fluids Engineering, Transactions of the ASME,* 130(8), 0815041-0815048.

Ferroir, T., Huynh, H. T., Chateau, X., and Coussot, P. (2004). "Motion of a solid object through a pasty (thixotropic) fluid." *Physics of Fluids,* 16(3), 594-601.

Furbank, R. J. (2004). "Drop formation from particulate suspensions." PhD thesis, Georgia Institute of Technology, United States.

Goldin, M., Pfeffer, R., and Shinnar, R. (1972). "Break-up of a capillary jet of a non-Newtonian fluid having a yield stress." *The Chemical Engineering Journal,* 4(1), 8-20.

Hall, N., Elenany, M., Zhu, D. Z., and Rajaratnam, N. (2010). "Experimental study of sand and slurry jets in water." ASCE *J. Hydraul. Eng.*, 136(10), 727-738.

Jiang, J., Law, A. W., and Cheng, N. (2005). "Two-phase analysis of vertical sediment-laden jets." ASCE *J. Eng. Mech.*, 131(3), 308-318.

Kitamura, Y., Mishima, H., and Takahashi, T. (1982). "Stability of jets in liquid-liquid systems." *Canadian Journal of Chemical Engineering,* 60(6), 723-731.

Kitamura, Y., and Takahashi, T. (1982). "Breakup of jets in power law non-Newtonian - Newtonian liquid systems." *Canadian Journal of Chemical Engineering,* 60(6), 732-737.

Meister, B. J., and Scheele, G. F. (1969). "Prediction of Jet Length in Immiscible Liquid Systems." *AIChE Journal,* 15(5), 689-699.

Merkak, O., Jossic, L., and Magnin, A. (2006). "Spheres and interactions between spheres moving at very low velocities in a yield stress fluid." *Journal of Non-Newtonian Fluid Mechanics,* 133(2-3), 99-108.

Nicolas, M. (2002). "Experimental study of gravity-driven dense suspension jets." *Phys. Fluids,* 14(10), 3570-3576.

Rao, K. K., and Nott, P. R. (2008). *An introduction to granular flow.* Cambridge University Press, Cambridge; New York.

Chapter 4 Experimental Study on Pumping Viscoplastic Fluids[3]

4.1 Introduction

In the oil sands industry, the transportation and management of oil sands tailings is a challenge due to the difficulty of shearing fluids containing high concentrations of fine solids. Depending on the age and the solid contents, these tailings appear to behave like various non-Newtonian fluids. Mature fine tailings (MFT), which is mainly comprised of a high concentration of fine solids (>30% by weight), water, and residual bitumen (Luo 2004), has a high viscosity and significant yield stress (Masliyah 2006). Banas (1991) reported that oil sands tailings sludge can be classified as a non-Newtonian fluid, which behaves like a Herschel-Bulkley model material in undisturbed state and a Bingham model fluid when remoulded. Based on this, MFT can be treated as a viscoplastic fluid, especially a Bingham plastic fluid. These models are usually applicable to simulate materials like soft soil, powder, and granular grains (Yamada 1999).

Existing studies on pumping non-Newtonian fluids are mainly concentrated on the applications of pump itself rather than the dynamics of the fluids. In the field of biochemical engineering, researchers tested peristaltic pump

[3] The content of this chapter is currently being prepared as a journal manuscript: Cai, J., Zhu, D. Z., and Rajaratnam, N. (2013). "Experimental study on pumping viscoplastic fluids." *J.Eng.Mech.,to be submitted..*

or centrifugal pump, both numerically (Teran *et al.* 2008) and experimentally (Zhang *et al.* 2008), because blood and other types of fluids in the human body are all non-Newtonian. For transporting suspensions, centrifugal pump and progressive cavity pump (PCP) systems have been found to be good solutions. The study of Graham *et al.* (2009) experimentally investigated the performance of a centrifugal pump for lifting a power law fluid and a Herschel-Bulkley fluid individually, and the PCP system was analyzed and modelled by Moreno and Romero (2007) and Gamboa *et al.* (2003). Numerical analysis was also presented by Li *et al.* (1999) for extrusion process of viscoelastic cementitious flows in a shallow flight screw extruder, which is similar to a PCP system.

Suction flow of a fluid is usually represented as a point sink. In a gas-liquid withdrawal system, especially when the liquid is very viscous, if the point sink sits in the gas, both gas and fluid can be withdrawn; but for a submerged sink, only liquid gets into the intake regardless of the flow rate (Zhou and Feng 2010b; Eggers and Du Pont 2009). While many studies were focused on Newtonian fluids (Xue and Yue 1998; Zhou and Graebel 1990; Robinson *et al.* 2010), only a few papers were found that studied non-Newtonian fluids withdrawal. However, they were restricted in their investigation of surface/interface deformation and force balance (Zhou and Feng 2010a; Blanchette and Zhang 2009; Berkenbusch *et al.* 2008; Jeong 2007). There have been no experimental studies to examine the flow field of a non-Newtonian fluid being withdrawn around an intake. Our experiments were designed to develop an understanding of the flow field in this area.

However, our attempts to understand the physical processes in MFT have been hampered by the opacity of MFT that does not allow observations of the internal movements. So in this study, a Laponite® dispersion is used as an artificial MFT material. Laponite is a rheological additive to make transparent clay, which also behaves like a viscoplastic fluid and can be made by mixing Laponite powder with tap water or demineralised / deionized water at different concentrations (Southern Clay Products 2006).

This laboratory study is intended to investigate the flow field induced in a Bingham plastic fluid when the fluid is withdrawn from a vertical circular pipe intake. The scope of this study includes using a CCD camera to capture the movement of particles in the gel during pumping. The velocity of the gel is calculated based on the displacement of tracking seeds at different time increment after pumping commenced.

4.2 Laboratory Methodology

4.2.1 Rheological properties

To simulate the rheological behaviour of MFT, Laponite gel of 3% mass concentration in demineralised water was tested using Brookfield rotational viscometer (DV-II+) at room temperature. For different duration of dispersion time, vane spindles were used to obtain the yield stress and disk spindles for the measurement of viscosities. Since the measurements are not straight-forward, we followed the method described by Mitschka (1982) to convert the rheological data into the shear rate ($\dot{\gamma}$) - shear stress (τ) flow curves (Figure 4-1). The results indicate that either the yield stress (Figure 4-2) or the viscosity of the gels keeps increasing for up to 30 days. But the 48 hours old sample, with a yield stress 12.7 Pa, is found to have the properties most similar to MFT. According to our measurements, a Bingham plastic model

$$\tau = \tau_0 + \mu_p \dot{\gamma} \tag{4-1}$$

can be adapted to fit the rheological data of 3% Laponite gel, where τ and $\dot{\gamma}$ refer to the shear stress and the shear rate of the gel; τ_0 and μ_p are, respectively, the yield stress and the plastic viscosity in the Bingham plastic model. All optimal coefficients are listed in Table 3-1. It should be noted that the measured yield stress (τ_0') is usually smaller than the value that can fit with Equation (4-1) for a real fluid (Wilkinson 1960).

To make 3% gel, Laponite powder has to be slowly sifted into demineralised water in a container while an electric mixer continually breaks down all formed clusters of powder. The mixer needs to continuously agitate for one hour, so that all clumps are saturated and well mixed. After mixer is removed, the container should be covered and sealed by a layer of plastic wrap to prevent evaporation while Laponite powder hydrates with water to build a jelly texture. At the room temperature (~ 21°), it takes 43 to 44 hours for this mixture to obtain the selected viscosity.

4.2.2 Experiment design

A schematic of the experimental setup is shown in Figure 4-3. A glass tank with width (W) of 50 cm, depth (D) of 25 cm, and height (H) of 30 cm was used for all the experiments. A vertical PVC pipe was placed in the center of the tank filled with 3% Laponite gel and it was attached to the inlet of a PCP system. To investigate the impact of intake size on the pumping velocity field, two pipes of different diameters were used as the intake for pumping; and for each diameter, the pumping discharge was varied to check the differences. In total, five tests were performed. Table 4-1 is a list of the experimental parameters, where the inner and outer diameters of the pipe are denoted as d_0 and d_1; h_1 is the initial submergence of the intake in the gel and h_2 is the distance from the intake entrance to the bottom of the tank; V_0 and Re_B are, respectively, the average velocity and the Reynolds number inside the pipe, wherein, Reynolds number was defined in a modified form $\mathrm{Re}_B = \dfrac{\rho_g d_0 V_0}{\mu_p}$ for Bingham plastic fluids. For each test, several pumping rates were set and the steady pumping flow rate (Q_m) was calculated by collecting gel at the outlet of the pump several times during the process and averaging the measurements. To verify the flow regime, the Hedstrom number ($He = \dfrac{d_0^{\,2} \rho_g \tau_0'}{\mu_p^2}$) was calculated and the critical Reynolds number, $(\mathrm{Re}_B)_c$, was obtained using the principles proposed by Hanks (1963). This critical number marks the transition from laminar flow to turbulent flow for Bingham plastic fluids. In particular, when $He = 0$, it becomes 2100, which is the criterion for differentiation between laminar and turbulent flows of a Newtonian fluid. Given $\mathrm{Re}_B < (\mathrm{Re}_B)_c$, all experiments listed in Table 4-1 were running within the laminar region.

Black poppy seeds, 1.3 mm to 1.8 mm in diameter, were used as tracer particles in our experiments. First, these seeds were mixed with 3% Laponite gel in a beaker. This gel was made the same day as the gel in the tank, and after more than 40 hours the yield stress has developed. As a result, seeds actually "float" and are uniformly distributed in the gel to create a seed-gel mixture. Later, a dropper was used to inject this mixture into the center plane across the tank. In order to put the particles in the right position, a light sheet was applied to define the center plane. This light sheet was produced by a side-facing slide projector that had been tailored to only shine light in along a thin vertical band. After the injection, all black seeds were suspended in the gel and can be distinguished easily using a plain white background. Food colour was used to mark the center plane at the gel surface. It allows observation of the surface change during the experiment. This procedure usually took about 3 hours to complete.

After 48 hours following gel preparation, the pumping and test was started. At this time, the volume of the Laponite gel had expanded by 2.4%, and the density of the gel was 1002.93 kg/m^3. In our experiments, a CCD camera

(PULNIX TM-1400CL), with a resolution of 1392×1040 pixels, was used to capture pictures at a rate of 30 frames per second (fps). The camera was placed 30.5 cm away from the front wall of the tank and it was located at the same level as the intake entrance. The observation window size is about 22 cm in height and 16 cm in width. Correction and scale were applied to image distortion.

A Seepex progressive cavity pump of size 10 and range BW (Seepex GmbH) was used in our experiments. This pump has a capacity of water flow rate up to 3.81 l/s with the maximum pumping rate at 1100 rpm. Running at the fastest rate, the pump was tested to withdraw 3% Laponite gel of different ages. We observed that, for the 10.1 mm intake, it was able to remove 48 and 96 hours old gels, but it failed to withdraw 216 hours old gel out of the tank, which has a yield stress around 66 Pa. However, under sheared condition, for example, if the gel had been stirred for a short time just before pumping, it could be withdrawn. The reason is that Laponite gel is a thixotropic non-Newtonian fluid. It displays a decrease in both viscosity and yield stress over time under a constant shear rate.

Figure 4-4 shows a set of raw images of pumping Laponite from the 7.2 mm intake pipe at different times during the test. It was shown that the surface of the gel was initially flat and gradually curved towards the centerline of the intake. The pumping discharge was monitored and found to increase at the beginning but reached a stable state during the experiment when the gel surface dropped down to the level of the intake entrance.

The commercial image processing software, Davis 8, from by LaVision®, was used to calculate the velocity field for each experiment. It is designed to process Particle Image Velocimetry (PIV) images, but could be also applied in our case, because the idea of tracking particles works the same way as in a PIV setup. Compared with a typical PIV image, our particle is much bigger and the distribution density is relatively low, hence the interrogation window size was set to 256 by 256 pixels with an overlap of 87%. The velocity fields were computed for all five tests at different times and an example (test No. 4) is presented in Figure 4-5. When the software was applied, three regions were masked out for every image, as marked by the dotted lines in Figure 4-3: the rectangular area occupied by the intake pipe, the zone very close to the entrance and the lowest part due to the reflection from the bottom of the tank. The reason for removing the second region is that the speed of our camera is limited to 30 fps, only allowing for tracking movement below 1.2 m/s within an interrogation window (256 pixels). However, all mean velocities at the entrance are higher than 1.2 m/s as shown in Table 4-1. In addition, the tracking seeds were travelling so fast that very few could be captured near the entrance. Contour plots are also displayed in Figure 4-5 to give a better description of the flow.

4.3 Results and Discussions

4.3.1 *Stable state*

In a masked domain (see Figure 4-3) containing a number of N velocity vectors, the field average velocity is defined as $|V|_{avg} = \frac{\sum_{i=1}^{N} |V|_i}{N} = \frac{\sum_{i=1}^{N} \sqrt{{v_{xi}}^2 + {v_{yi}}^2}}{N}$.

Assuming the obtained flow pattern is similar during one test, the $|V|_{avg}$ can be used as an index for measuring the flow movement or strength of pumping rate. The higher it is, the bigger the discharge induced by the pump. Time serial values of $|V|_{avg}$ are plotted in Figure 4-6 from which the stable state can be assigned. In the chart, four out of five tests were running towards a stable state after a sharp rise in the beginning. The only exception is the one with the biggest flow rate, whose velocity might be strongly affected by the volume limitation of the tank. Therefore the flow finished so fast that it didn't have enough time to reach the stable stage. However, at t = 20 s a semi-stable state was achieved and it will be treated as the stable state in the following analysis.

Figure 4-7 contains plots of the stable velocity field, velocity contours and the gel surface profile of each experiment. The flow pattern appears to be similar in all tests, but unlike the potential sink flow of a Newtonian fluid, the velocity contours are not spherical and the radial velocity decays at varied rate along different angular directions.

4.3.2 Velocity

In a 3D Cartesian coordinate system, if the origin is located at the centerline of the entrance and the x-axis goes downwards as shown in Figure 4-8, the center plane across the tank can be defined as $z = 0$. Generally, velocity of a suction flow through one single intake increases radially towards the intake as it is approaching and the increasing rate is inversely proportional to some power of the radial distance from the intake point. However, in our system, the velocity field is different.

4.3.2.1 Horizontal components

The horizontal and vertical components of the velocities are denoted as v_y and v_x. Figure 4-9 shows two plots of v_y at different y locations, in which each curve represents all horizontal velocity components along one vertical line in the center plane. These curves are bell-shaped close to the intake but flatten out away from it. The peak of each curve indicates where the maximum horizontal velocity component is located along x direction at different y location. The positions of these peaks are plotted in Figure 4-10 and the averaged x location of test No. 1~3 and test No. 4~5 are displayed by the dashed lines. It is shown that the mean value of peak locations don't change with different flow rate, but only depends on the diameter of the intake pipe, d_0. In other words, the maximum horizontal velocity along the y-axis is always located $1.4d_0$ below the intake level. Based on that, a virtual sink is assumed to be located along the centerline below the intake pipe and the distance away from the entrance is equal to $1.4d_0$.

4.3.2.2 Cone shaped zone

In a spherically symmetric radial flow, the axisymmetric sink flow solution for the velocity in an infinite domain is

$$u_r = \frac{Q}{4\pi r^2} \tag{4-2}$$

wherein r is the radial distance from the point sink (Papanastasiou *et al.* 2000). As shown in Figure 4-7, when the flow is stable, a kidney shaped sheared zone was observed for all five tests The radial velocity in the center plane increases dramatically as the fluid is being sucked into this point sink (O). If a spherical polar coordinate system is employed with its origin located at O (Figure 4-8), the radial velocity u_r can be obtained at different angles. Figure 4-11 shows that, within a conical region $0 \leq \theta \leq 15°$, u_r does not appear to change with the angle and the axisymmetric point sink flow solution is found to overestimate the flow velocity within this region.

4.3.2.3 Radial velocity at different angles

Beyond the cone-shaped zone, radial velocity u_r does not vary or decay at the same rate along different angular directions. Its variation is demonstrated in Figure 4-12 at four angles, where $\theta = 0°, 45°, 90°, 135°$.

For a steady-state fluid in spherical coordinates, the continuity equation is

$$\frac{1}{r^2}\frac{\partial}{\partial r}(r^2 u_r) + \frac{1}{r\sin\theta}\frac{\partial}{\partial\theta}(u_\theta \sin\theta) + \frac{1}{r\sin\theta}\frac{\partial u_\phi}{\partial\phi} = 0 \tag{4-3}$$

If there is only radial movement and an axisymmetric flow is assumed along x'-axis, Equation (4-3) can be simplified into $\frac{1}{r^2}\frac{\partial}{\partial r}(r^2 u_r) = 0$, thus

$$u_r = \frac{f_1(\theta)}{r^2} \tag{4-4}$$

where f_1 is a function of θ only.

Compared with Equation (4-2), the Equation (4-4) can be further rewritten as

$$u_r = \frac{f(\theta)}{r^2}\cdot\frac{Q}{4\pi} = f(\theta)\frac{Q}{4\pi r^2} \tag{4-5}$$

$f(\theta)$ is a function of θ. For a fixed angle, it becomes a constant, and $\sqrt{Q/u_r}$ increases linearly with r. This idea was tested in Figure 4-13, where all the radial velocities are plotted in terms of the value of θ. In every subplot, a dashed line is used to indicate the average of different values of $f(\theta)$ (see Figure 4-14) which best fits the dataset for each test. For two pipe sizes, all the data follows the same curve and Equation (4-5) can be used to predict the velocity.

If the following assumptions are applied: (a) the Laponite gel is incompressible, (b) it is running at a steady state, (c) it is a laminar flow, (d) it is an axisymmetric flow with respect to x'-axis and (e) there is radial motion only, the rate of deformation tensor can be simplified as

$$\dot{\gamma} = \begin{bmatrix} \dot{\gamma}_{rr} & \dot{\gamma}_{r\theta} & \dot{\gamma}_{r\phi} \\ \dot{\gamma}_{\theta r} & \dot{\gamma}_{\theta\theta} & \dot{\gamma}_{\theta\phi} \\ \dot{\gamma}_{\phi r} & \dot{\gamma}_{\phi\theta} & \dot{\gamma}_{\phi\phi} \end{bmatrix} = \begin{bmatrix} 2\frac{\partial u_r}{\partial r} & \frac{1}{r}\frac{\partial u_r}{\partial \theta} & 0 \\ \frac{1}{r}\frac{\partial u_r}{\partial \theta} & 2\frac{u_r}{r} & 0 \\ 0 & 0 & 2\frac{u_r}{r} \end{bmatrix} \tag{4-6}$$

The Bingham fluid constitutive laws are

$$\tau_{ij} = (\mu_p + \frac{\tau_0}{|\dot{\gamma}|})\dot{\gamma}_{ij} \Leftrightarrow |\tau| > \tau_0$$

$$|\dot{\gamma}| = 0 \Leftrightarrow |\tau| \le \tau_0 \tag{4-7a,b}$$

where $|\tau|$ and $|\dot{\gamma}|$ are, respectively, the second principal invariant of the stress tensor and the rate of deformation tensor. They are defined as $|\tau| = (\frac{1}{2}\sum_{i,j=1}^{3}\tau_{ij}^2)^{\frac{1}{2}}$ and $|\dot{\gamma}| = (\frac{1}{2}\sum_{i,j=1}^{3}\dot{\gamma}_{ij}^2)^{\frac{1}{2}}$ (Tadmor and Gogos 2006). According to Equation (4-6), it comes to

$$|\dot{\gamma}| = \sqrt{2\left(\frac{\partial u_r}{\partial r}\right)^2 + 4\frac{u_r^{\ 2}}{r^2} + \frac{1}{r^2}\left(\frac{\partial u_r}{\partial \theta}\right)^2} \tag{4-8}$$

In the fluid domain, the area where $|\tau| \le \tau_0$ is under a zero rate-of-strain condition, hence it moves like a rigid solid. Fluid in other regions is moving like viscous liquid and the components of stress tensor can be calculated based on Equation (4-7a) and (4-8). Then the momentum equations in a spherical system become Equation (4-9) and (4-10).

$$\rho u_r \frac{\partial u_r}{\partial r} = -\frac{\partial p}{\partial r}$$

$$+\frac{1}{r^2}\left(4r\frac{\partial u_r}{\partial r} + 2r^2\frac{\partial^2 u_r}{\partial r^2} + \cot\theta\frac{\partial u_r}{\partial \theta} + \frac{\partial^2 u_r}{\partial \theta^2} - 4u_r\right)\cdot\left[\mu_p + \frac{\tau_0}{\sqrt{2\left(\frac{\partial u_r}{\partial r}\right)^2 + 4\frac{u_r^{\ 2}}{r^2} + \frac{1}{r^2}\left(\frac{\partial u_r}{\partial \theta}\right)^2}}\right] \tag{4-9}$$

$$0 = -\frac{1}{r}\frac{\partial p}{\partial \theta} + \frac{1}{r^2}\left(4\frac{\partial u_r}{\partial \theta} + r\frac{\partial^2 u_r}{\partial r \partial \theta}\right)\cdot\left[\mu_p + \frac{\tau_0}{\sqrt{2\left(\frac{\partial u_r}{\partial r}\right)^2 + 4\frac{u_r^{\ 2}}{r^2} + \frac{1}{r^2}\left(\frac{\partial u_r}{\partial \theta}\right)^2}}\right] \tag{4-10}$$

Introducing Equation (4-5) into Equation (4-9) and (4-10), and cross differentiating Equation (4-9) with respect to θ, Equation (4-10) with respect to r, the pressure term will be canceled out, then it comes to

$$
\frac{\rho Q}{\pi r^5} f(\theta) f'(\theta) + \frac{\mu_p}{r^4}\left[-\csc^2 \theta f'(\theta) + \cot \theta f''(\theta) + f'''(\theta)\right]
$$
$$
-\frac{\tau_0}{r}\left\{\frac{-\csc^2 \theta f'(\theta) + \cot \theta f''(\theta) + f'''(\theta)}{\left[12 f(\theta)^2 + f'(\theta)^2\right]^{1/2}} - \frac{\left[\cot \theta f'(\theta) + f''(\theta)\right]\left[12 f(\theta) f'(\theta) + f'(\theta) f''(\theta)\right]}{\left[12 f(\theta)^2 + f'(\theta)^2\right]^{3/2}}\right\}
$$
$$
= -\frac{6\mu_p f'(\theta)}{r^4}
$$

(4-11)

Since we assume *f(θ)* is a function independent of θ, the factors of r^{-4} in Equation (4-11) should be equalled. Also, the factors of r^{-5} and r^{-1} can be proved to be not very important in the sheared zone where the yield stress has been overcame and a power-law stress-strain relationship maybe apply. Thereby, the following equation can be used to find the approximate solution of *f(θ)*:

$$
(\csc^2 \theta - 6) f'(\theta) = f'''(\theta) + \cot \theta f''(\theta) \qquad (4\text{-}12)
$$

$f(\theta) = C_1 \cos 2\theta + C_2$ is one of the general solutions of Equation (4-12). C_1 = -0.39 and C_2 = 1.0 is the set of best-fit coefficients within $0° \le \theta \le 150°$ when compared with the experimental data in Figure 4-14. In this figure, the error bars are generated by fitting each dataset individually for all five tests and thereby they demonstrate the range of *f(θ)* for best fitting all dataset. Finally, the approximate solution

$$
f(\theta) = -0.39 \cos 2\theta + 1.0 \qquad (4\text{-}13)
$$

can be employed to describe the velocity field of Laponite when $0° \leq \theta \leq 150°$.

4.3.3 Deformed area

In our experiments, 2-dimensional (2D) velocity data were obtained in the central plane across the tank, as a result the maximum shear strain is limited to be calculated in 2D, which is $|\dot{\gamma}|_{\max} = \frac{1}{2}\sqrt{(\frac{\partial v_x}{\partial x} - \frac{\partial v_y}{\partial y})^2 + (\frac{\partial v_x}{\partial y} + \frac{\partial v_y}{\partial x})^2}$. All the contour plots for $|\dot{\gamma}|_{\max}$ are presented in Figure 4-15. Those regions where $|\dot{\gamma}| < 0.1 s^{-1}$ are under low shear stress and the fluid within them is moving like solid, so they are often referred as "rigid" regions or plug regions (Widjaja *et al.* 2003). In contrast, the rest are sheared by relatively high stresses and they are called as "flow" regions. Figure 4-15 shows that the radius of these flow regions depends on the pumping discharge and higher discharge yields bigger deformation radius.

Combined with Equation (4-5) and Equation (4-8), the shear rate of Laponite in 3D can be arrived at:

$$|\dot{\gamma}| = \frac{Q}{4\pi r^3}\sqrt{12 f(\theta)^2 + f'(\theta)^2} \tag{4-14}$$

Substitute *f(θ)* in Equation (4-14) with Equation (4-13), we have

$$|\dot{\gamma}| = \frac{Q}{4\pi r^3}\sqrt{1.24\cos^2 2\theta - 9.44\cos 2\theta + 12.61} \tag{4-15}$$

The maximum shear rate occurs at θ = 90°, with the value equal to $|\dot{\gamma}| = 1.21Q/\pi r^3$ and the minimum is $|\dot{\gamma}| = 0.53Q/\pi r^3$ when θ = 0°. The magnitude of $|\dot{\gamma}|$ is proportional to the withdrawal discharge Q. If deformed area is defined as the region where $|\dot{\gamma}| \geq 0.1s^{-1}$, the deformation radius is found to increase with the cube root of the withdrawal flow rate: $\tilde{r} \propto Q^{1/3}$. Figure 4-16 contains two images which were taken before and after a random test. The deformed region is easily demonstrated by the black tracer particles.

4.4 The Numerical Solver

4.4.1 General description

The numerical solver solves the unsteady Navier-Stokes equation applying a non-Newtonian model to assess viscosity. A homogenous multiphase model is used to simulate the unsteady draining condition. A commercial CFD code, ANSYS CFX, is used to solve the conservation equations (CFX 2009). The governing equations are,

$$\frac{\partial \rho}{\partial t} + \frac{\partial \rho u_i}{\partial x_i} = 0 \tag{4-16}$$

$$\frac{\partial \rho u_i}{\partial t} + \frac{\partial \rho u_j u_i}{\partial x_j} = -\frac{\partial p}{\partial x_i} + \frac{\partial}{\partial x_j}\left\{\mu\left(\frac{\partial u_i}{\partial x_j} + \frac{\partial u_j}{\partial x_i}\right)\right\} + (\rho - \rho_a) g_i \qquad (4\text{-}17)$$

$$\rho = \alpha_g \rho_g + \alpha_a \rho_a \qquad (4\text{-}18)$$

$$\mu = \alpha_g \mu_g + \alpha_a \mu_a \qquad (4\text{-}19)$$

where, ρ_g is the density of the gel, ρ_a is the density of air, α_g is the volume fraction of the gel, α_a is the volume fraction of air, p is the pressure, μ_g is the molecular viscosity of the gel, and μ_a is the molecular viscosity of air. The transport equations for α_g and α_a are,

$$\frac{\partial \alpha_g}{\partial t} + u_j \frac{\partial \alpha_g}{\partial x_j} = 0 \qquad (4\text{-}20)$$

$$\alpha_a = 1 - \alpha_g \qquad (4\text{-}21)$$

The molecular viscosity of the gel is computed using the Bingham model dependent on the shear-strain rate.

The solver uses unstructured mesh and finite volume method to discretize the governing equations. The central difference advection scheme is used which is second order accurate and free from numerical diffusion. As the experimental geometry is symmetric, a quarter of the flow domain is used in the computation.

Average grid spacing of 0.33 cm is used in the flow domain and local refinement is used in the intake location, where a spacing of 0.15 cm is used. The refinement zone takes the shape of a sphere of a diameter of 3 cm. Figure 4-17 shows the model geometry and the unstructured mesh. Approximately 360,000 nodes were used in the solution domain. Mass flow rate is provided at the pump intake location. At the top surface, a pressure boundary is applied which allows air to be entrained in the domain when the interface drops down. A symmetry boundary condition is applied in the bisected walls. All other walls were specified as no-slip boundaries. The experimental scenario 1 and 4 (see Table 4-1) are simulated numerically.

The interface is created by defining the volume fraction of the Laponite gel and air. The initial velocity of the Laponite gel is taken as zero, and the initial pressure is provided as hydrostatic. The transient solver uses a time-step of 0.1 second.

4.4.2 Discussions

Figure 4-18 and Figure 4-19 show the comparison between the experimental and the computed velocity profiles for scenario 1 and 4, respectively. The radial velocity (u_r) profiles are shown at six radials having θ is equal to 0°, 30°, 60°, 90°, 120° and 150°, respectively. The radial velocity (u_r) is the velocity component along the radial. The positive magnitude implies velocity vectors pointing towards the pump intake location. In scenario 1, the normalized mean absolute error (MAE) is computed as 29% and it is 30% for scenario 4. The MAE is computed by averaging the absolute errors. The MAE is then normalized by the average values of the experimental data.

Again, assume the velocity field can be described by Equation (4-6). The variation of $f(\theta)$ with θ is shown by the empty diamonds in Figure 4-14, which is in good agreement with those of the experimental data.

4.5 Summary

This chapter presents a laboratory study on pumping a Bingham plastic fluid from a vertical circular pipe by a PCP system. The experimental results show that the intake pipe can be simplified as a virtual point which located $1.4d_o$ below the intake entrance and the size of the intake pipe has no impact on the radial velocity. The horizontal velocity in far field away from the intake appears to be symmetric to a horizontal line, which is $1.4d_o$ below the intake level. In spherical polar coordinates, a conical zone is found to be within 15° under the intake. In this region, the magnitudes of radial velocity at different directions are almost the same; while in the outer region from 15° to 150°, the radial velocity varies angularly. In the flowing domain, the radius of deformed area is proportional to the 1/3 power of the pumping flow rate.

4.6 Notation

d_0	Inner diameter of the intake pipe
d_1	Outer diameter of the intake pipe
h_1	Initial submergence of the intake in the gel
h_2	Distance from the intake to the bottom of the tank
He	Hedstrom number
N	The number of velocity vectors
Q	Steady pumping discharge
Q_m	Measured steady pumping rate
r	Radius in spherical coordinates
$\tilde{r}$	Deformation radius
Re_B	Bingham Reynolds number
t	Time from the commencement of pumping
$u_{r,\theta,\varphi}$	Velocity components in spherical coordinate system
v_x	Vertical component of 2D velocity
v_y	Horizontal component of 2D velocity
V_0	Velocity in the intake pipe
$\lvert V \rvert_{avg}$	Field average velocity
x, y, z	Cartesian coordinates
μ_p	Plastic viscosity
τ	Shear stress
τ_0	The value of yield stress which fits the viscosity measurements
τ_0'	The measured yield stress
$\dot{\gamma}$	Shear rate
θ, φ	Spherical coordinates

Table 4-1 Experimental parameters.

No	d_0 *(mm)*	d_1 *(mm)*	Q_m *(ml/s)*	V_0 *(m/s)*	h_1 *(cm)*	h_2 *(cm)*	$\mathbf{Re}_B$	*He*	$(\mathbf{Re}_B)_c$
1	7.2	13.8	84	2.08	8.5	12.5	824	1986	2300
2	7.2	13.8	137	3.39	8.5	12.5	1342	1986	2300
3	7.2	13.8	144	3.57	8.6	12.4	1411	1986	2300
4	10.1	17.1	95	1.19	9.1	11.9	661	3922	2900
5	10.1	17.1	153	1.92	9.1	11.9	1067	3922	2900

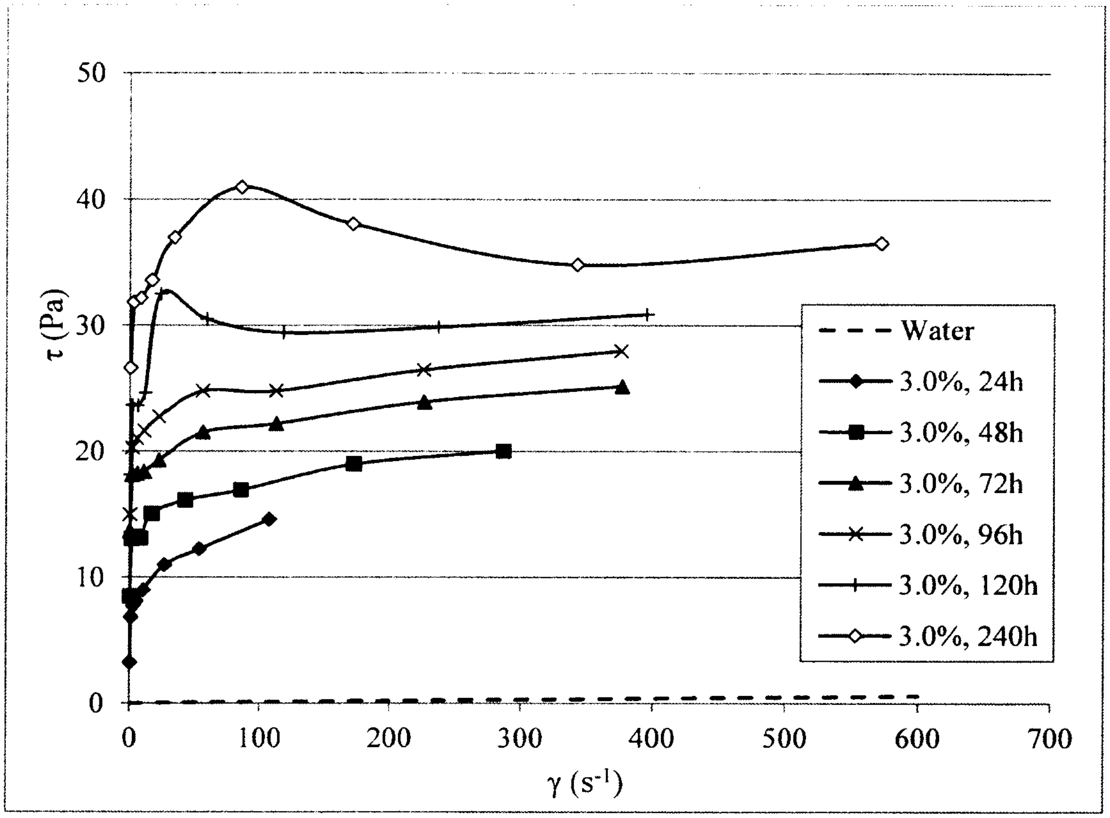

Figure 4-1 Rheological measurements of 3.0% Laponite gel samples.

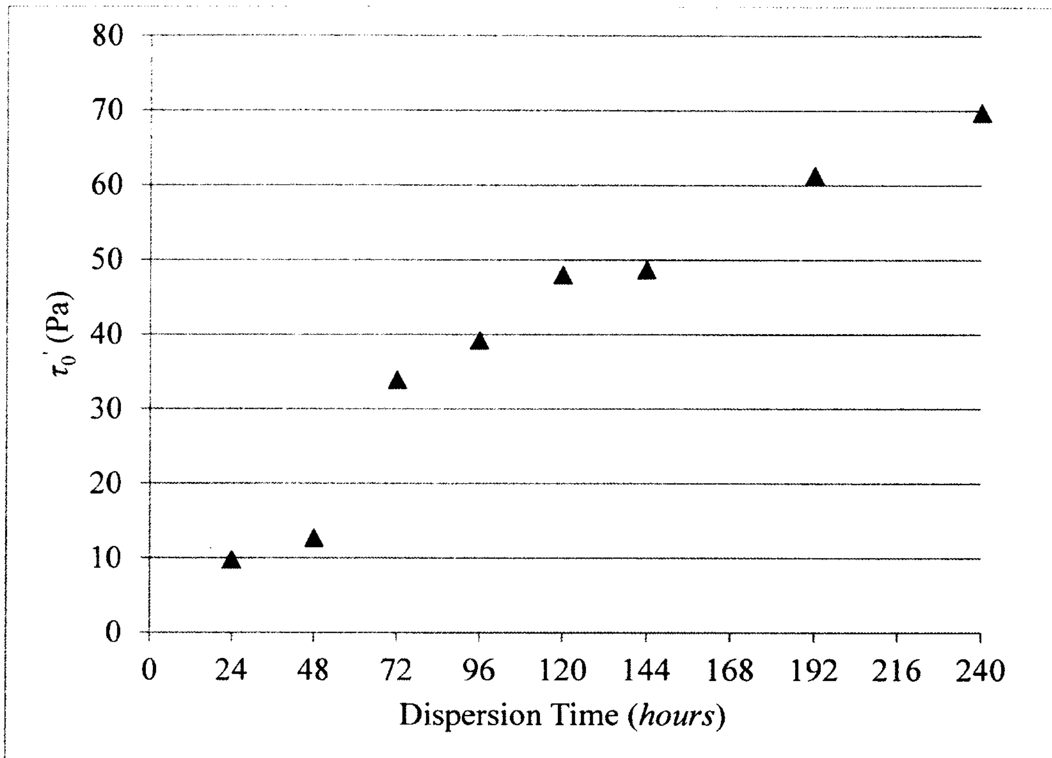

Figure 4-2 Yield stress measurements 3.0% Laponite samples.

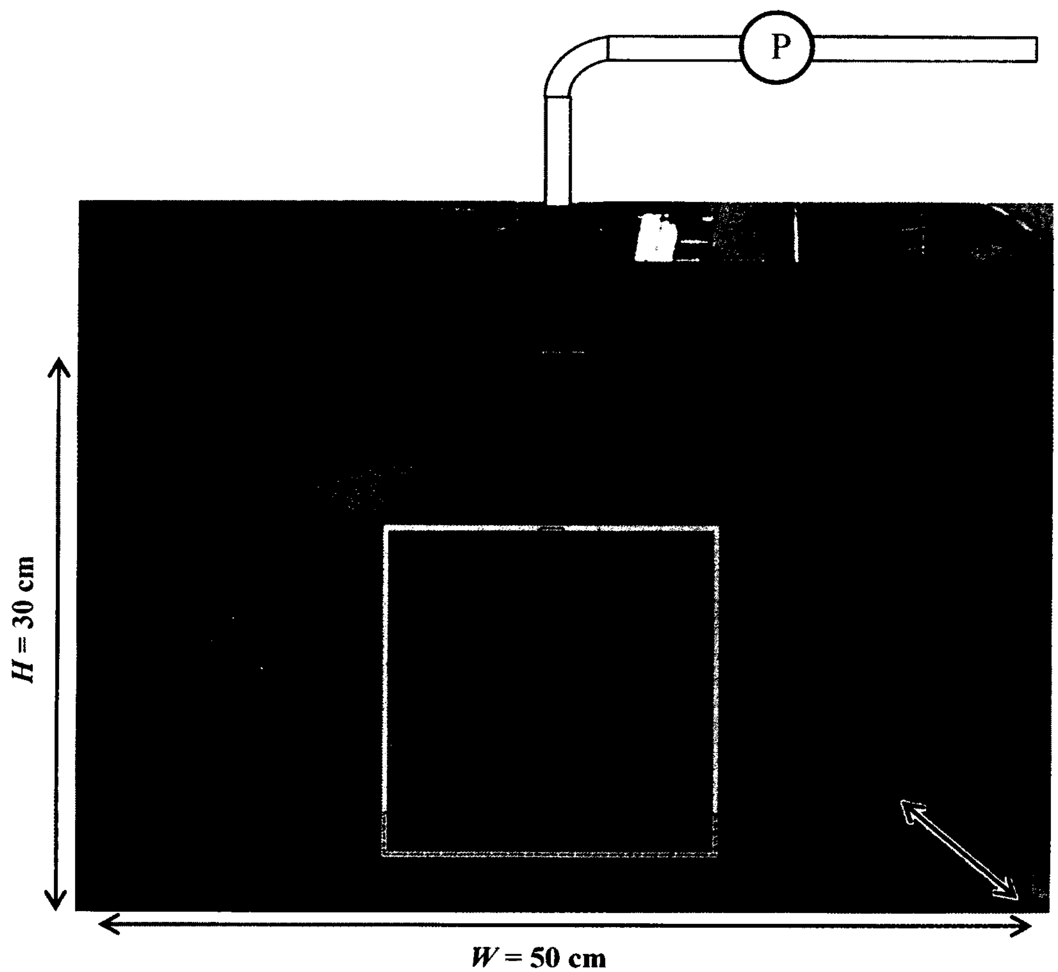

Figure 4-3 Schematic of laboratory setup and the observation window.

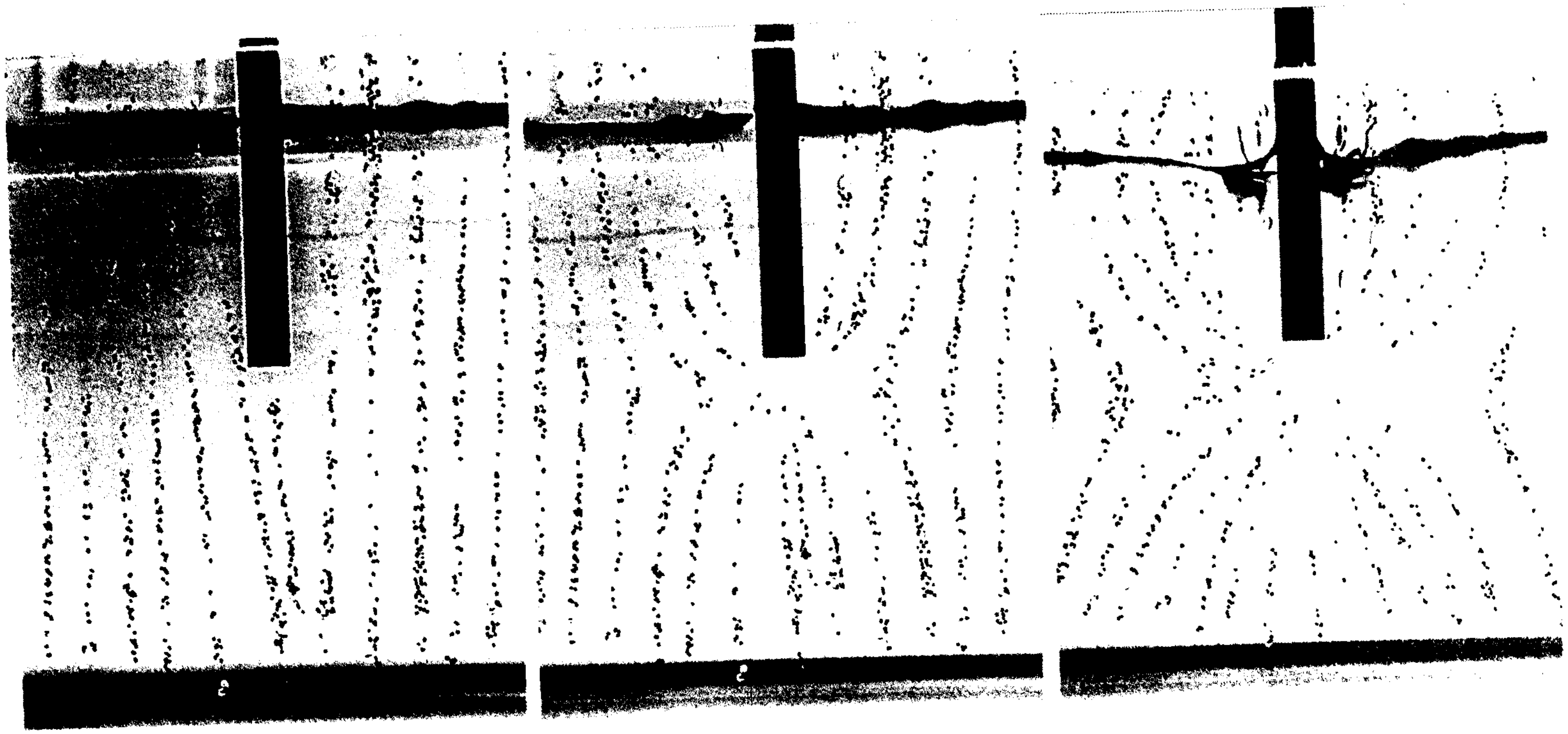

Figure 4-4 Experimental raw images of Test No. 1 at 0 sec, 23 sec and 46 sec.

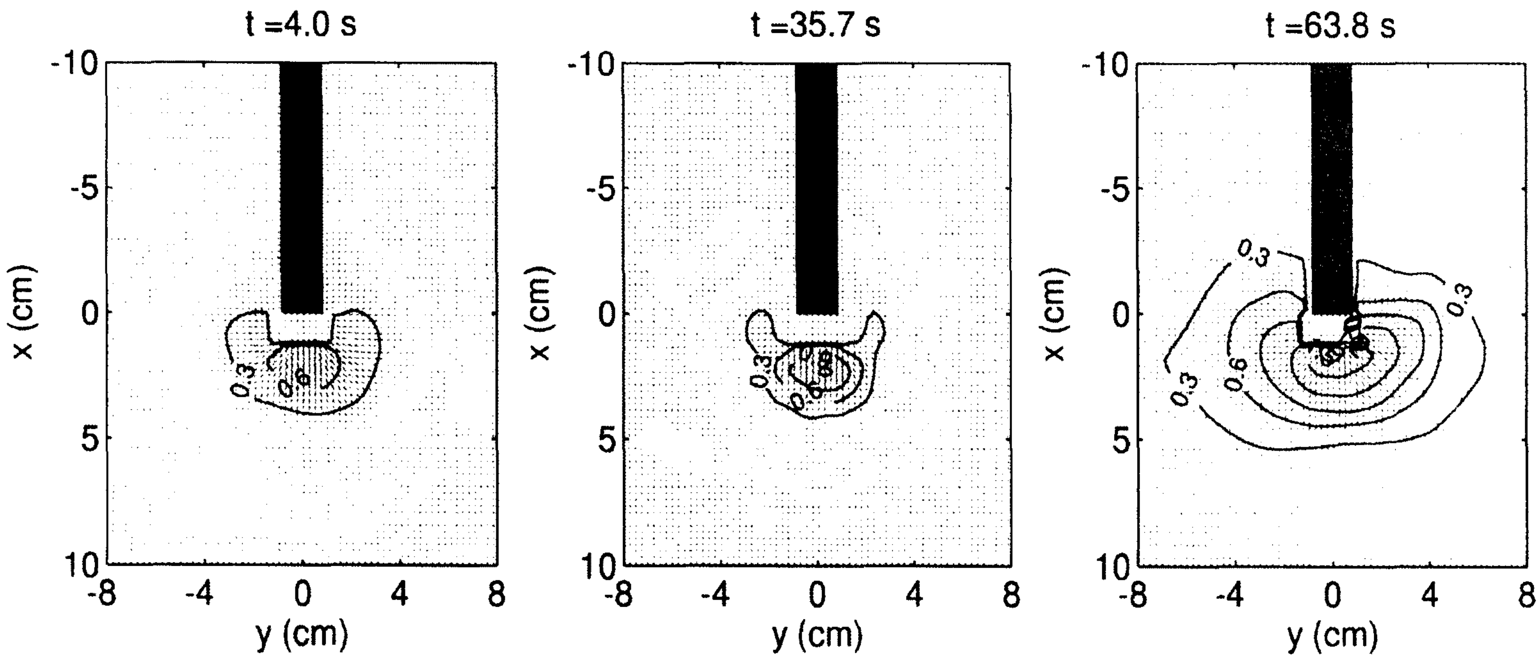

Figure 4-5 Velocity field of test No. 4 at different time during pumping.

The contour plots of the velocity are in the unit of cm/s.

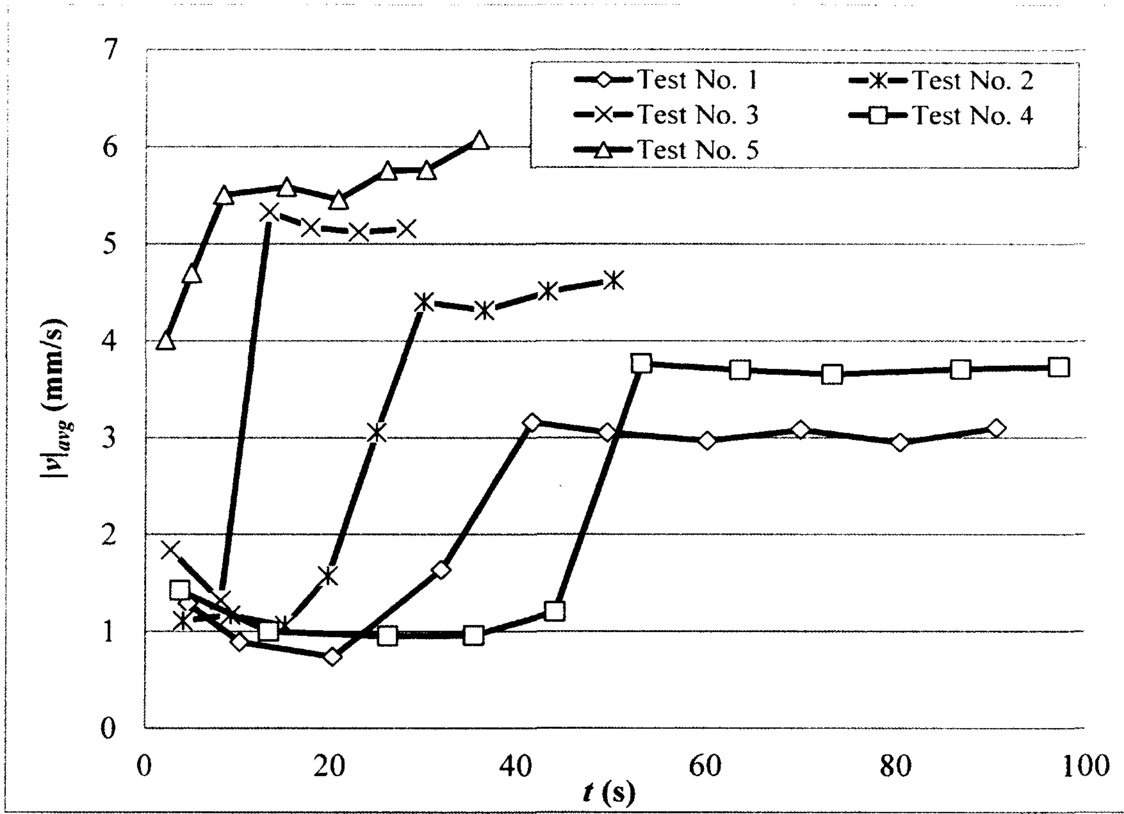

Figure 4-6 Variation of the field average velocity of all five tests.

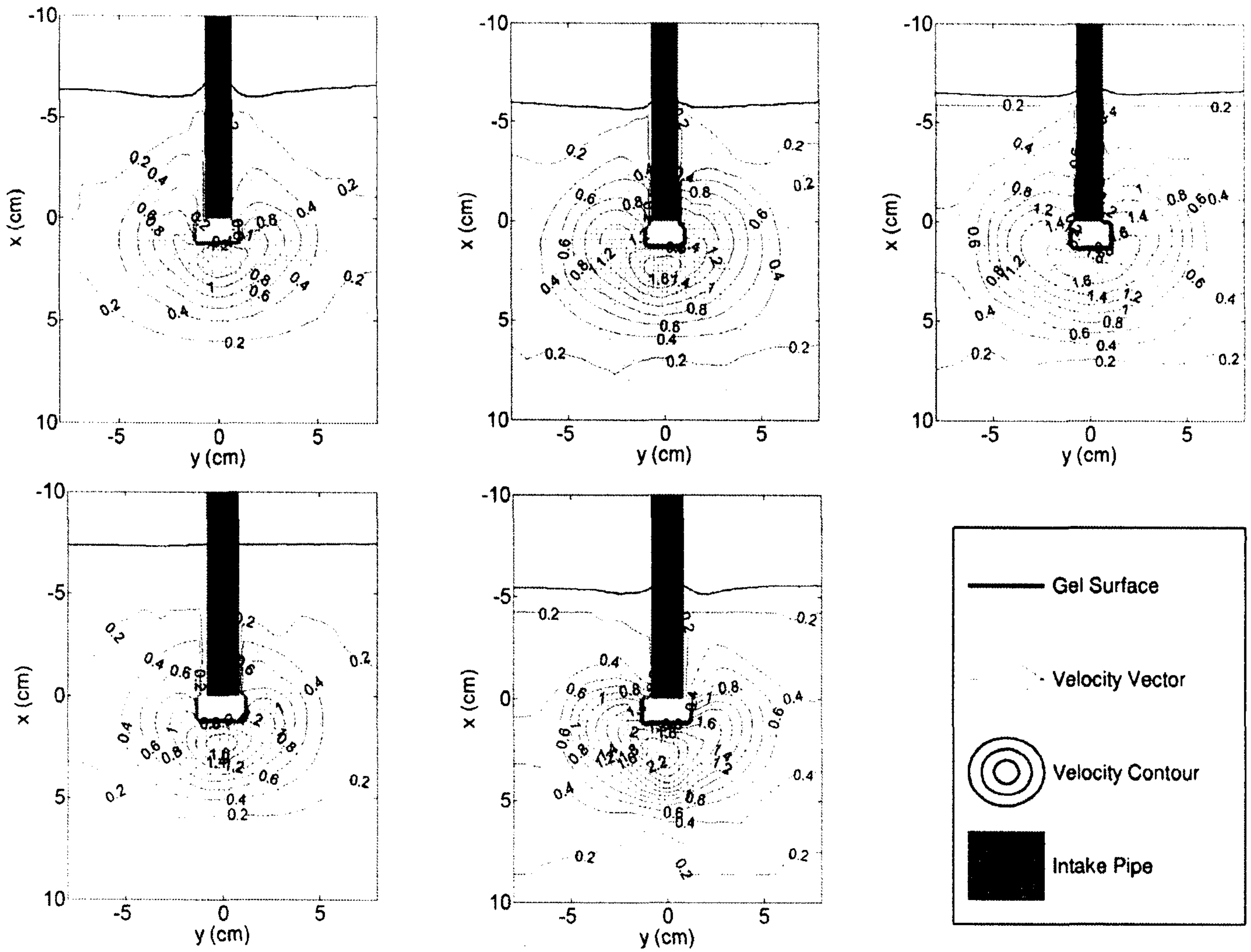

Figure 4-7 Contour plots of steady velocity field and velocity contours:

(a) ~ (e) is for Test No. 1 ~ No. 5 respectively. Velocity is in the unit of cm/s.

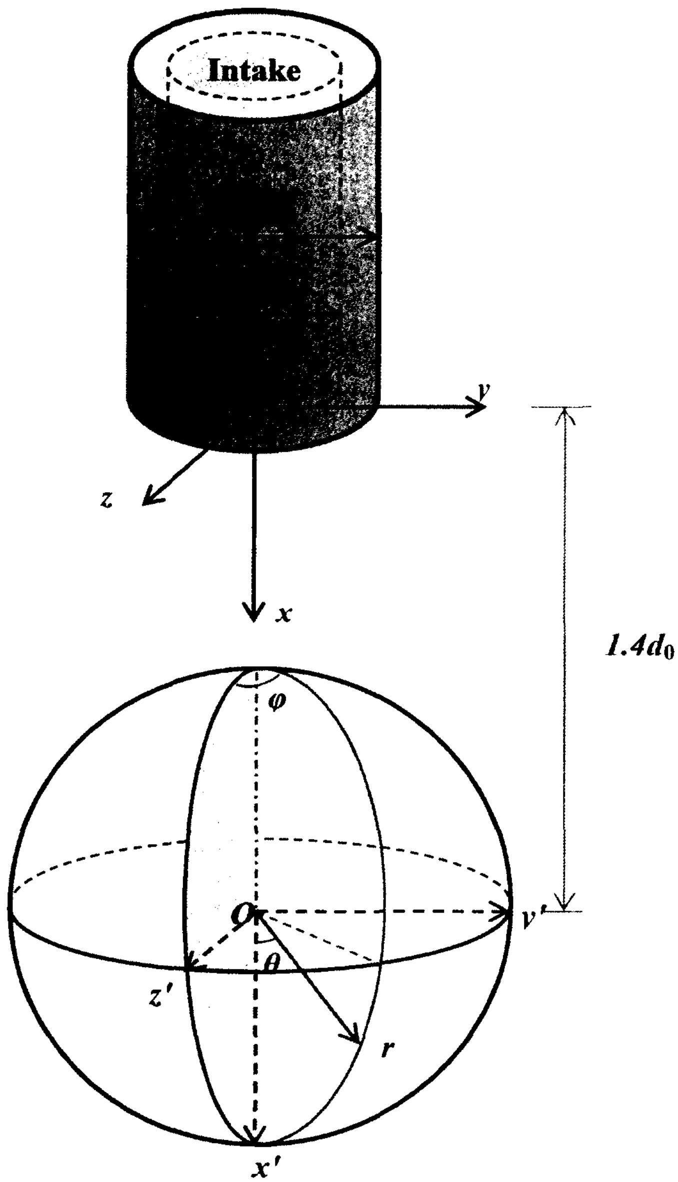

Figure 4-8 The Cartesian and spherical polar coordinate system.

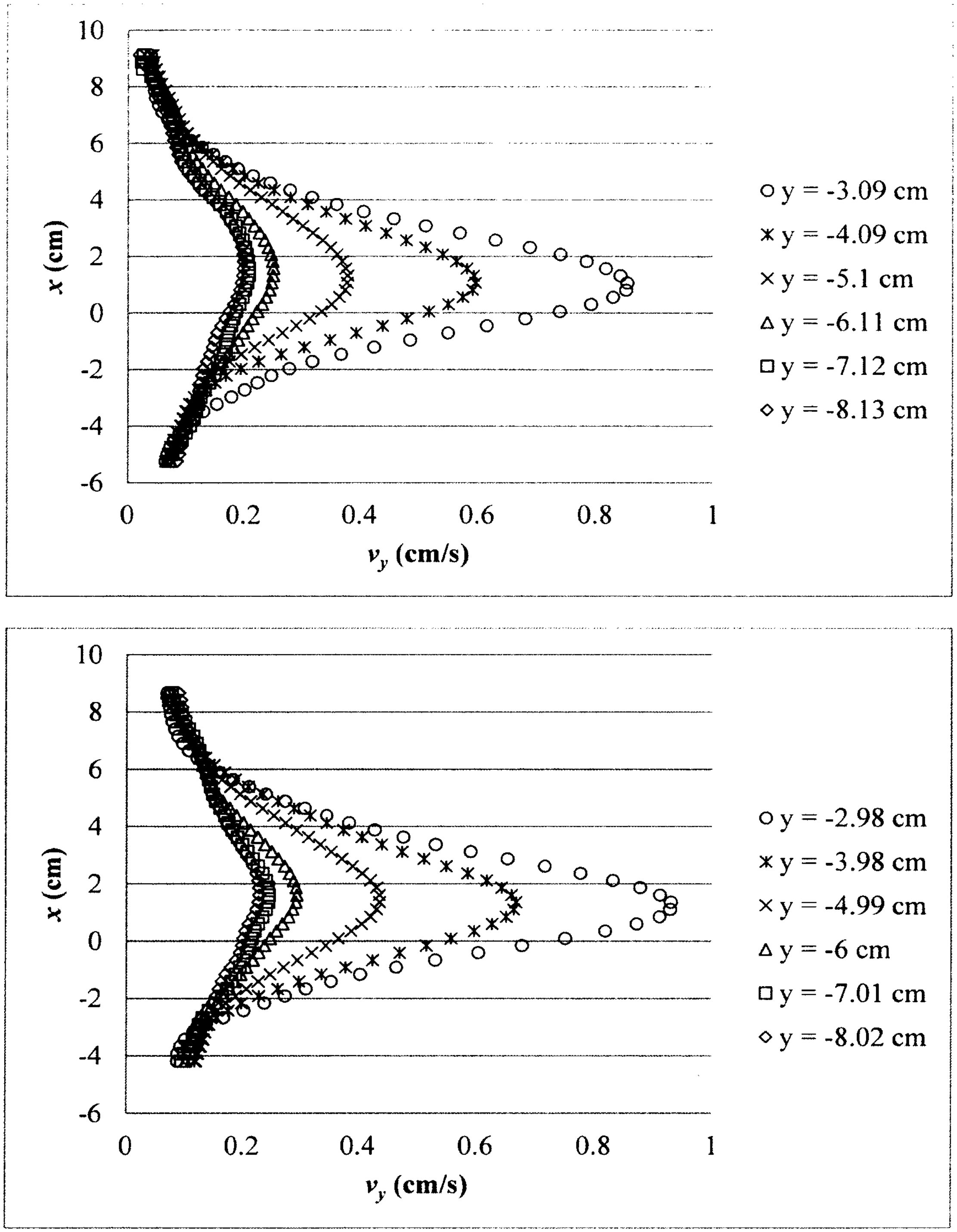

Figure 4-9 Horizontal velocity components along the *x*-axis at different *y* locations for test No. 1 and No. 4.

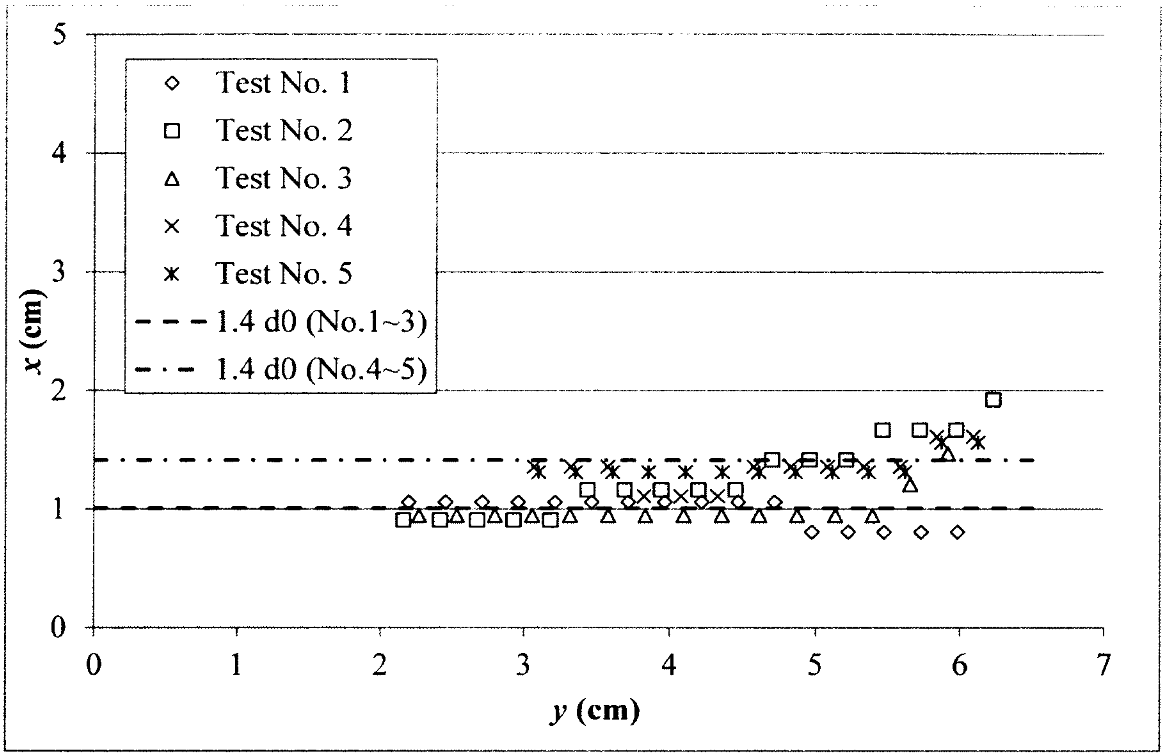

Figure 4-10 The locations of maximum horizontal velocity components.

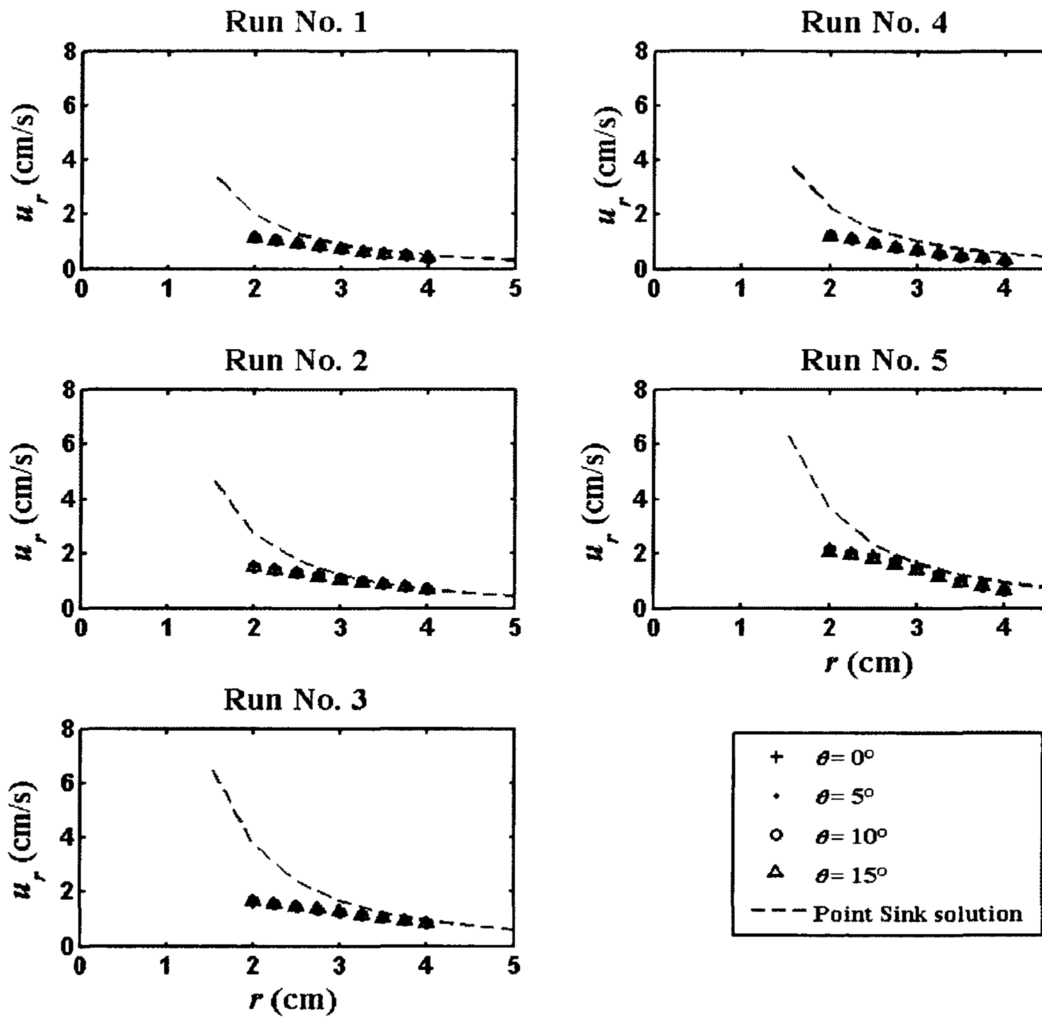

Figure 4-11 Radial velocity in the conical region of all five tests.

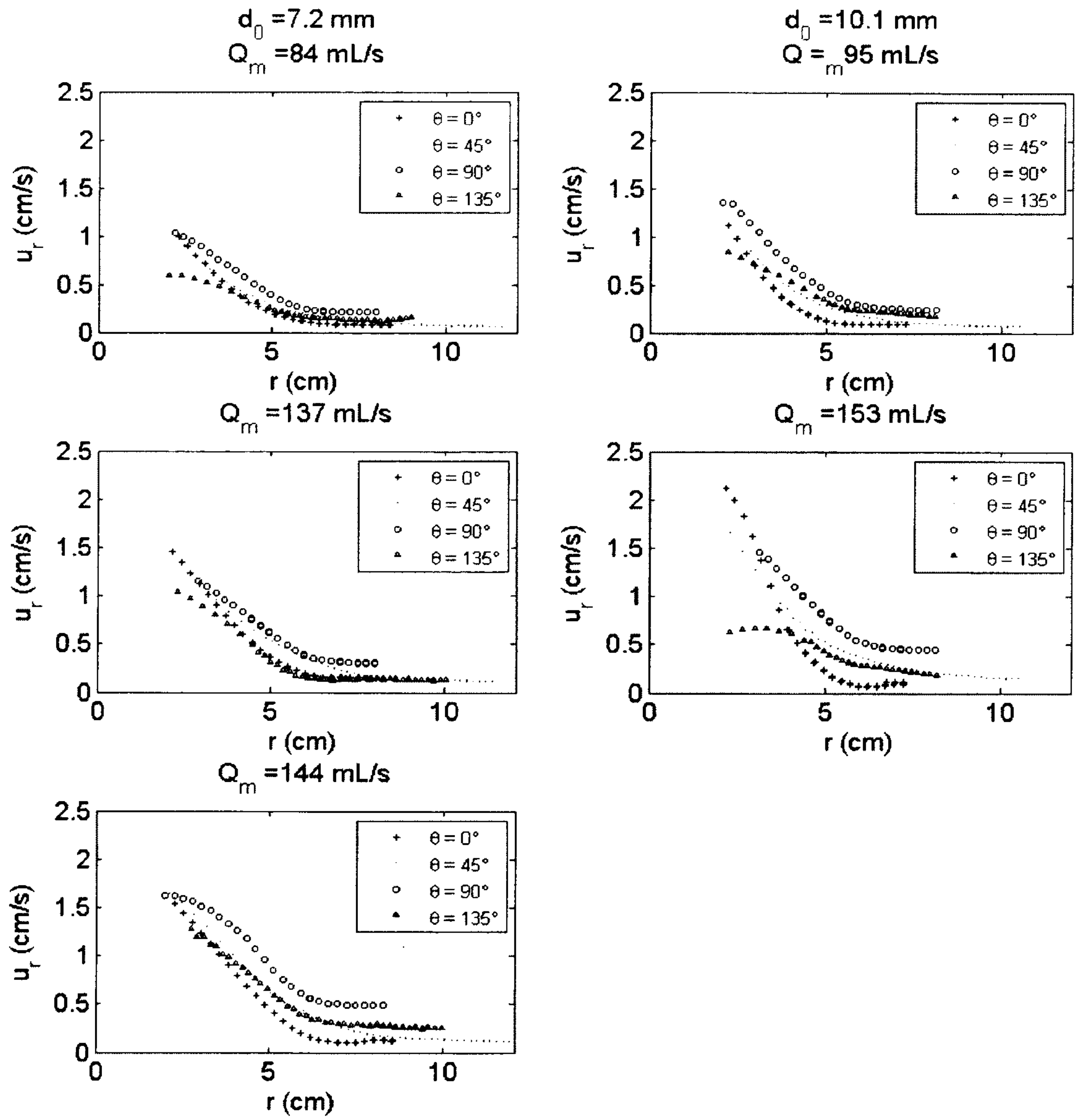

Figure 4-12 Radial velocity at different angular directions.

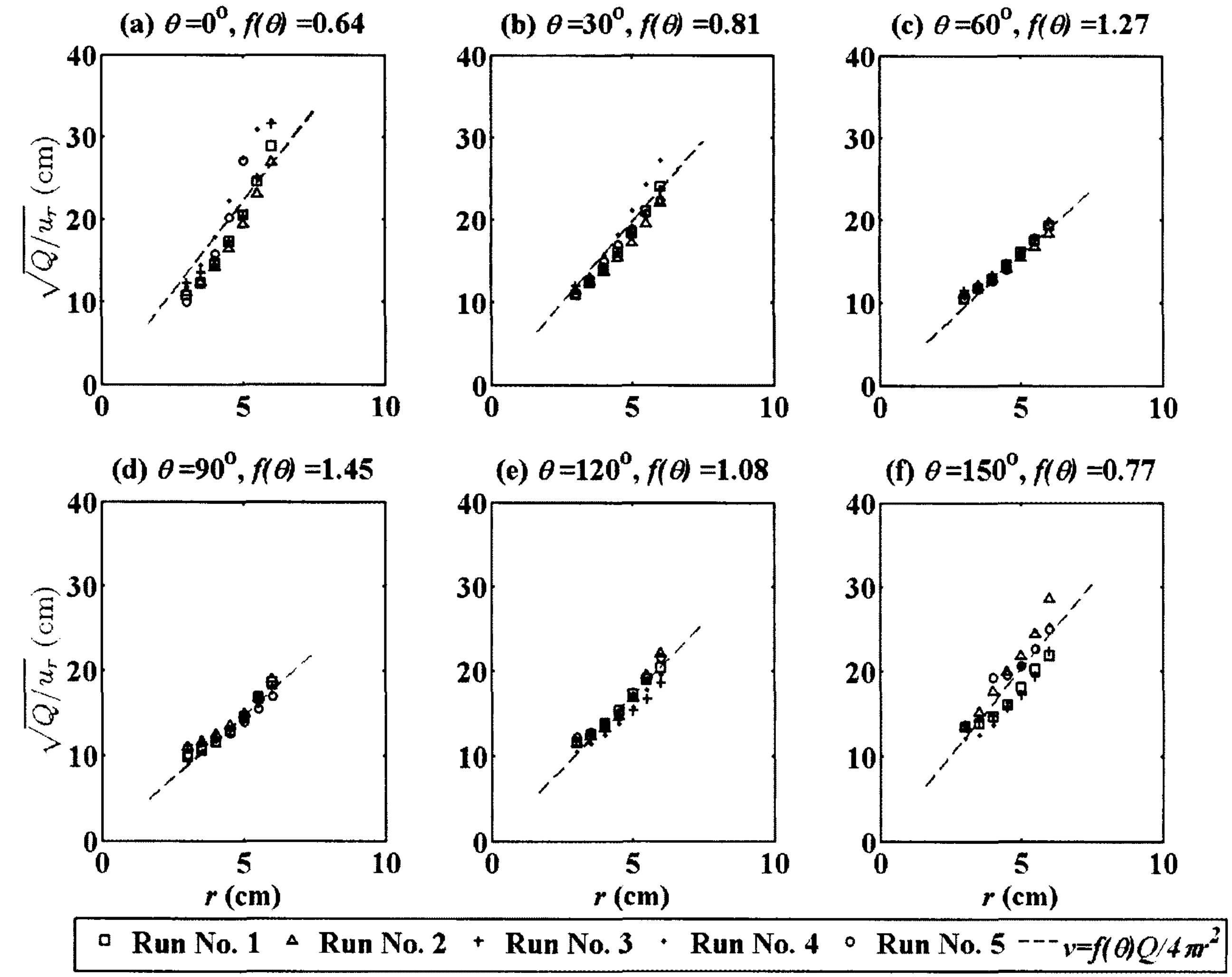

Figure 4-13 Radial velocity at different angles.

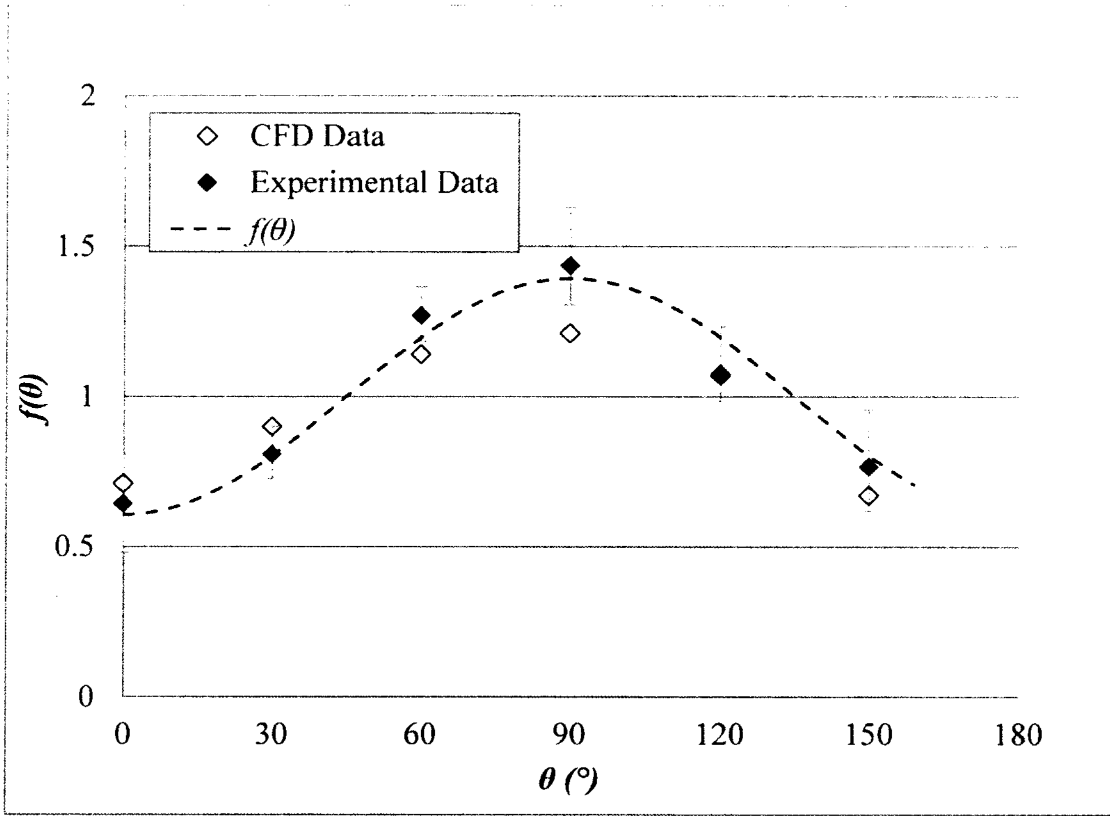

Figure 4-14 The variation of *f(θ)* with *θ*.

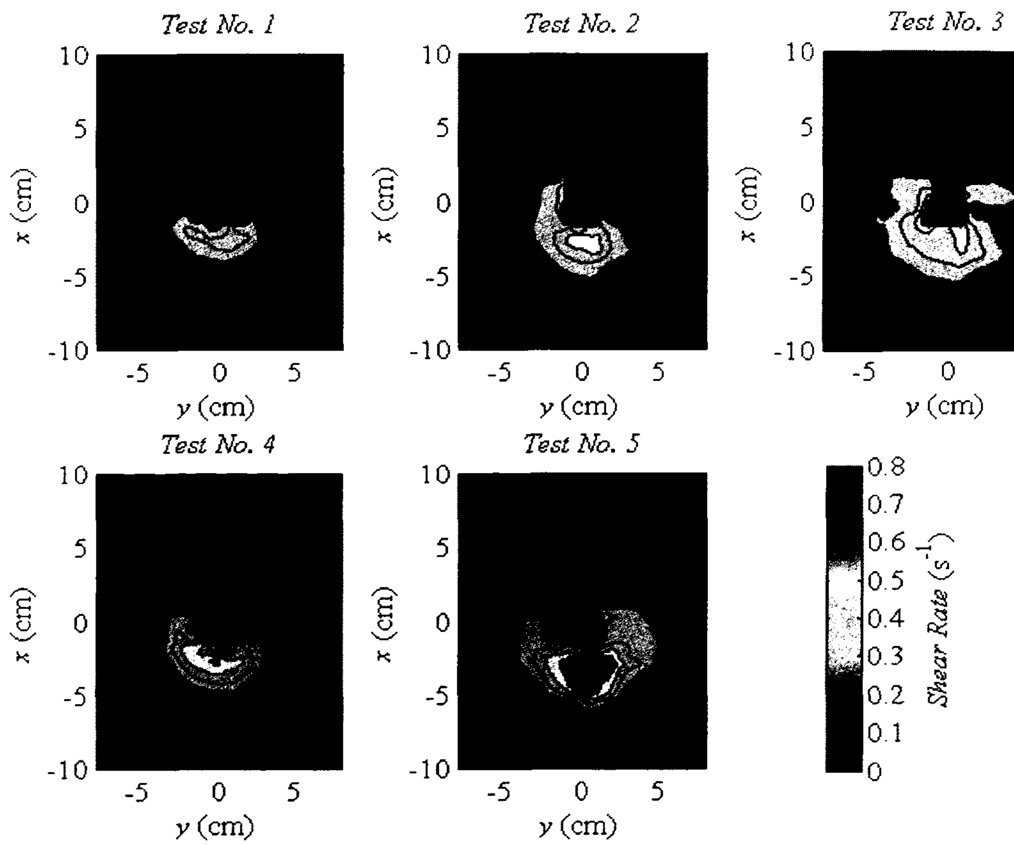

Figure 4-15 Maximum 2D shear rate contour plots for each experiment.

a)

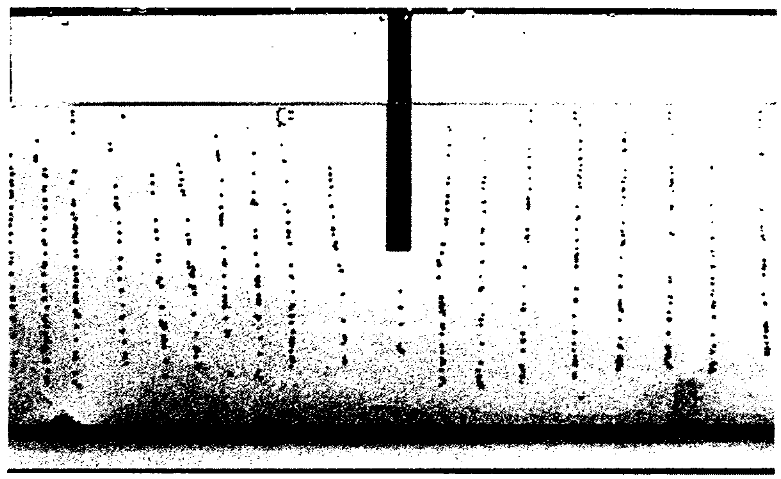

b)

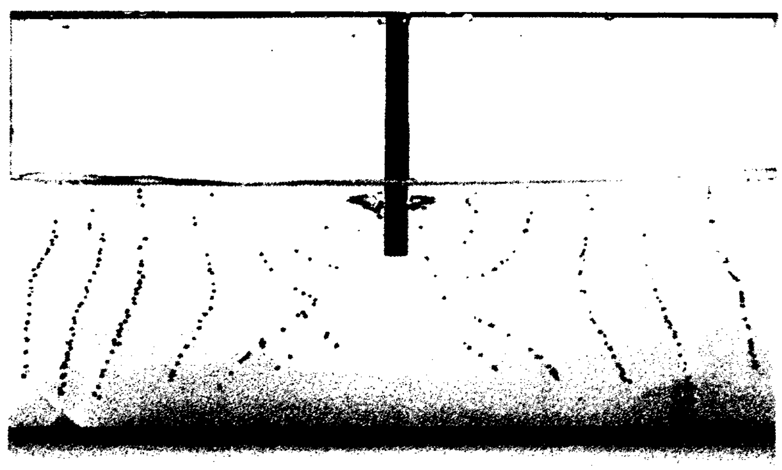

Figure 4-16 The beginning (a) and the end (b) of a random test.

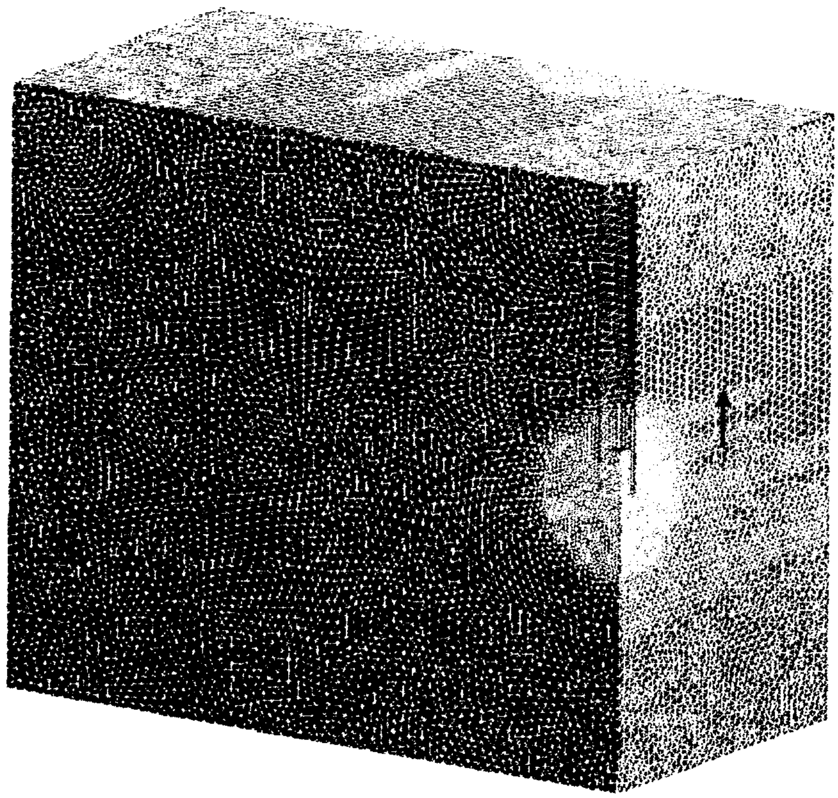

Figure 4-17 A view of the unstructured mesh and the local refinement.

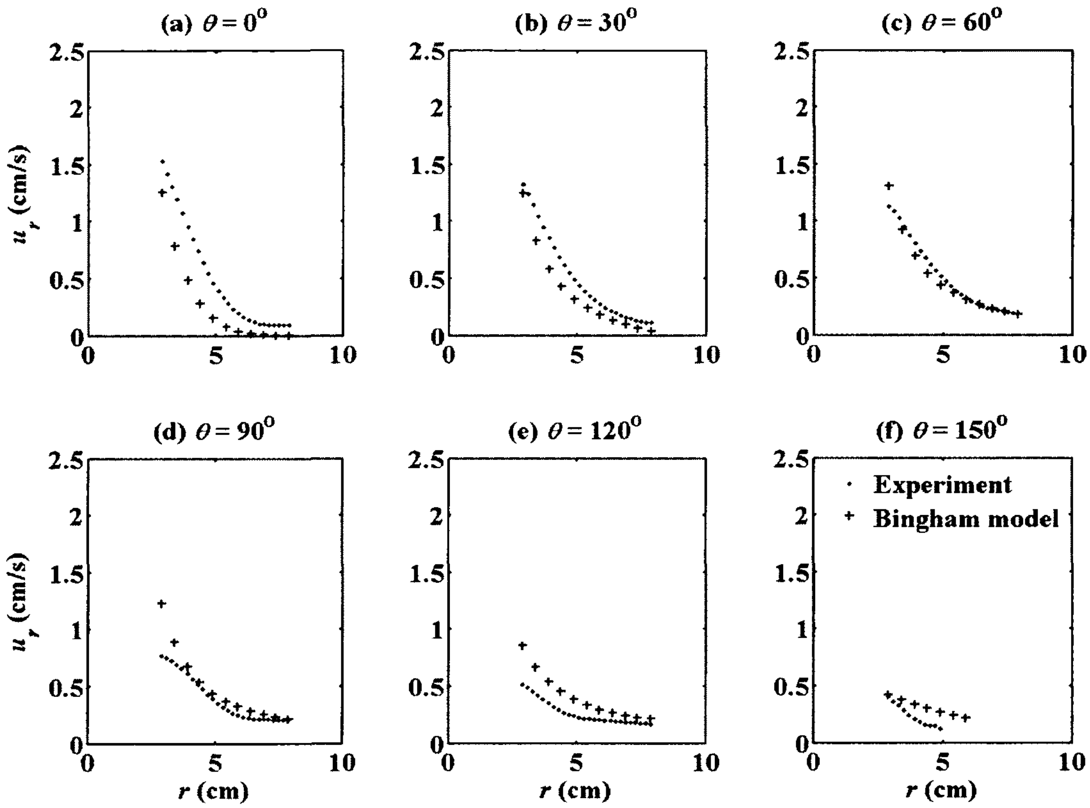

Figure 4-18 Comparison between the experimental and simulated velocity profiles for Scenario 1.

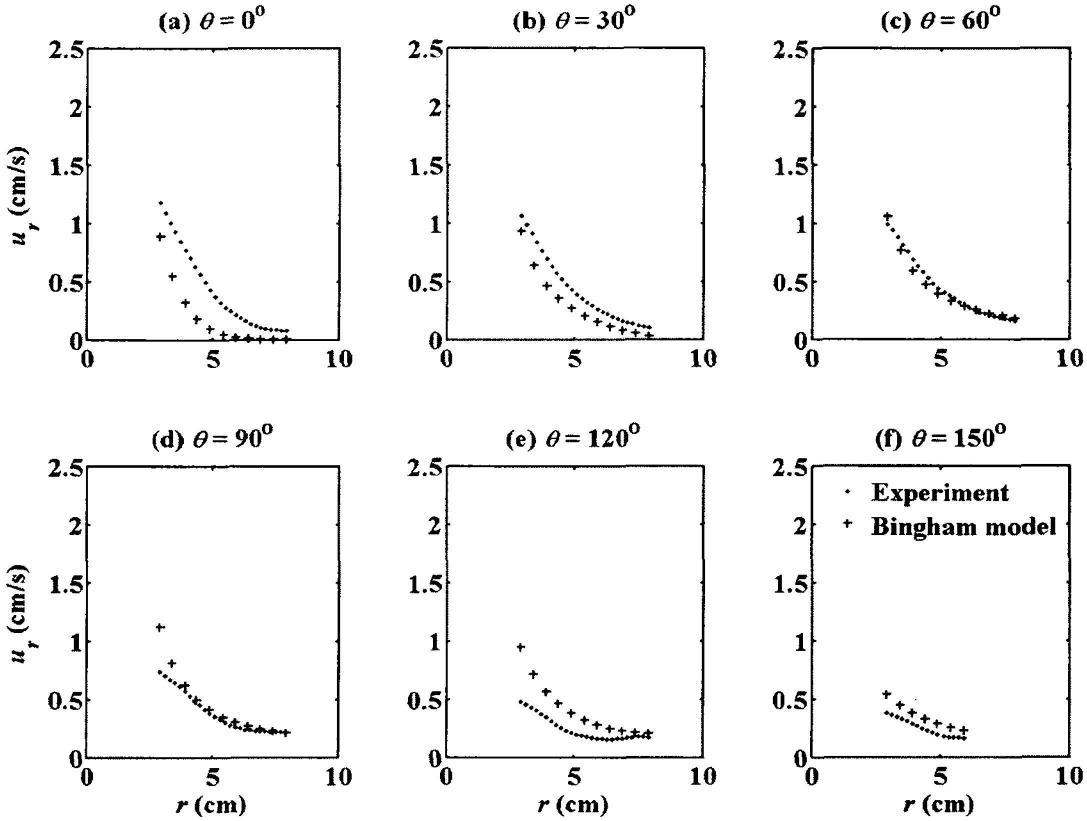

Figure 4-19 Comparison between the experimental and simulated velocity profiles for Scenario 4.

4.7 References

Banas, L. C. (1991). "Thixotropic behaviour of oil sands tailings sludge." PhD thesis, University of Alberta, Canada.

Berkenbusch, M. K., Cohen, I., and Zhang, W. W. (2008). "Liquid interfaces in viscous straining flows: Numerical studies of the selective withdrawal transition." *J.Fluid Mech.*, 613 171-203.

Blanchette, F., and Zhang, W. W. (2009). "Force balance at the transition from selective withdrawal to viscous entrainment." *Phys.Rev.Lett.*, 102(14).

Eggers, J., and Du Pont, S. C. (2009). "Numerical analysis of tips in viscous flow." *Physical Review E - Statistical, Nonlinear, and Soft Matter Physics,* 79(6).

Gamboa, J., Olivet, A., and Espin, S. (2003). "New Approach for Modeling Progressive Cavity Pumps Performance." *Proceedings - SPE Annual Technical Conference and Exhibition,* 807-815.

Graham, L. J. W., Pullum, L., Slatter, P., Sery, G., and Rudman, M. (2009). "Centrifugal pump performance calculation for homogeneous suspensions." *Can.J.Chem.Eng.*, 87(4), 526-533.

Hanks, R. W. (1963). "The laminar-turbulent transition for fluids with a yield stress." *AICHE J.*, 9(3), 306-309.

Jeong, J. (2007). "Free surface deformation due to a source or a sink in Stokes flow." *Eur.J.Mech.B Fluids,* 26(6), 720-728.

Li, Z., Mu, B., and Chui, S. N. C. (1999). "Rheology Behavior of Short Fiber-Reinforced Cement-Based Extrudate." *J.Eng.Mech.*, 125(5), 530-536.

Luo. G. (2004). "Investigation of CT beneath MFT deposition for oil sands tailings disposal." PhD thesis. University of Alberta, Canada.

Masliyah. J. H. (2006). "Tailings and water management.".

Mitschka, P. (1982). "Simple conversion of Brookfield R.V.T. readings into viscosity functions." *Rheologica Acta,* 21(2), 207-209.

Moreno, O. B., and Romero, M. E. M. (2007). "Integrated analysis for PCP systems." *Proceedings of the SPE Latin American and Caribbean Petroleum Engineering Conference,* 1234-1243.

Papanastasiou, T. C., Georgiou, G. C., and Alexandrou, A. N. (2000). *Viscous fluid flow.* CRC Press, Boca Raton.

Robinson, A., Morvan, H., and Eastwick, C. (2010). "Computational investigations into draining in an axisymmetric vessel." *J Fluids Eng Trans ASME,* 132(12).

Seepex GmbH. "Operation and Maintenance Manual." http://www.seepex.com/ 2011).

I. Southern Clay Products. (2006). "Product Bulletin/Laponite®." http://www.laponite.com/index.asp.

Tadmor, Z., and Gogos, C. G. (2006). *Principles of polymer processing / Zehev Tadmor, Costas G. Gogos.* Hoboken, N.J. : Wiley-Interscience, c2006; 2nd ed., Rev. ed, .

Teran, J., Fauci, L., and Shelley, M. (2008). "Peristaltic pumping and irreversibility of a Stokesian viscoelastic fluid." *Phys.Fluids,* 20(7).

Widjaja, J., Samali, B., and Li, J. (2003). "Electrorheological and Magnetorheological Duct Flow in Shear-Flow Mode Using Herschel-Bulkley Constitutive Model." *J.Eng.Mech.*, 129(12), 1459-1465.

Wilkinson, W. L. (1960). *Non-Newtonian fluids; fluid mechanics, mixing and heat transfer.* Pergamon Press, New York.

Xue, M., and Yue, D. K. P. (1998). "Nonlinear free-surface flow due to an impulsively started submerged point sink." *J.Fluid Mech.*, 364 325-347.

Yamada, K. (1999). "Computation for Rheological Phenomena of Elastic-Viscoplastic Body." *J.Eng.Mech.*, 125(1), 11-18.

Zhang, G., Zhang, M., Yang, W., Zhu, X., and Hu, Q. (2008). "Effects of non-Newtonian fluid on centrifugal blood pump performance." *Int.Commun.Heat Mass Transfer*, 35(5), 613-617.

Zhou, D., and Feng, J. J. (2010a). "Selective withdrawal of polymer solutions: Computations." *J.Non Newtonian Fluid Mech.*, 165(15-16), 839-851.

Zhou, D., and Feng, J. J. (2010b). "Selective withdrawal of polymer solutions: Experiments." *J.Non Newtonian Fluid Mech.*, 165(15-16), 829-838.

Zhou, Q. N., and Graebel, W. P. (1990). "Axisymmetric draining of a cylindrical tank with a free surface." *J.Fluid Mech.*, 221 511-532.

Chapter 5 Experimental Study on Pumping Water-capped Viscoplastic Fluids[4]

5.1 Introduction

Pumping of MFT is an important issue related to tailings ponds reclamation and tailings management. In Alberta, the land area currently covered by tailings ponds is more than 170 km^2 (Alberta Government). After the initial settling period in the ponds, tailings separate from the top layer of water to form a mid-layer of MFT, which can be removed for further treatment and thickening. However, the difficulty is how to withdraw MFT efficiently without disturbing the upper water layer.

In stratified fluids, the minimum submerged depth of the intake in the lower layer fluid to avoid withdrawing the upper layer fluid is known as "critical submergence", h_c. An early study by Harleman *et al.* (1959) on bottom withdrawal from a vertically stratified fluid suggested that the relative critical submergence h_c/d_0 (d_0 is the internal diameter of the intake pipe) is proportional to the withdrawal flow rate but increases when d decreases. Lubin and Springer (1967) considered the formation of a dip on the interface of a two-layer system draining from a tank and discovered a similar result as that of Harleman *et al.*'s study. Sharp and Parchure (1991) proposed a 1% mixing theory to define the

[4] A version of this chapter will be submitted as a journal paper.

critical drawdown for two layers withdrawal and gave a modified formula to predict h_c based on their laboratory experiments.

Whether the intake is partly or fully submerged (Sharp and Parchure 1993), the vertical distance between a raised intake and the bed or the clearance also plays a role in defining the critical drawdown condition under which the drawdown of the upper layer is incipient. When the intake is capped with a plate or a collar, Sharp and Parchure (1993) and Sharp *et al.* (1996) showed that although the intake structure has some effects on the critical condition, the surface layer drawdown is independent of the internal geometry of the intake.

Kocabaş and Ülker (2006) and Kocabaş *et al.* (2009) investigated the impact of different parameters on the critical submergence for an intake in a stratified fluid media. They varied the thickness of upper layer fluid, the clearance of the intake position, the withdrawed flow rate from the intake pipe and applied an Artificial Neural Network (ANN) and a Neuro-Fuzzy model to predict the critical submergence.

However, little knowledge is available concerning the subject of pumping non-Newtonian fluid, in particular the viscoplastic flow with existing yield stress. It is known that the pipe flow of non-Newtonian fluids is different from the Newtonian fluids. Zhou and Feng (2009) reported the surface deformation of a non-Newtonian fluid-gas sink flow and showed that the effects of elasticity on the critical submergence. Furthermore, how the yield stress affects the flow field induced by the intake is worthwhile to investigate.

Tailings management has become one of the most difficult environmental challenges for the oil sands processing. The objective of this study is to experimentally investigate the critical condition of withdrawing water-capped artificial MFT and the flow evolution of both fluids during the progress. It aims to improve the understanding of pumping process in oil sands tailings ponds.

5.2 Experiment Design

One set of experiments was performed to observe the interface development when a vertical intake pipe was placed in the lower gel layer while capped with a layer of water. Another set was to detect the velocity field near the intake during the pumping process. As described in chapter 4, the 48 hours old 3% Laponite gel was used in all our experiments to simulate the rheological behaviour of MFT, with the yield stress τ_0= 15.2 Pa and plastic viscosity μ_p= 0.018 Pa·s, in terms of the Bingham plastic model $\tau = \tau_0 + \mu_p \dot{\gamma}$.

An experimental setup is shown in Figure 5-1. All our experiments were carried out in glass tanks with a dimension of 60 cm (width) by 30 cm (depth) by 52 cm (height). 3% Laponite gel was made by mixing the Laponite powder with demineralised water by weight. The procedure is described in chapter 4. About 40 hours after mixing, the yield stress started to build up and the gel was ready to trap small particles. Then a circular vertical pipe was slowly inserted into the center of the tank with an initial submergence of h_1 and the clearance of h_2 from the bottom. The other end of the pipe was attached to the inlet of a progressive cavity pump (PCP) and the outlet went into the drainage.

To insert black seeds in the center plane across the tank, a syringe with an attached rigid tube was used to pick up pre-mixed gel-seed mixture and inject seeds into the gel. A light sheet produced from a slit using a slide projector was used to only illuminate the center plane so that all seeds were put in place. The seeds were always added starting from the far end of the tank in order not to block any light in the near field close to the light sheet. Later a layer of dyed water was gently added to cap the gel through a piece of foam, which allowed very gentle flow of water to get through and form a clear interface between water and gel. The depth of upper layer water is h_w.

In our experiments, the size of the intake was changed to test its impact on the results. The inner and outer diameters of the intake pipes are denoted as d_0 and d_1 in Table 5-1, which shows all the experimental details. In this table, Q_m is the measured steady pumping flow rate, and it was varied for each test. The Reynolds number is calculated as $\mathrm{Re}_B = \dfrac{\rho_g d_0 V_0}{\mu_p}$ for Bingham plastic fluids, where V_0 is the average velocity at the intake and ρ_g is the density of 3% Laponite gel at room temperature (= 1,003 kg/m^3). The Hedstrom number ($He = \dfrac{d_0^{\,2} \rho_g \tau_0'}{\mu_p^2}$) and the critical Reynolds number $(Re_B)_c$ are obtained to verify the flow regime (Hanks 1963). All tests are found running in the laminar flow zone with $Re_B < (Re_B)_c$.

Tests No. 1 ~ 6 are designed to monitor the interface development between gel and water without adding tracking seeds in the gel. In each test, a video camera was utilized to record the pumping process from the front wall of the tank with a grid sheet attached. This sheet was used to calibrate the physical scales from the video images, to calculate the pumping rate at different time and to examine the distortion of the frames. It is found the distortion of the images is within 2% spatially; so for the image post-process, linear conversion was applied. The outer diameter of the intake, d_1, is used as a measurement to compute the scale of examining parameters at the center plane of the tank, which is also assumed to be a constant for each test.

In tests No. 7 ~ 10, black seeds were added as tracing particles and a CCD camera (PULNIX TM-1400CL) was used to track all the movement of these seeds during pumping. The camera has a resolution of 1392×1040 pixels. Among these four tests, No. 7 is a repeat of No. 2 with slight differences of initial intake submergence and the intake clearance. Since it can be treated as an axisymmetric flow, the observation window was only focused on half of the domain near the intake. From the side wall of the tank, a video camera was set to detect the surface dropping for the purpose of discharge measurement. A ruler was placed in the view of the observation window after pumping and thereby the conversion parameter can be determined.

To analyse the velocity field of water-capped gel during pumping, the commercial image processing software by LaVison®, called Davis 8, was utilized to analyse all the images for tests No. 6 ~ 10. This package is able to process low seeding density images given its function of the Particle Tracking Velocimetry method. As only the lower layer was seeded by tracing particles, the velocity of water layer could not be detected.

5.3 Results and Discussions

5.3.1 Flow evolution

In this study, each test was carefully prepared to avoid strongly disturbing the lower layer of gel. After the preparation, the PCP was started to withdraw from the tank until the surface of the fluid dropped to the intake level or very little discharge was detected at its outlet. In the beginning of each test, only gel can be withdrawn from the tank as the interface of water and gel was all above the intake level and only clear flow was detected at the outlet. As volume of the gel decreased, the interface started to deform, especially in the central region. It gradually reached the level of intake in the center and the upper layer water started to be extracted along with gel too. After that both water and gel were withdrawn by the pump with water discharge dominated. Thereby the colour of the flow at the pump outlet darkened. However, once the volume of water running out, the pump was able to only withdraw gel since it was no longer covered by water. Also the outflow cleared up again.

5.3.1.1 Interface deformation

Water-capped gel sitting in the tank forms a water-gel two layer system. In general, the selective withdrawal in stratified liquid-liquid system falls into three regimes: subcritical, critical and supercritical. In subcritical regime, only the liquid in the layer where the intake is located can be withdrawn, while for supercritical flow, liquids from both layers are able to enter the intake. The critical stage is recognized as the threshold of transition from the subcritical to the supercritical stage, when the second liquid is just starting to be extracted by the intake (Zhou and Feng 2010). In our experiments, the initial submergence of the intake was tested and it was always deep enough to prevent the supercritical flow to happen at the beginning, so only lower layer gel was withdrawn for a period of time after pumping initiated. This subcritical period would continue until water was taken by the pump when the supercritical stage started. The critical stage is defined as the moment when the upper layer water was just starting to get into the intake pipe entrance. The submerged depth of the intake in gel at this moment is named as the critical submergence.

The first set of tests (No. 1 ~ 6) was specifically conducted to study the interface development during pumping process. In all our tests, the interface of water and gel deformed gradually until the critical stage was attained. After that the deformation rate slowed down as upper layer water started to leak through the intake. Images in Figure 5-2 are an illustration of interface changing, which are selected from test No. 2 at different time after the pump was turned on. It clearly shows the evolution of the deforming process moving from subcritical (from a to

c) to critical stage (d) further to supercritical stage (from e to i). It also indicates that the intake pipe has some impact on the interface profiles during the subcritical stage: there is a heart-shape zone above the intake which was not sheared. This differs from the flow field created in Newtonian media or fluids without any yield stress, which extends to the whole domain. However, in the case of a viscoplastic liquid, it no longer shears as soon as the prevailing stress level drops below the value of the yield stress, and it will behave like a solid (Chhabra 2007).

As defined in chapter 4, a 3D Cartesian coordinate system is applied with its origin located at the center of the entrance of the intake pipe, x-axis going downwards and $z = 0$ across the center plane of the tank (see Figure 5-1).The water surface is monitored during the whole process and can be used to compute the total volume of gel and water removed by the pump. On the other hand, the profiles of interface deformation allow us to calculate the changes in the volumes of gel from one step to another. A set of these profiles are plotted in Figure 5-3. In subcritical stage (from 30s to 119s), the gap is relatively even and wider than that of the later stages, which tells a constant but bigger volume of gel is withdrawn. When the gap starts getting narrower, the smaller amount of gel has been withdrawn during a time interval from between two profiles. Furthermore, if we take the average value of the space between each profile as the uniform dropping down distance, Δh, and assume the volume is forced down uniformly in the whole tank area, then we can estimate the volume of the gel reduced between two profiles as well as the flow rate of gel. The estimation is shown in Figure 5-4 a), wherein the filled blocks display the water discharge and the blanks are for gel discharge.

In a PCP system, the production is based on the pump rotation frequency and the fluid it works on. At a fixed rate it can have a different pumping rate depending on the type of the fluid. In our experiments, the PCP system was set at a fixed rotation rate for each individual test, so that at the subcritical stage, the pumping discharge is stable once the yield stress of the gel was overcome; but at the supercritical stage, water was also withdrawn and the viscosity of the gel-water mixture was changed. This is the reason that the total discharge increases first then decreases when water discharge increases and the mixed fluid becomes less viscous. For example, in Figure 5-4 a) the water discharge began to increase from 0% at the critical stage to over 90% towards the end of the test. The rest three tests follow the same trend as presented in Figure 5-4 b), c) and d).

5.3.1.2 Velocity Index

The second set of tests (No. 7 ~ 10) in this study was designed to detect the velocity field of lower layer gel during pumping. A group of raw images taken for test No. 10 with a time interval of 40 s is presented in Figure 5-5. The subcritical stage, as shown in images a) to c), critical stage, image d), and supercritical stage from image e) to l) are displayed in this figure. Part of the interface of gel and colored water is also visible from image c) to j), which unveils that the withdrawal process started from pumping gel exclusively, moved to take both of gel and water, then back to drain gel only. The interface is getting flatter very slowly once the critical stage was passed since gel was continuously being taken by the pump and the hydrostatic pressure drove the interface down. However, the discharge of the gel is not large compared with that of the water. So the curving of the interface is not changing dramatically.

For the image process, the two zones are masked out: the area blocked by the intake pipe and the area would possibly be covered by dyed water in the later stage. A typical velocity field with a contour plot of the velocity vectors is shown in Figure 5-6, which contains a number of N velocity vectors. The field average velocity, $|V|_{avg} = \frac{\sum_{i=1}^{N} |V|_i}{N} = \frac{\sum_{i=1}^{N} \sqrt{v_{x_i}^{\ 2} + v_{yi}^{\ 2}}}{N}$, is used as an index to measure the flow intensity of the whole domain, similar to what is defined in chapter 4. It varies with time and the variation is plotted in Figure 5-7.

The fluctuation of $|V|_{avg}$ in Figure 5-7 indicates the evolution of the pumping process, which is also indicated by interface changing in Figure 5-5. Similar to the single layer gel pumping flow in chapter 4, at subcritical stage, the gel would reach a stable stage with a sudden growth after the commencement of pumping. However, once the supercritical stage was attained, gel and water were both withdrew from the intake. Then gel discharge decreased rapidly because water is less viscous and easier to drain. The decrease rate depends on the pumping discharge and size of the intake entrance. The smaller the entrance and the faster the pump rotates, the larger the decrease rate is resulted in. It is as big as

90.5% in test No. 7 which is a combination of the smallest intake and highest discharge. But for wider intakes and smaller flow rate, the decrease rate of this index is not very significant. It is only reduced by 46.4% in test No. 10, which is related to the biggest intake and smallest pumping discharge.

5.3.2 Critical submergence

All the videos for test No. 1 ~ 6 are broken down into series of frames from where the critical stage could be found. One example picture of the critical stage is shown in Figure 5-2 d). The water layer was colored so that the interface of water and gel could be easily detected. For each test at the critical stage, the interface was identified visually in the image based on pixel values. It was recorded as a group of pixel locations and then converted into physical positions in the unit of millimeter, as presented in Figure 5-8. It is shown that the slope of the interface is not changing with the diameter of the intake, but with the pumping discharge. For the same size of the intake (test No. 1 ~ 3), the higher the discharge is, the steeper the interface curves, and therefore the bigger the critical submergence requires. On the other hand, under comparable discharge (test No. 1, 4 and 6), the interface curving in the region near the intake is found to be similar, which indicates the impact of intake size on the interface deformation is not important compared with that due to discharge variations. Based on this, we propose a length scale h^* to group our data, $h^* = \left(\frac{Q_m}{\sqrt{g'}}\right)^{2/5}$.

When the critical submergence of each test is normalized by h^*, it appears to be a constant, 1.24, and it is not sensitive to the densimetric Froude number, $F = \frac{V_0}{\sqrt{g' d_0}}$ as demonstrated in Figure 5-9. In this figure, h_c/h^* starts to increase a bit with F is around 260, which is related to test No. 3. This might be due to the boundary condition given the discharge is relatively high compared to other five tests. As a result, the functional relationship for the critical submergence can be written as

$$h_c = 1.24 \left(\frac{Q_m}{\sqrt{g'}} \right)^{2/5} \tag{5-1}$$

For selective withdrawal of Newtonian two-layer stratified fluids, the critical submergence depends on the location of the intake, the withdrawal flow rate and the density difference between two fluids, as stated in some earlier investigations (Harleman et al. 1959; Lubin and Springer 1967; Sharp and Parchure 1993; Davidian and Glover 1956; Wilhelms et al. 1985). The results of most of these studies (see Figure 5-9) can be generalized as,

$$\frac{h_c}{h^*} = \alpha \cdot F^{\beta} \tag{5-2}$$

in which α and β are coefficients differed in each study, where α varied from 0.17 to 0.83, and β was typically either 0 or 0.1.

When the intake is located at the lower layer, $\beta = 0$, the normalized critical submergence becomes a constant and it is independent of the densimetric Froude number. In one case of withdrawing from the upper layer (Davidian and Glover 1956), $\beta = 0.1$, the dependence of h_c/h^* on the Froude number is very weak as the exponent is relatively small. It indicates that the withdrawal of two-layer Newtonian fluids is simply controlled by the forcing discharge and the density difference between two layers. Thereby the following function is generated based on Equation (5-1) and (5-2),

$$h_c = \alpha \cdot \left(\frac{Q_m}{\sqrt{g'}} \right)^{2/5} \tag{5-3}$$

The coefficient α in Equation (5-3) is found to be different with various setups and boundary conditions. In unbounded condition, Craya (1949) applied Bernoulli equation on the interface and analytically derived that $\alpha = 0.69$ in the case of selective withdrawal from a horizontal intake located on a vertical boundary. Gariel (1949) experimentally confirmed the analytical findings of Craya. Lawrence and Imberger (1979) later reported a value of $\alpha = 0.52$ by several axisymmetric two-layer withdrawal experiments. Later Wilhelms *et al.* (1985) generalized a result that can be applied on all two-layer stratification withdrawal, which can be rewritten as

$$h_c = 0.69 \cdot \left(\frac{\pi}{\theta}\right)^{2/5} \left(\frac{Q_m}{\sqrt{g'}}\right)^{2/5} \tag{5-4}$$

where θ is the angle of withdrawal in radians. When compared with this study, the same axisymmetric condition should be applied with $\theta = 2\pi$, and it can be shown that $\alpha = 0.52$. However, in the present study $\alpha = 1.24$ when the lower layer is occupied by a viscoplastic fluid. This value is 138% higher than that in Equation (5-4), which is used when both layers are Newtonian fluids.

When the liquid depth is limited by boundaries and withdrawal happens at the bottom, the value α is found to be greater than unbounded withdrawal. Harleman *et al.* (1959) analytically and experimentally investigated a two-layer axisymmetric system and found that $\alpha = 0.83$. Lubin and Springer (1967) reported $\alpha = 0.69$ in their study on the formation of a dip at the interface of two layers draining from the bottom. Wilhelms *et al.* (1985) also worked on the bottom withdrawal and finalized a function, rewritten as

$$h_c = 1.09 \cdot \left(\frac{\pi}{\theta}\right)^{2/5} \left(\frac{Q_m}{\sqrt{g'}}\right)^{2/5} \tag{5-5}$$

Again when $\theta = 2\pi$, $\alpha = 0.82$ in Equation (5-5). These investigations of critical submergence are all less than our result.

In addition, while the clearance of the intake, h_2, rises from 0, the critical submergence, h_c, decreases. The falling rate is as big as 18% when h_2/d_0 increased from 0.5 to 2.3 as shown by the Sharp and Parchure (1993). The value of α is respectively 0.58, when h_2/d_0 = 0.5; and 0.49 when h_2/d_0 = 2.3. But when h_2 reaches the height of h_c, it has no impact on the critical stage and h_c is not affected by it. In our setup, the intake was always kept far enough away from the tank bottom that the boundary effect of the bottom is not significant. Thus our observation indicates that the critical submergence in viscoplastic fluid is at least 2.5 times of that in normal selective withdrawals in Newtonian systems.

5.3.3 Interface and discharge variation

5.3.3.1 Interface variation

During pumping process, the interface of gel and water changes spatially and temporally. In the far field away from the intake, the interface is flatter than that within the near field. The temporal variation of interface in the far field is also lower than the change near the intake. The height of the far-field interface is linearly related to the operation time at the subcritical stage. This can be shown by Figure 5-10, which presents the temporal variation of the depth of gel above the intake level, h_g in test No. 2, 5 and 6. The filled symbols are used to indicate the critical stage in each test and to separate the subcritical and supercritical stages. At the subcritical stage, the linear relationship of h_g and t indicates a constant discharge of gel, and the slope of the data is related to the magnitude of this discharge. However, at the supercritical stage, h_g does not drop with time constantly, but slows down as a power function of t. The power of t ranges between -1.3 for test No. 6 and -2.6 in test No. 5.

Another dataset of test No. 3 in chapter 4 is also included in Figure 5-10. It is an example to show the temporal variation of h_g in the experiment on pumping from a single gel layer. Here h_g decreases with a constant rate until it has been all taken out, similar to what happens at the subcritical stage in two-layer pumping.

The interface development in Figure 5-3 shows that in the beginning of the subcritical stage, the interface uniformly spreads out along y-axis. It is comparable to the profile of gel surface in the tests of pumping single layer of gel (see Figure 5-11). But while it gets closer to the critical stage, the water-gel interface changes dramatically in the zone near the intake. Images taken by CCD camera (test No. 7 ~ 10) provide a close observation of the interface development in the near field.

With reference to Figure 5-5, the interface of water and gel is digitalized and the positions are recorded as shown in Figure 5-12, where the filled bars are used to indicate a half body of the intake pipe in test No. 10. In this figure, the interface dropped slowly in the direction of x-axis, and somehow uniformly along y-axis in the beginning. But when water front was getting lower and closer to the intake level, the interface in the near field started to accelerate and form a sudden shearing zone along the intake pipe. In contrast, the far-field interface barely changed its position.

The speed of the water front, V_f, is found to increase while water travelling down until it became close to the intake level, then it changed direction and turned into the intake abruptly. Figure 5-13 is a plot containing the frontal velocity of interface along x-axis direction in all four tests.

However, when compared with Figure 5-8, the interface profile at the critical stage in Figure 5-12 indicates a big difference from the prediction by Equation (5-1), which is based on the tests without seeding. To verify the impact of seeding process on the results, test No. 7 and No. 9 were repeated three times with different seeding spacing and timing. The pumping discharges of these two tests are comparable (see Table 5-1). Figure 5-14 presents three interface profiles of water and gel in the repeated tests at the critical stage. It is shown that the seeding has negligible impact on the critical stage given these three profiles are very similar and close to each other. However, the critical submergence is almost doubled the value by Equation (5-1), which indicates there is some uncertainty about the expression. One possible reason is that the diffusion of the dye in the lower layer gel created a false interface, the critical submergence was thus underestimated. On the other hand, the definition of the critical stage is difficult when the water discharge is low and the interface is hard to be detected.

5.3.3.2 Gel and water discharges

In section 3.1.1, the discharges of gel and water are estimated based on the surface and interface dropping information as presented in Figure 5-4. During the experimental process, these discharges change with the depth of gel above the intake level, h_g. Their variations in test No. 2, 5 and 6 are plotted in Figure 5-15. It is again shown that the discharge of gel is stable before the critical stage is reached, then decreases continuously with the dropping of the gel depth, while the discharge of water starts to increase from zero. The decreasing rate of gel discharge and the increasing rate of water discharge depend on the value of h_g in the supercritical stage, and linear relationships may apply.

5.3.4 Velocity field

As described in 3.1.2, $|V|_{avg}$ is computed as an index to show how fast gel flows during the whole pumping process. It appears that there is a stable stage before the upper layer water started to be drain from the intake (see Figure 5-7). In this section, the velocity field of this stable stage will be discussed.

5.3.4.1 Horizontal component

In a 3D Cartesian coordinate system as defined in Figure 5-1, $z = 0$ is the center plane across the tank. In this plane, the horizontal and vertical velocity components, v_y and v_x, are computed. The results show that, no matter what the pumping discharge is, the maximum value of v_y is always located around the same height, which is $1.4d_0$ below the intake entrance level. As a result, when the difference is removed, all x locations of maximum v_y at different y locations should be at the same level (see Figure 5-16). Consequently the origin in spherical polar coordinates is assumed to locate along the centerline of the intake pipe and 1.4 d_0 below the entrance level. This result is no different from that of the tests on pumping a single layer of gel as discussed in chapter 4.

5.3.4.2 Radial velocity

If we assume an axisymmetric flow along x-axis and there is only radial flow, then the radial velocity can be expressed by the following equation

$$u_r = \frac{f(\theta)}{r^2} \cdot \frac{Q}{4\pi} = f(\theta) \frac{Q}{4\pi r^2} \tag{5-6}$$

or

$$\sqrt{\frac{Q}{u_r}} = \sqrt{\frac{4\pi}{f(\theta)}} \cdot r = K \cdot r \tag{5-7}$$

Equation (5-7) shows a linear relationship of $\sqrt{Q/u_r}$ and r, and $K = \sqrt{4\pi/f(\theta)}$. For all four tests, the radial velocities are plotted together in Figure 5-17 in terms of different values of θ. A trend line is applied to fit all the spots and the slope K is used to calculate $f(\theta)$ when θ varies. The dashed line displays the best fitted data of $f(\theta)$. At $\theta = 150^\circ$, only part of the data near the intake area were used for the calculation, because when it is getting close to the water-gel interface, the velocity of gel is interrupted and it becomes bigger than the result under our assumptions.

Figure 5-18 is another view of the variation of $f(\theta)$ with θ, in which the error bars are generated by fitting each data set individually for all tests. In the range of 0° to 150°, $f(\theta)$ increases from 0.55 at $\theta = 0^{\circ}$ to the maximum value of 1.58 when $\theta = 120^{\circ}$, then decreases while $\theta = 150^{\circ}$. It indicates more flow from the upper body (when $\theta \geq 90^{\circ}$) of the gel, which differed from the withdraw process of pumping single layer of gel while flow majorly fed by the side (when $\theta = 90^{\circ}$). It should also be noted that at $\theta = 0^{\circ}$ and $\theta = 30^{\circ}$, $f(\theta)$ only changes slightly from 0.55 to 0.60, combing the deviation of $f(\theta)$ is relatively wide at $\theta = 30^{\circ}$, so we could conclude that radial velocity barely changes within the cone shaped zone of $0^{\circ} \leq \theta \leq 30^{\circ}$. In the experiments of pumping pure gel, this zone is limited in $0^{\circ} \leq \theta \leq 15^{\circ}$.

5.3.4.3 Velocity change

The radial velocity of gel in the supercritical stage is found to differ from the velocity in the subcritical stage. Figure 5-19 displays the variation of $f(\theta)$ with the experimental process in test No. 10. Three stages are presented in it: a) stable stage of withdrawing gel only; b) withdrawal of both gel and water; c) withdrawal of gel again after water has been all taken out by pump. The experimental result of chapter 4 for pumping single layer gel is also listed in the figure. The maximum radial velocity is along $\theta = 150^{\circ}$ at subcritical stage, and moves to $\theta = 90^{\circ}$ when the depth of water decreased to zero and gel started to be withdrawn.

5.3.5 Similarity to seepage flow

The flow of viscous fluid between two plates is found to be similar to that of fluids through porous media, e.g. groundwater flow. The "hydraulic conductivity" in this case can be calculated based on the space between the plates and the viscosity of the fluid (Marino and Luthin 1982). Our results at the critical stage also share some similarity to the seepage flow. If the specific discharge or section average velocity is defined the same as the groundwater flow, it is known as

$$V_s = \frac{Q_m}{A} = \frac{Q_m}{2\pi y(|x| + h_2)} \tag{5-8}$$

The hydraulic gradient $J = \Delta h/y = \Delta x/y$ is then found to increase with V and the relationship is presented in Figure 5-20.

Usually Darcy's law is suitable when applied to seepage flow which is in the laminar zone. However as the specific discharge increases, the relationship between the specific discharge and the hydraulic gradient gradually deviates from the linear relationship expressed by Darcy's law (Bear 2007). The non-linear relationships reported in the literature mostly follow a general form of $J = mV + nV^k$ and in many cases k = 2. This manner is used to fit our data in Figure 5-20 and it shows a good agreement when m = 0.46 and n = 0.40.

5.3.6 Scour by water

In the pumping process the interface position near the intake is similar to scour. The scouring depth of water in gel is found at the maximum value when water discharge reached the maximum point. After that, the interface starts to flatten out and the scour depth decreased gradually, as shown in Figure 5-12.

At the maximum erosion depth (see Figure 5-21), the water changes its flowing direction within a distance of the pipe thickness $\frac{d_1 - d_0}{2}$. The variation of velocity is $V_w + V_s$, if V_s and V_w are both the absolute value of the water velocity. So the shear stress of water acting on the interface equals

$$\tau = \mu \dot{\gamma}_w = \mu \left(\frac{V_w + V_s}{\frac{d_1 - d_0}{2}} \right) = \frac{2\mu (V_w + V_s)}{d_1 - d_0} \tag{5-9}$$

In Equation (5-9), the maximum value of V_s is used for the calculation. With respect to V_w, we assume the total discharge of water and gel at supercritical stage are the same as that of pumping gel along at subcritical stage and the reduce rate of gel as shown in Figure 5-7 is substituted by water.

The erosion depth of water in gel is found to increase linearly with the shear stress of water flow (see Figure 5-22) because this give a measure of the shear stress of water applies on gel and balanced with the yield stress of the gel.

5.4 Summary

In this study, we examined the interface deformation, the critical submergence and the velocity field of the withdrawal of a two-layer Newtonian and non-Newtonian liquid system. Three stages were discussed: the subcritical stage of only taking upper layer gel, the supercritical stage for withdrawing from both layers and the critical stage as the transition from one to the other.

At the subcritical stage, the discharge of gel is stable after a sudden rise in the beginning. The deformation of the water-gel interface is relatively uniform in the far field, but changes rapidly with time and space in the near field. At the critical stage, the gel discharge decreases while water is starting to be withdrawn. The critical submergence for preventing water leaking is found to increase with the pump flow rate but not sensitive to variable intake sizes. It is proportional to the flow rate to the power of 2/5. At the supercritical stage, both water and gel are withdrawn. The deformation of the interface then slowed down. Furthermore, the radial velocity varies at different angel and it is independent of the intake size. However, it changes with the time after the stable subcritical stage.

5.5 Notation

d_0	Inner diameter of the intake pipe
d_1	Outer diameter of the intake pipe
F	Densimetric Froude number
h_1	Initial submergence of the intake in the gel
h_2	Distance from the intake to the bottom of the tank
h_c	Critical submergence
h_g	The depth of gel above the intake level
h_w	The depth of the water layer
He	Hedstrom number
K, k, m, n	Constant coefficients
N	The number of velocity vectors
Q	Steady pumping discharge
$Q_{g,w}$	Discharge of gel or water at supercritical stage
Q_m	Measured steady pumping rate
R	Radius in spherical coordinates
Re_B	Bingham Reynolds number
$(\mathrm{Re}_B)_c$	Critical Reynolds number corresponding to the Hedstrom number
t	Time from the commencement of pumping
$u_{r,\theta,\varphi}$	Velocity components in spherical coordinate system
v_x	Vertical component of 2D velocity
v_y	Horizontal component of 2D velocity
V_0, V_f, V_w	Velocity in the intake pipe, frontal velocity of water or inteface and water velocity at intake
$\lvert V\rvert_{avg}$	Field average velocity
x, y, z	Cartesian coordinates
α, β	Constant coefficients
μ_p	Plastic viscosity
τ	Shear stress
τ_0	The value of yield stress which fits the viscosity measurements
τ_0'	The measured yield stress

$\dot{\gamma}$	Shear rate
$\boldsymbol{\theta}, \boldsymbol{\varphi}$	Spherical coordinates

Table 5-1 Experimental parameters.

No. 1 ~ 6 for interface changing; No. 7 ~ 10 for particle tracking. Test No. with * are repeated.

No	d_0 (mm)	d_1 (mm)	Q_m (ml/s)	V_0 (m/s)	h_1 (cm)	h_2 (cm)	h_w (cm)	Re_B	He	$(Re_B)_c$
1	7.2	13.8	133	3.28	18.4	21.1	7.7	1297	1988	2300
2*	7.2	13.8	173	4.27	19.7	19.8	8.0	1689	1988	2300
3	7.2	13.8	215	5.31	18.5	21.0	8.0	2100	1988	2300
4	10.1	17.1	131	1.64	20.2	19.5	7.5	912	3922	2900
5	10.1	17.1	206	2.58	20.2	19.5	7.5	1435	3922	2900
6	15.1	21.4	135	0.76	19.7	20.0	7.5	629	8795	3200
7*	7.2	13.8	173	4.28	18.3	21.2	8.0	1695	1988	2300
8	7.2	13.8	190	4.69	19.5	19.5	4.5	1855	1988	2300
9*	10.1	17.1	178	2.23	20.3	19.1	7.7	1239	3922	2900
10	15.1	21.4	95	0.53	18.2	21.2	8.0	441	8795	3200

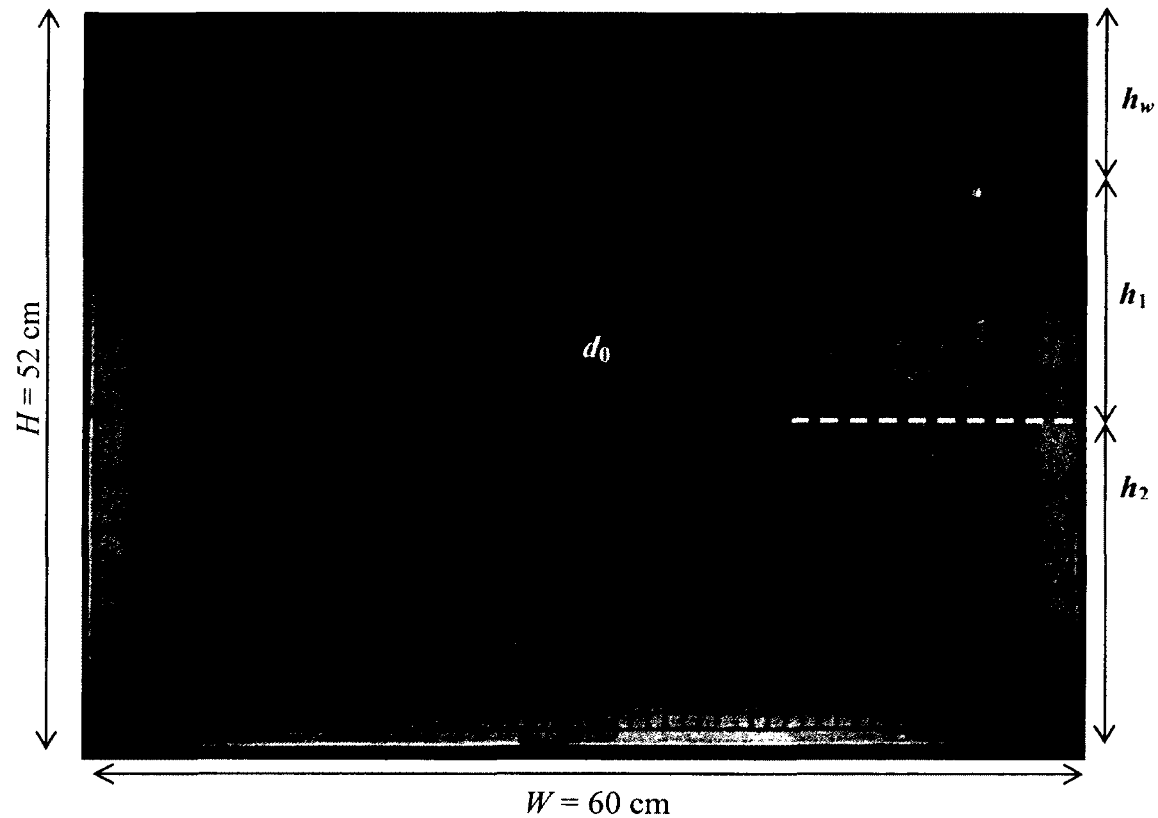

Figure 5-1 Scheme of the experimental setup for water-gel pumping.

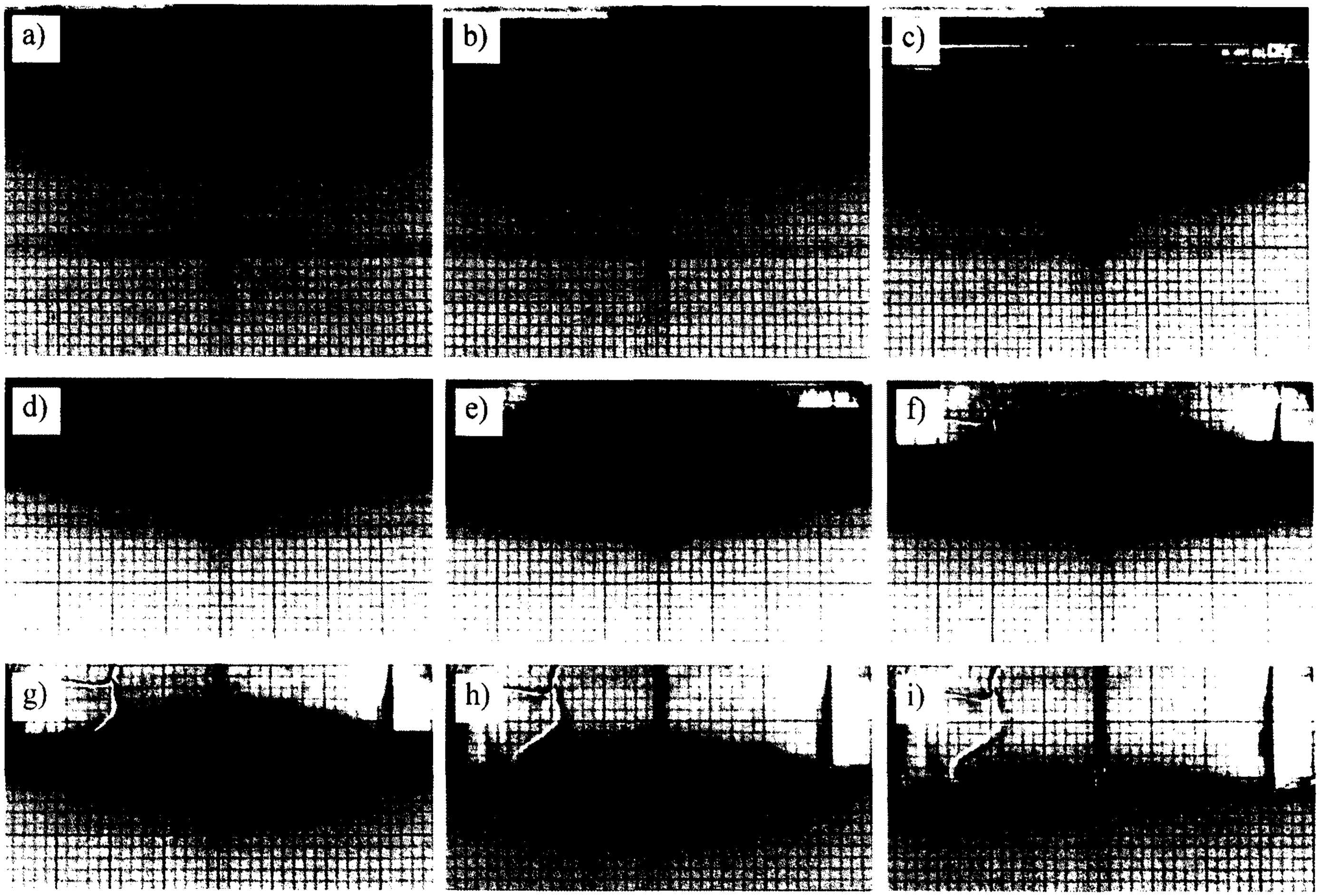

Figure 5-2 The evolution of interface deformation of test No. 2 at a time interval of 30 seconds: a) 30 s, b) 60 s, c) 90 s, d) 119 s: the critical stage, e) 150 s, f) 180 s, g) 210 s, h) 240 s and i) 259 s: the end of the test.

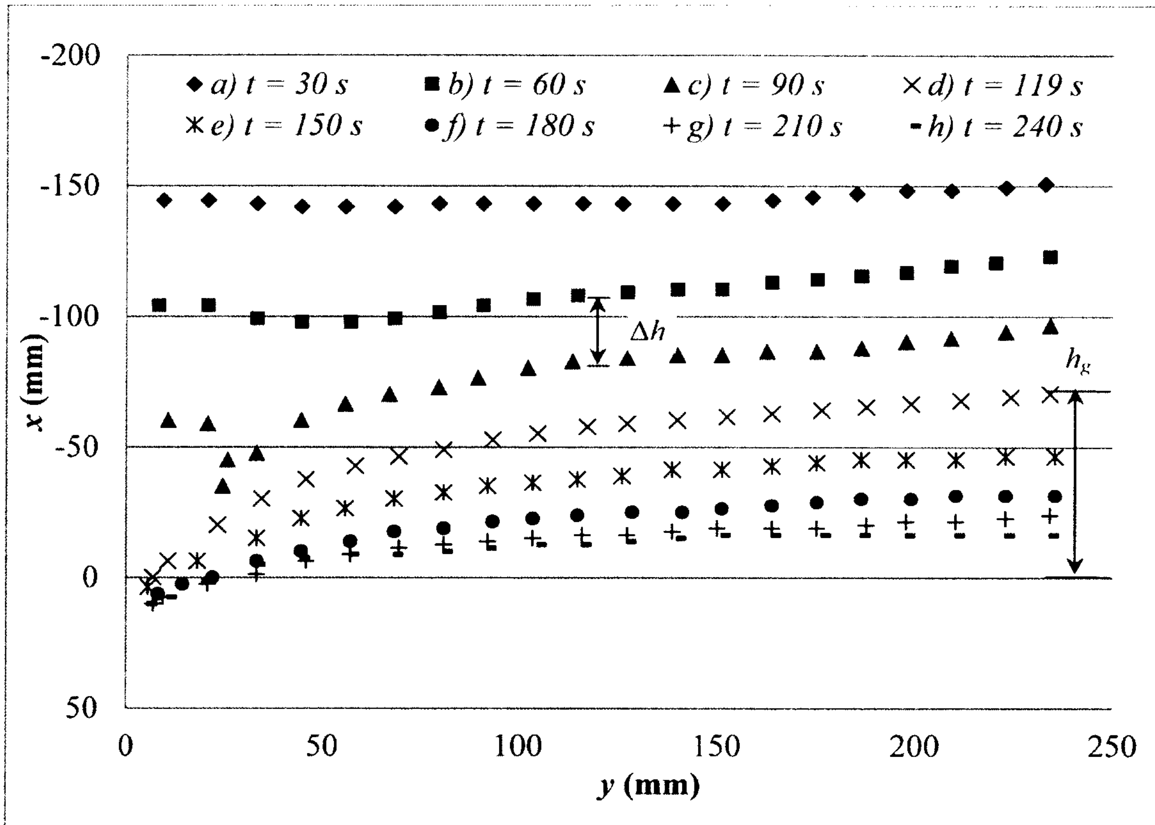

Figure 5-3 The profiles of interface deformation in test No. 2 at different time corresponding to each sub-image in Figure 5-2.

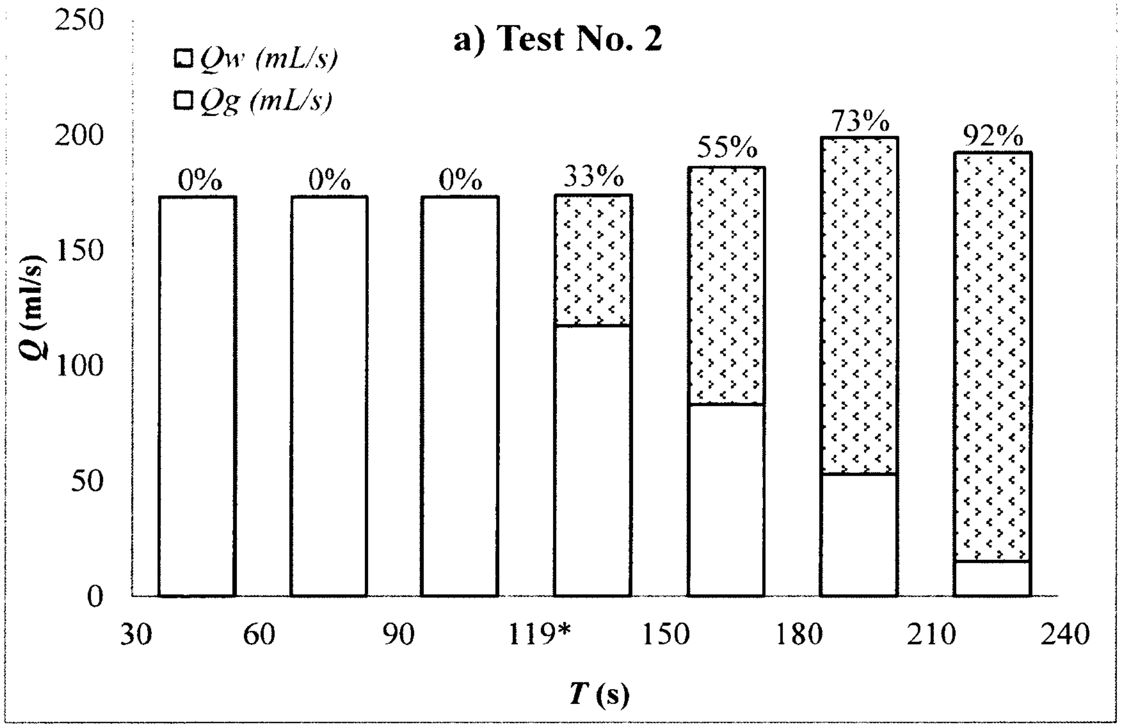
a) Test No. 2
Qw (mL/s)
Qg (mL/s)
Q (ml/s)
T (s)
250
200
150
100
50
0
30
60
90
119*
150
180
210
240
0%
0%
0%
33%
55%
73%
92%

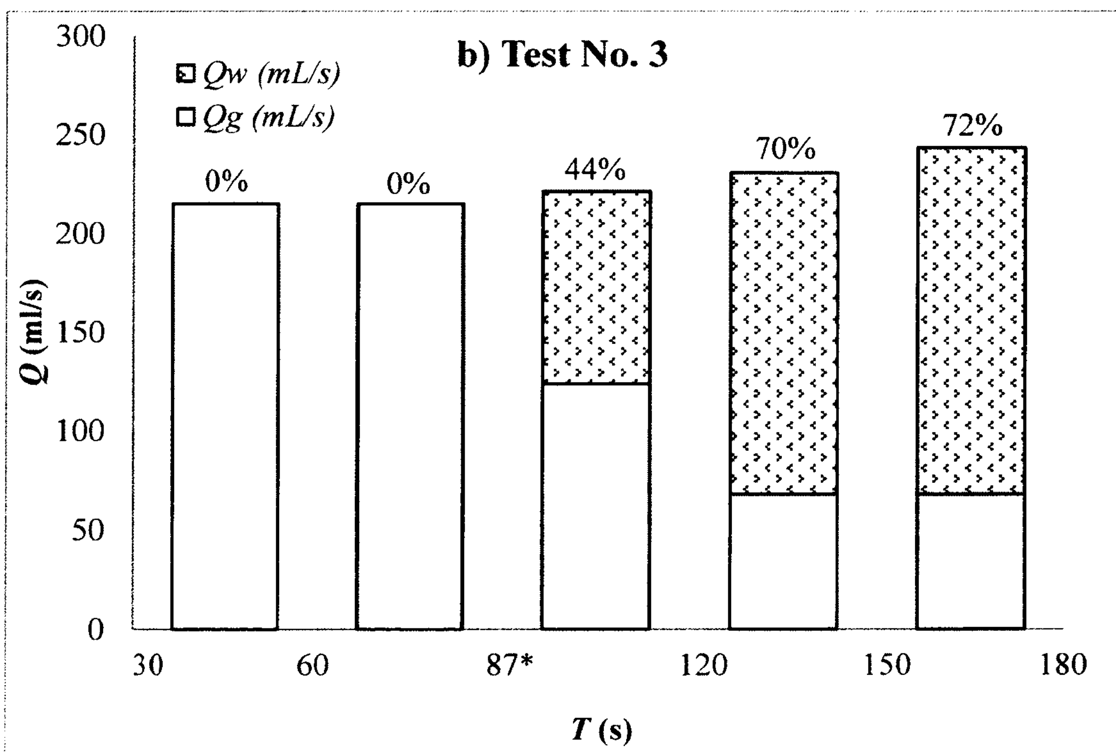
b) Test No. 3
Qw (mL/s)
Qg (mL/s)
Q (ml/s)
T (s)
300
250
200
150
100
50
0
30
60
87*
120
150
180
0%
0%
44%
70%
72%

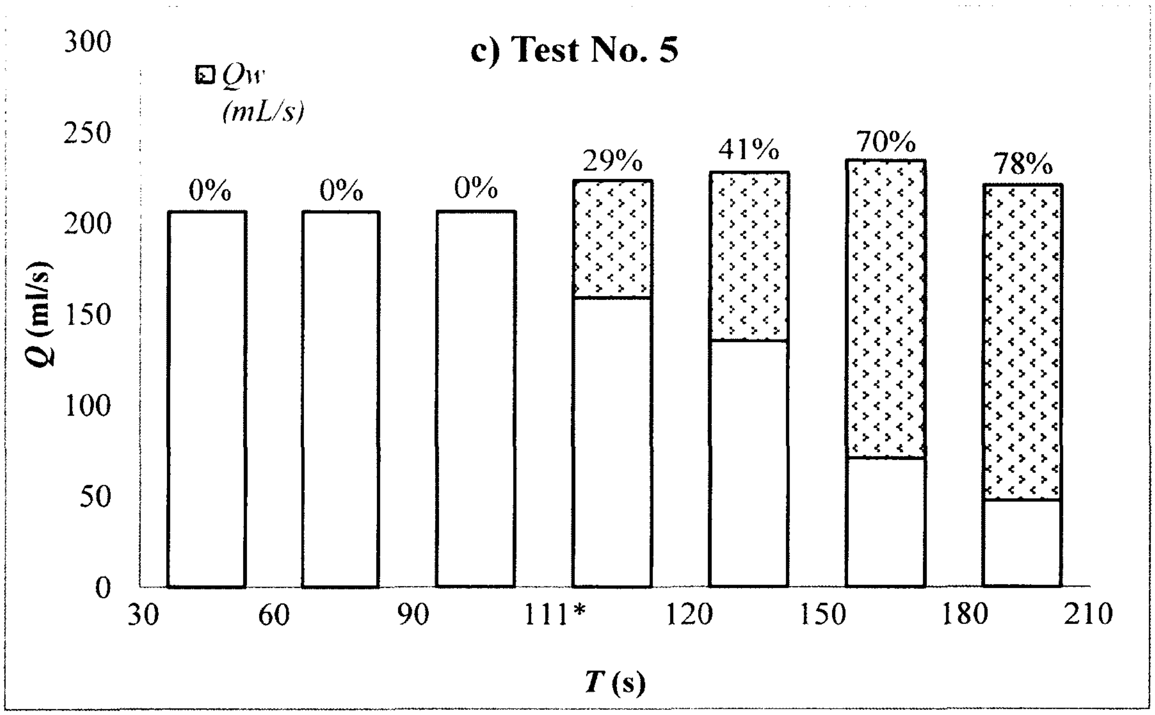

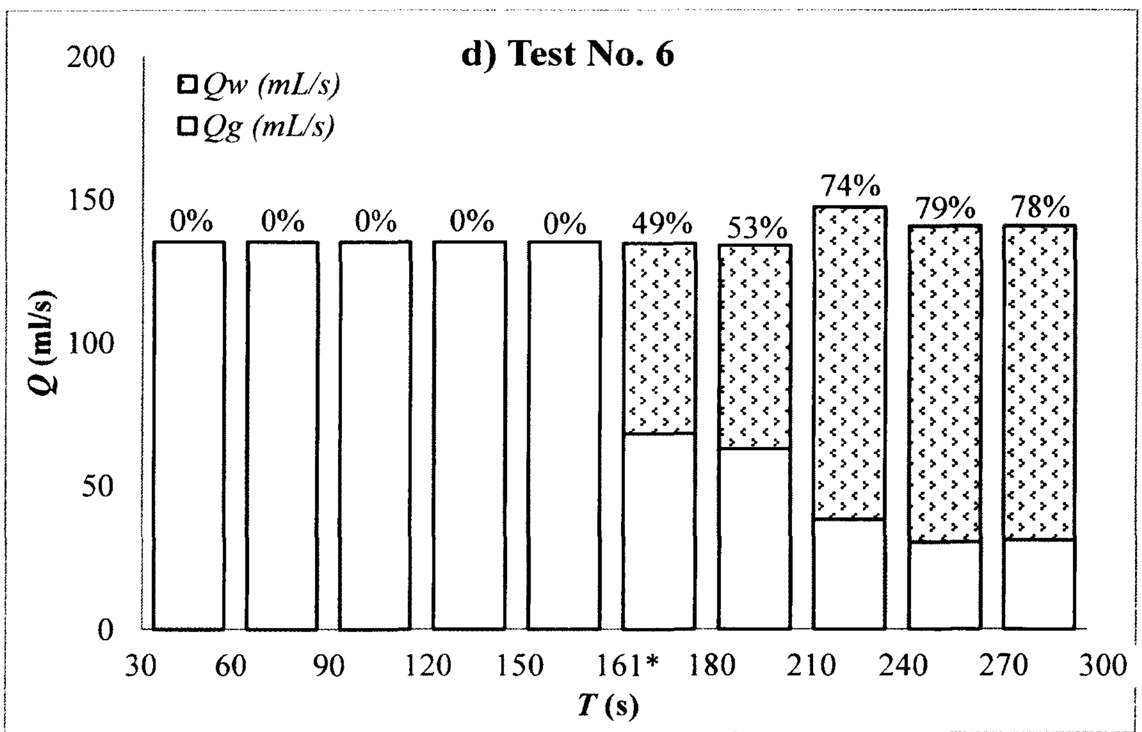

Figure 5-4 The estimated discharges of water and gel during pumping process in test No. 2, 3, 5 and 6. The blank blocks represent gel flow rate and the filled ones are for water. Labels are the percentage of water discharge. The superscript * indicates the critical stage.

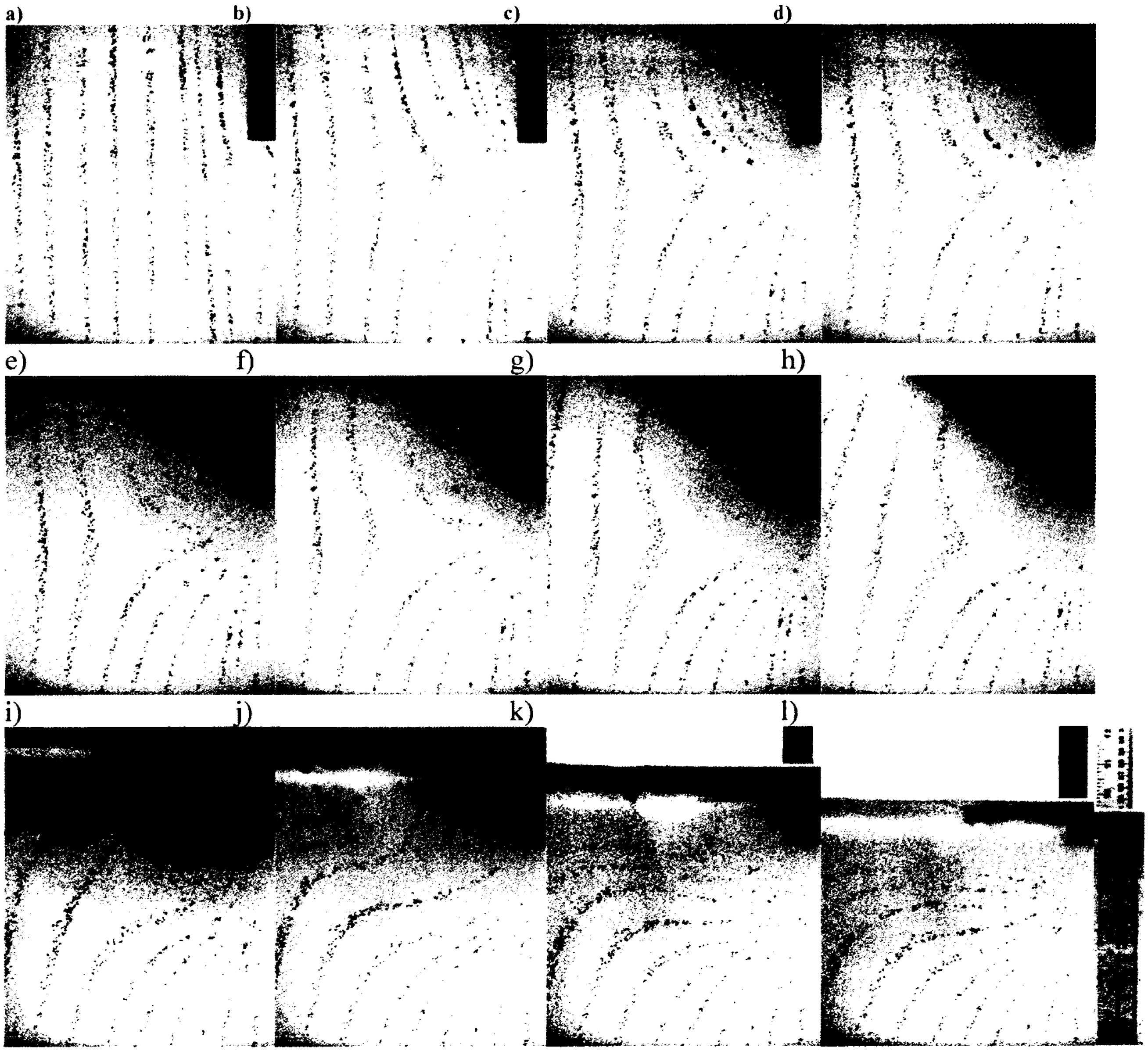

Figure 5-5 Raw images taken at a) 0.1 s, b) 40, c) 80 s, d) 90 s, e) 120 s, f) 160 s, g) 200 s, h) 240 s, i) 280 s, j) 320 s, k) 360 s and l) 400 s for test No. 10. A ruler is attached to show the scale of these images.

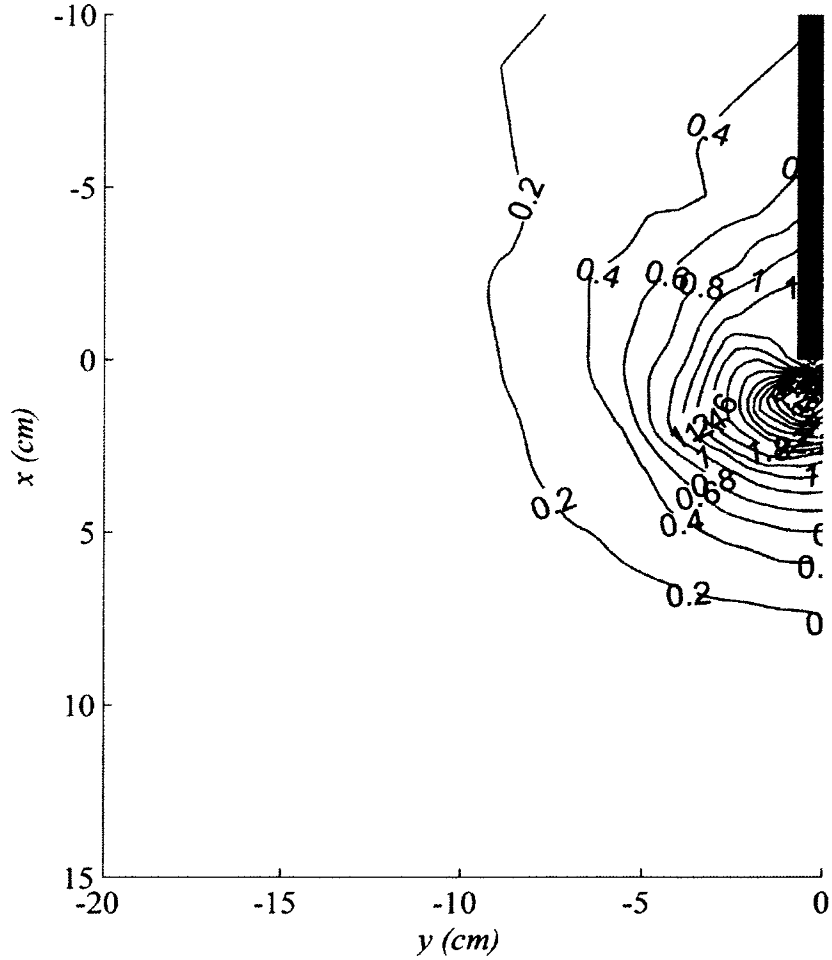

Figure 5-6 The velocity contour plot of test No. 7 (in the unit of cm/s).

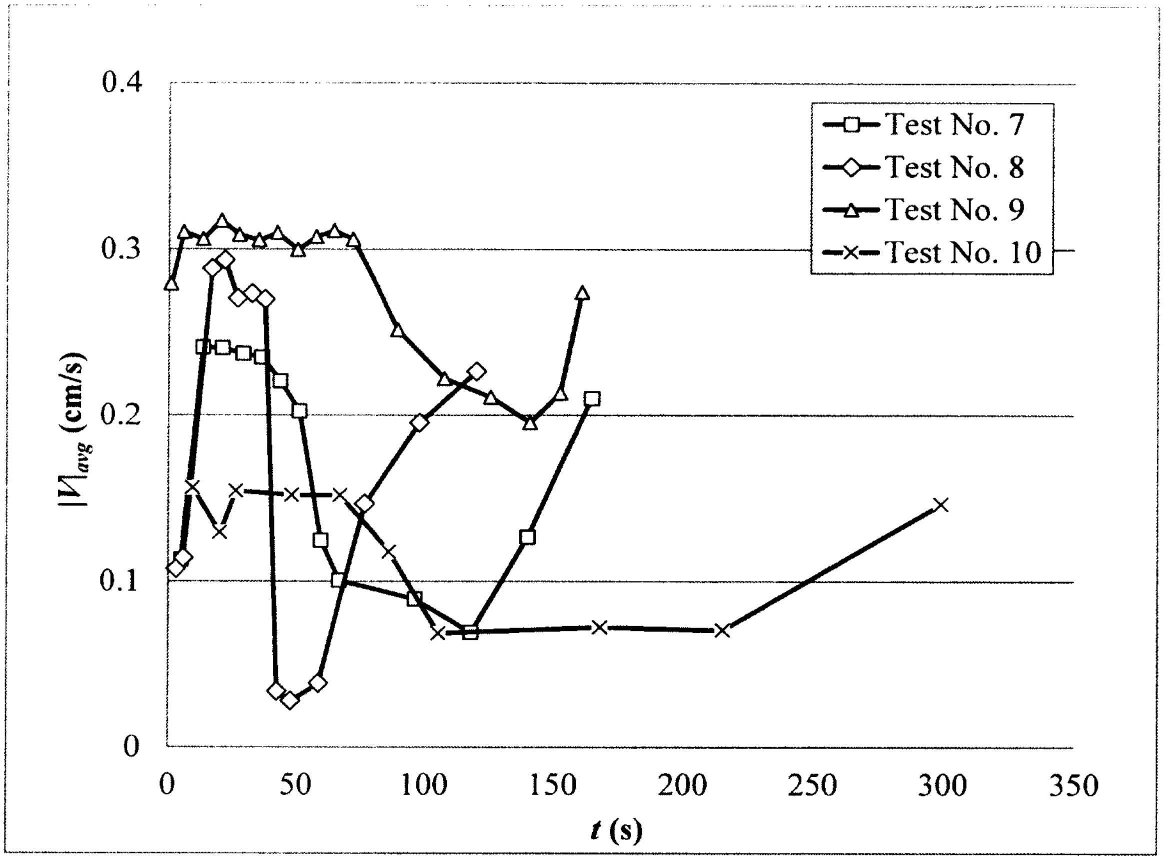

Figure 5-7 Variation of field averaged velocity of gel with time. The area used for calculation is the seeded area as shown in Figure 5-5. Two zones were blocked out: the area covered by the intake pipe and the area covered by water.

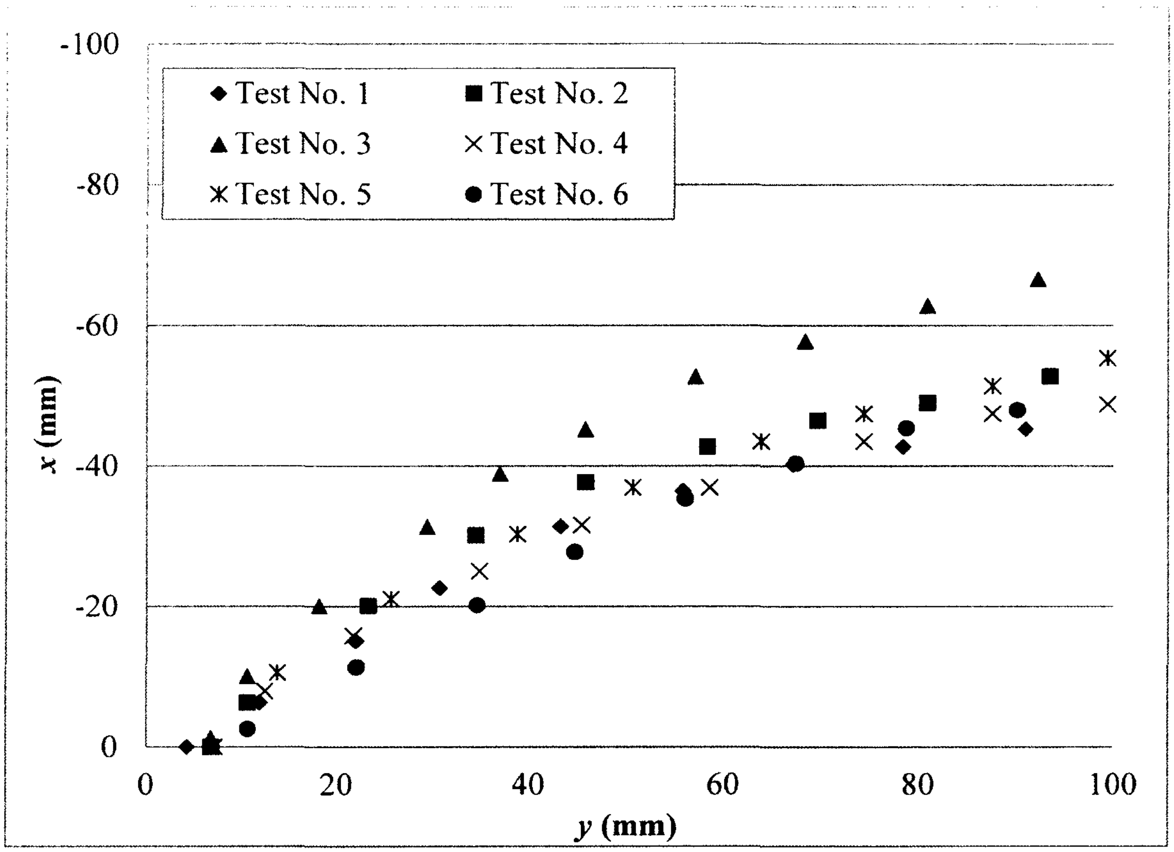

Figure 5-8 The drawdown curves of test No. 1 ~ 6 at the critical stage.

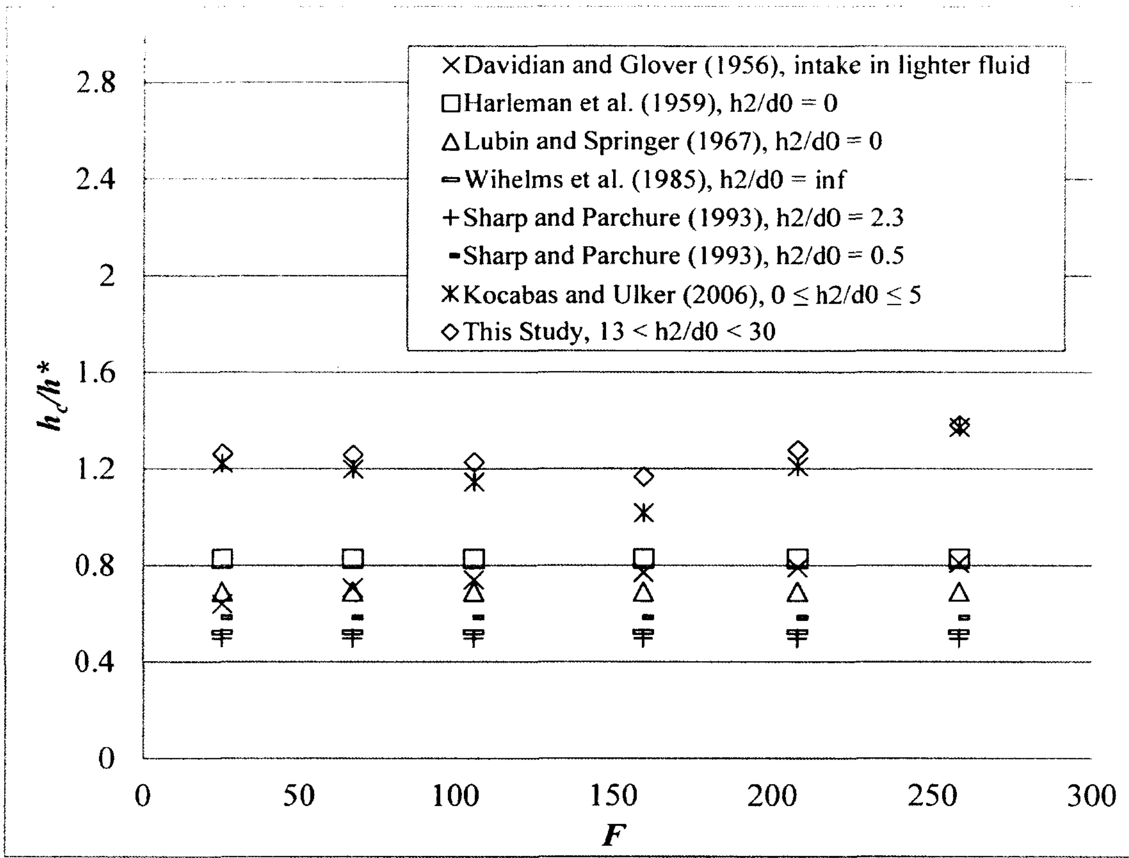

Figure 5-9 The dimensionless critical submergence is not dependent on the Froude number at the intake.

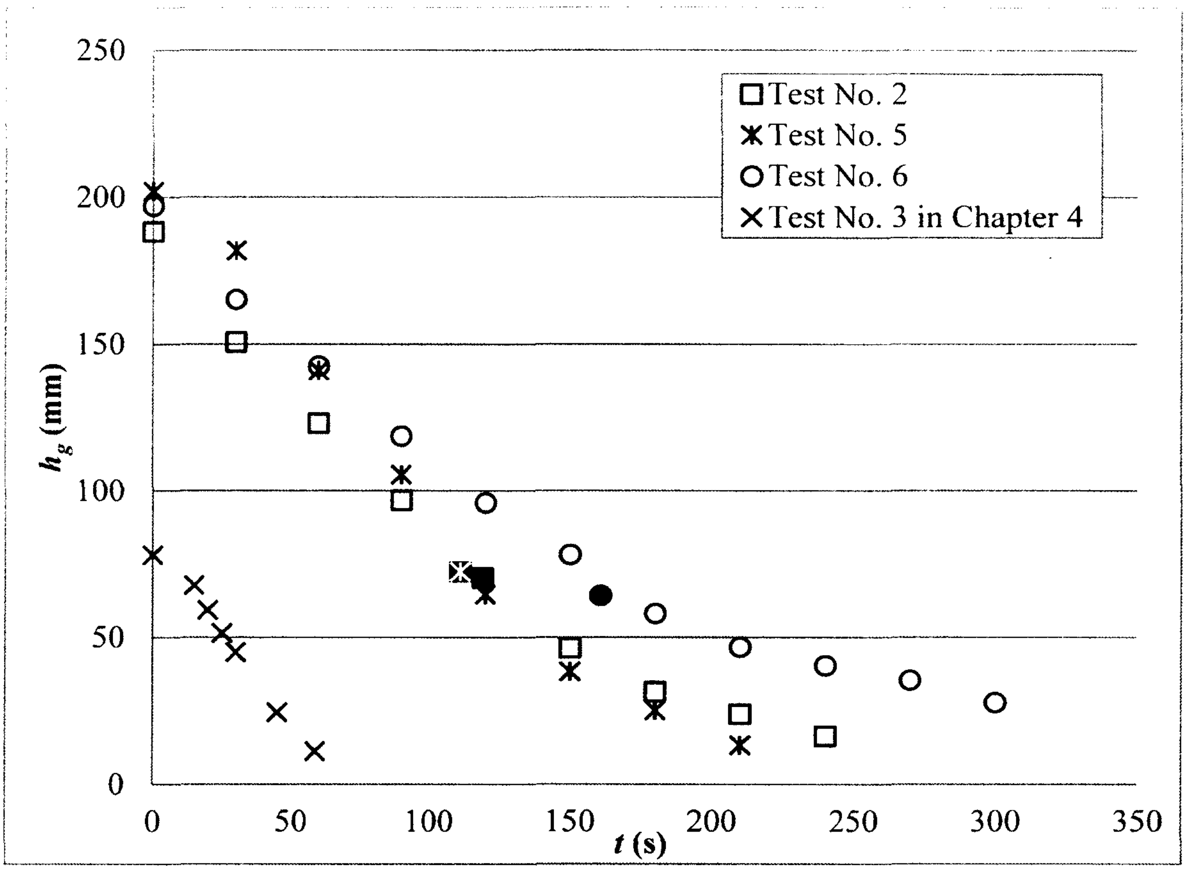

Figure 5-10 The depth of gel above the interface of gel and water varies with time. The filled symbols are used to indicate the critical stages of each test. The decreasing rate of this depth in subcritical stage is proportional to the pumping flow rate.

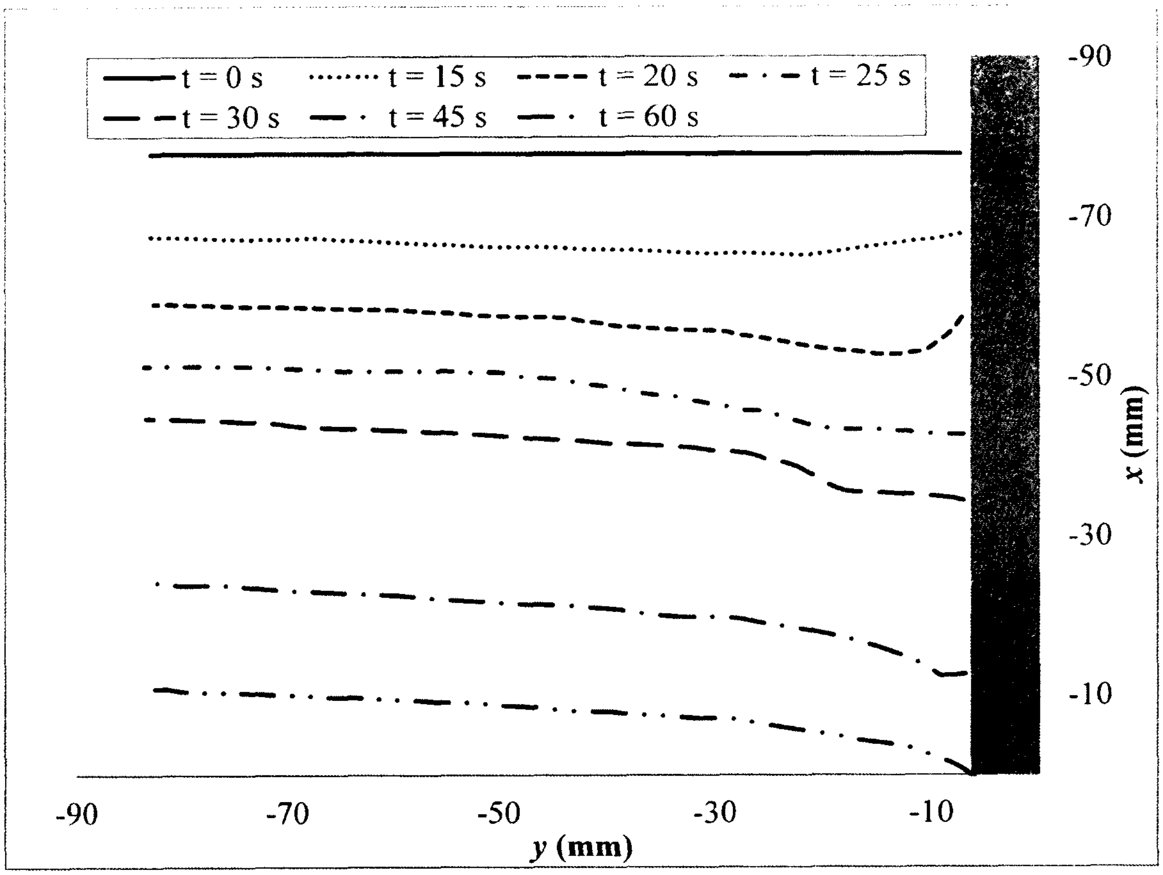

Figure 5-11 The profiles of the surface of gel at different time during withdrawal process in the test No. 3 of pumping single layer of gel.

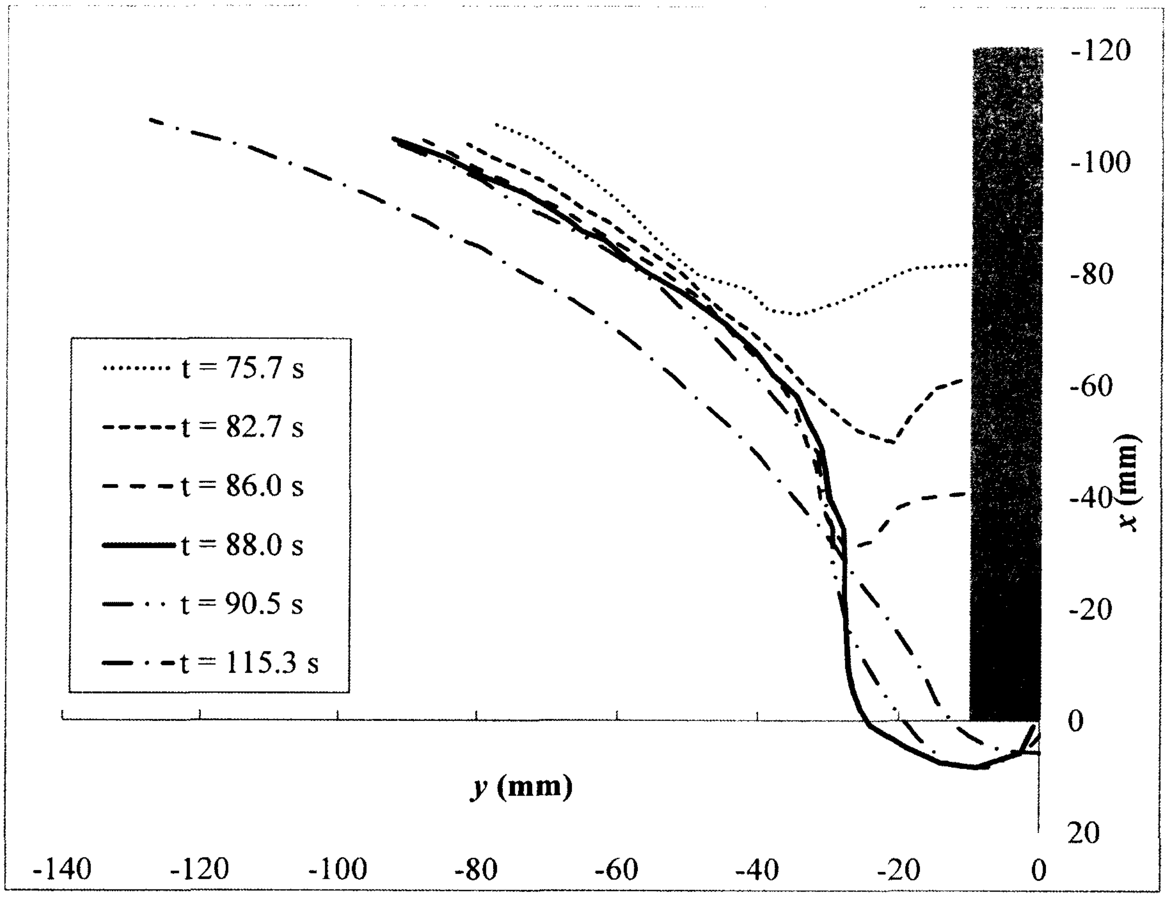

Figure 5-12 Development of the interface of water and gel during pumping in test No. 10.

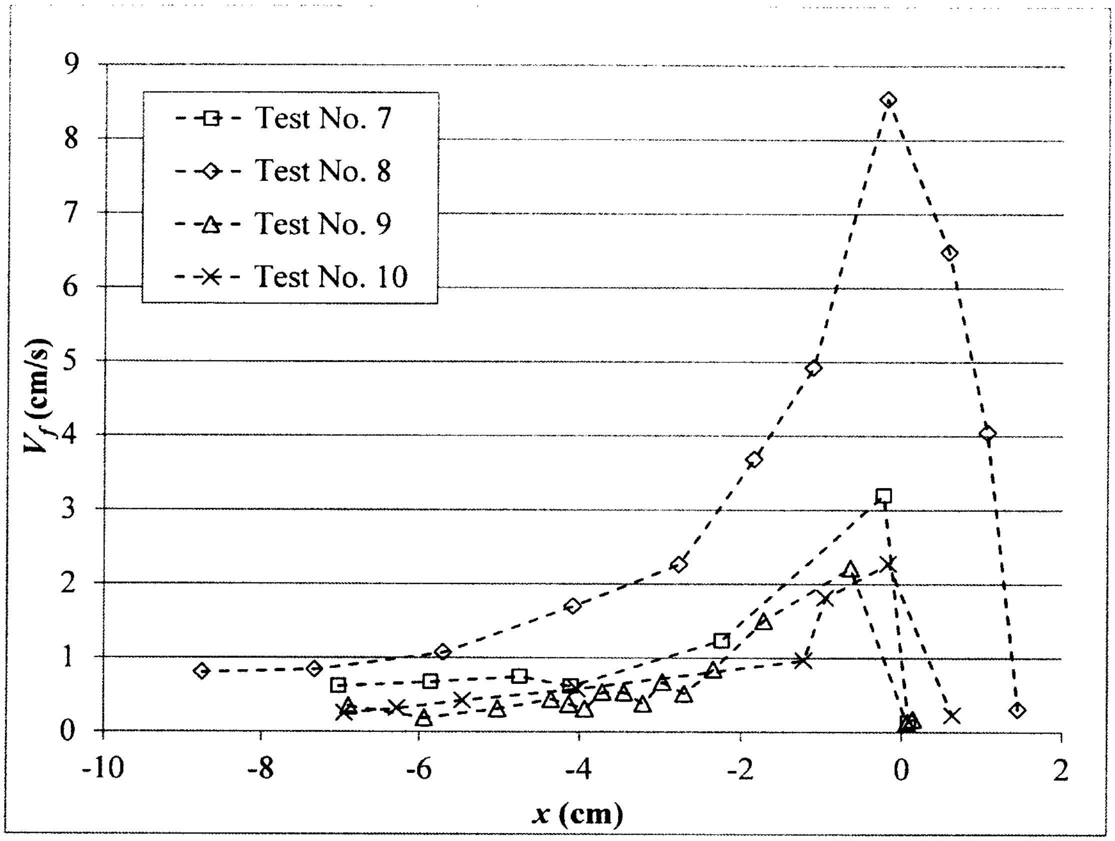

Figure 5-13 The vertical frontal velocity of water while travelling down in gel.

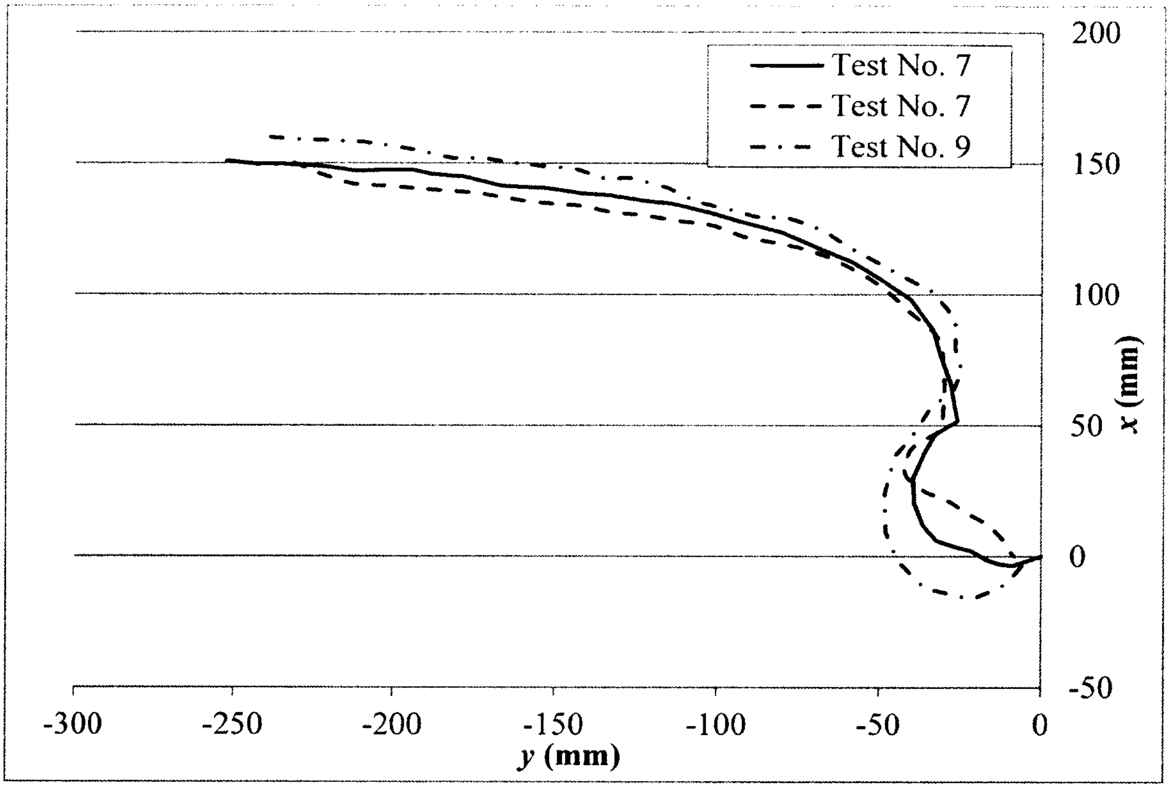

Figure 5-14 The interface profiles of water and gel at the critical stage in repeated test No. 7 and No. 9.

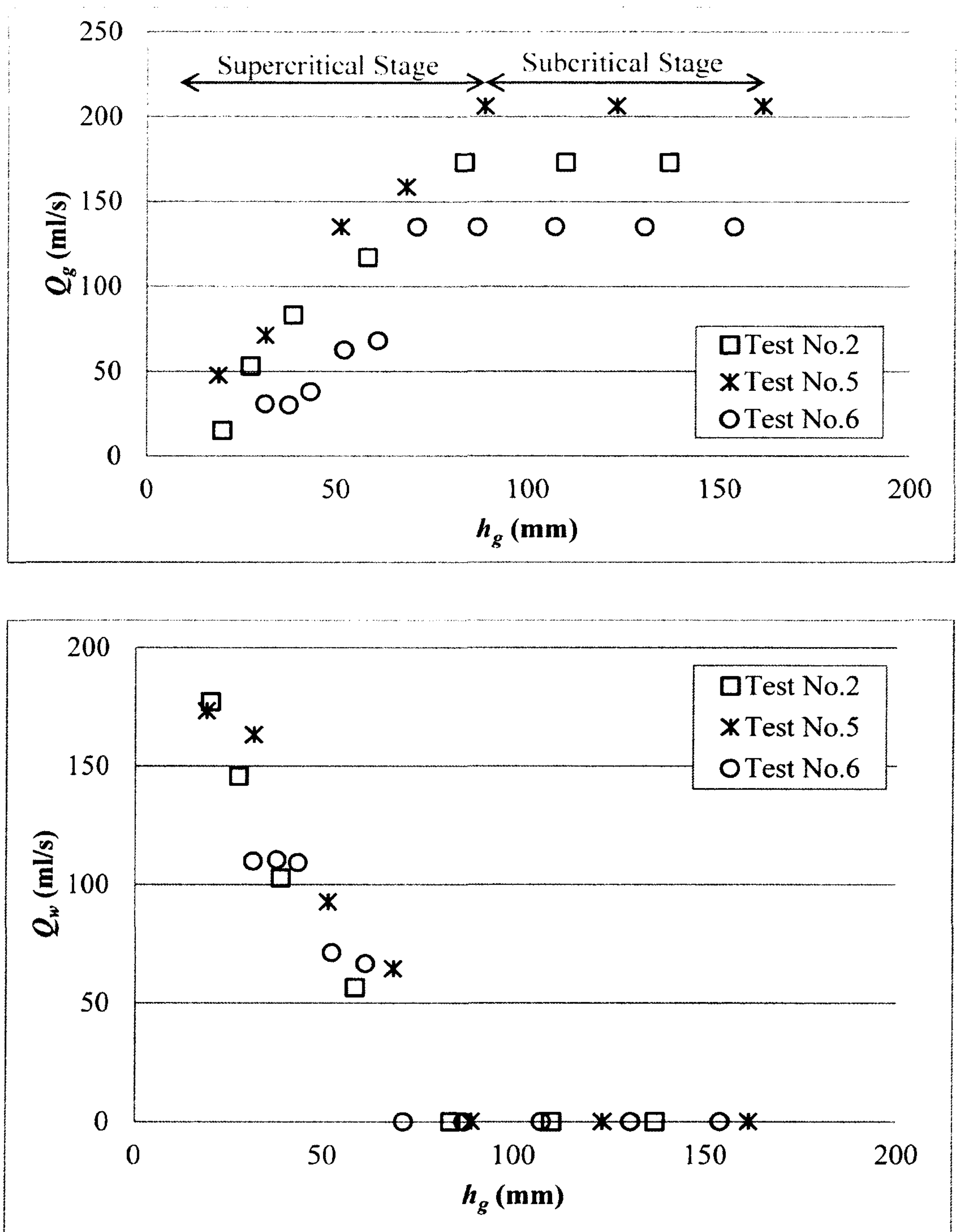

Figure 5-15 The discharges of gel and water change with the depth of gel above the interface.

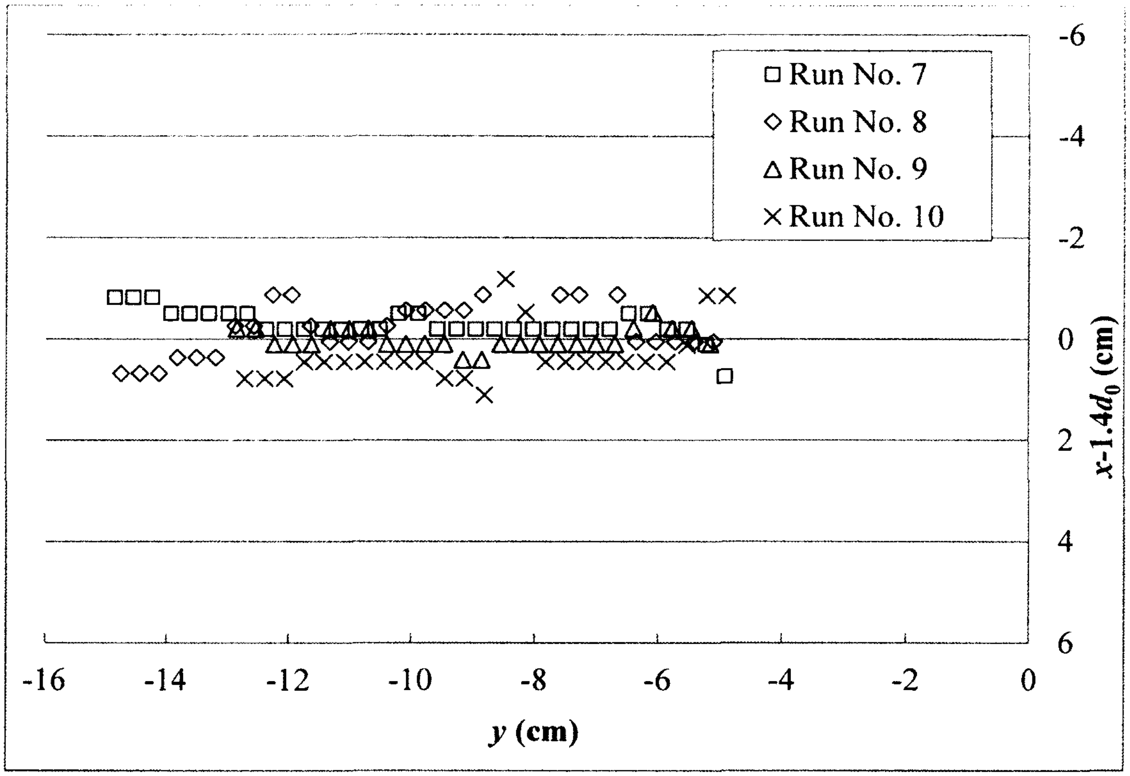

Figure 5-16 The locations of maximum horizontal velocity components.

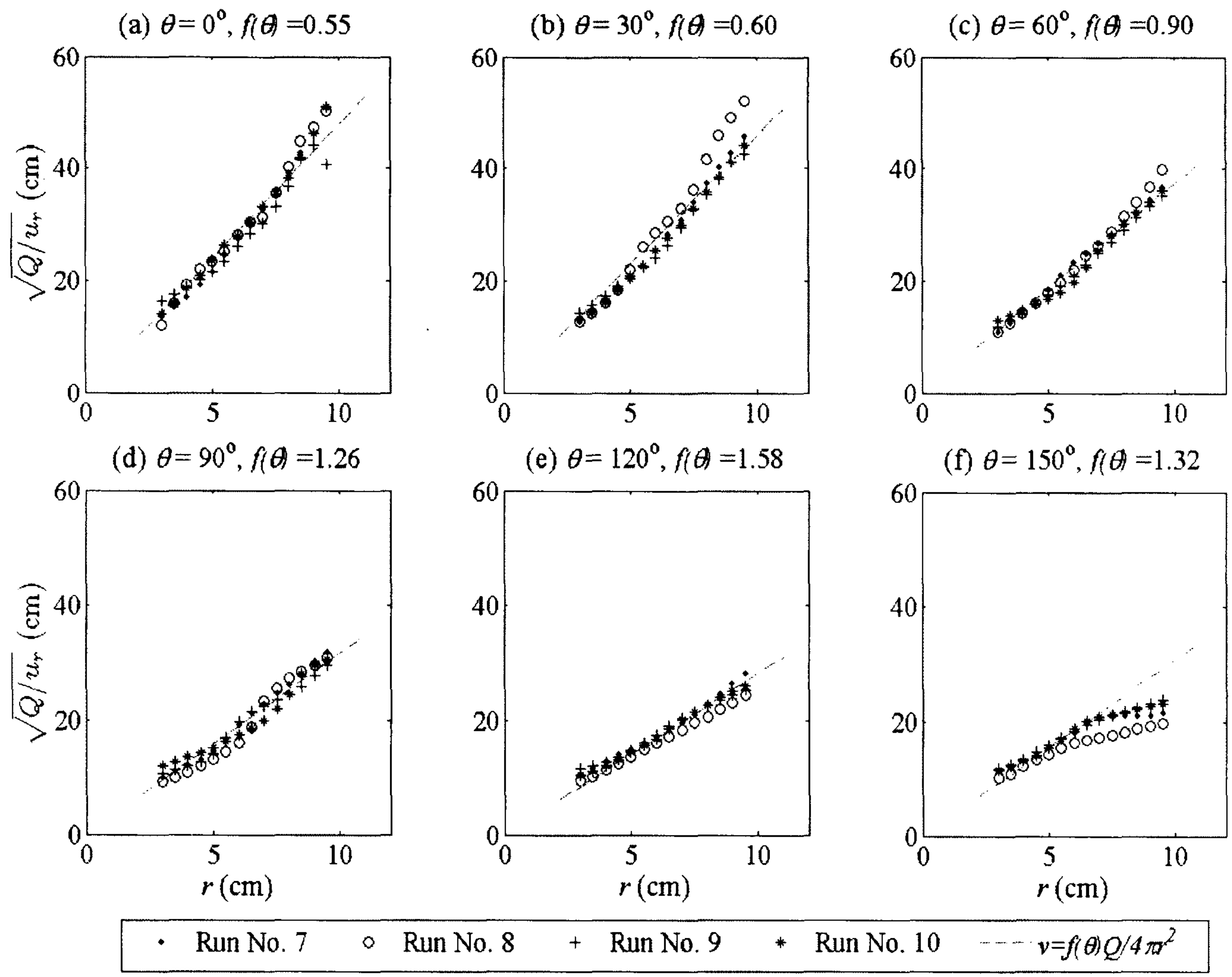

Figure 5-17 Radial velocity at different angles.

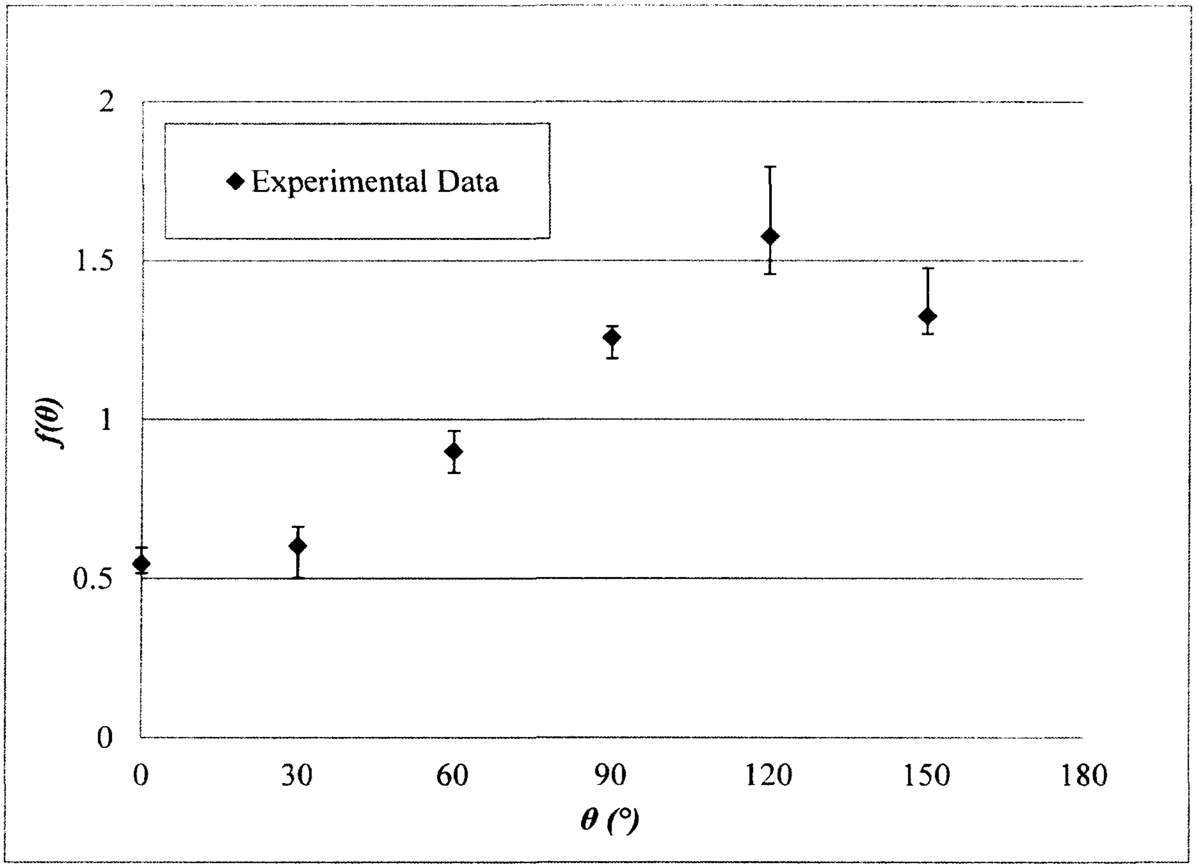

Figure 5-18 Variation of $f(\theta)$ with θ.

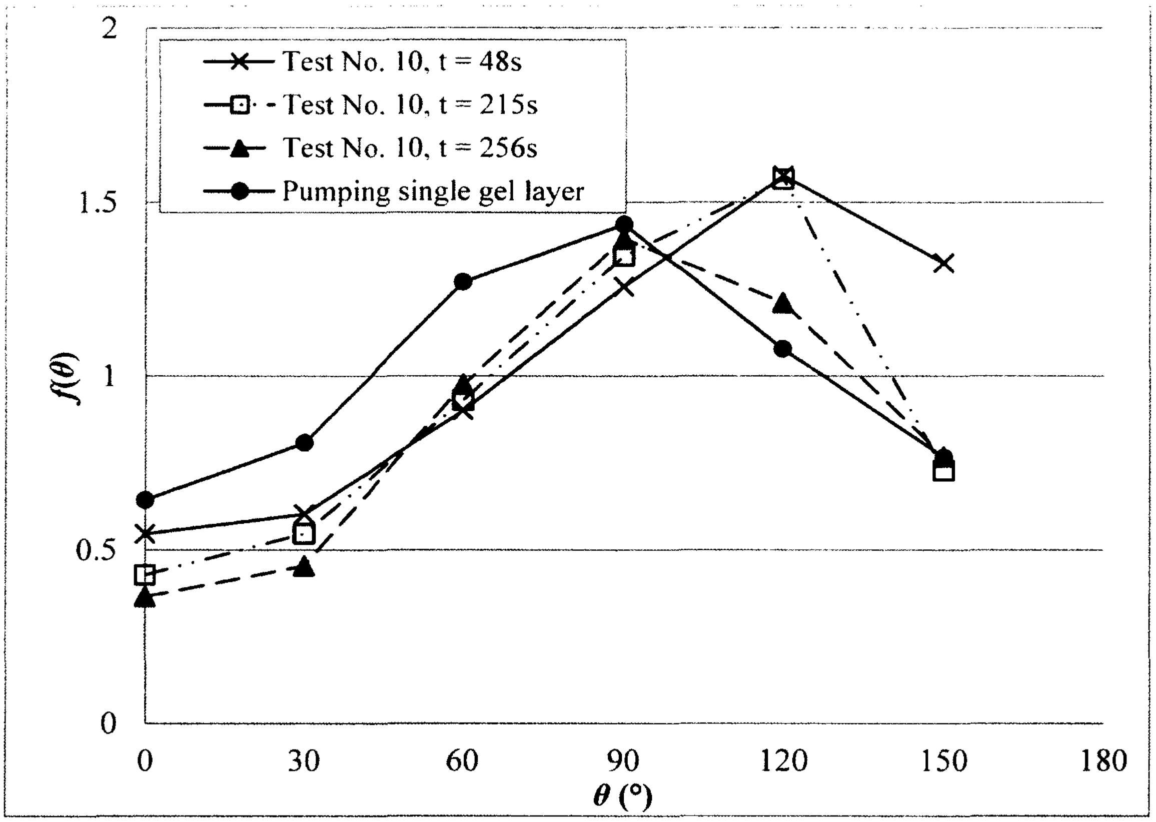

Figure 5-19 The values of $f(\theta)$ change with the experimental process in test No. 10. Three stages presented here are: a) stable stage of withdrawing gel only; b) withdrawal of both gel and water; c) withdrawal of gel again after water has been all taken out by pump. All are compared with the result in chapter 4 for pumping from single gel layer.

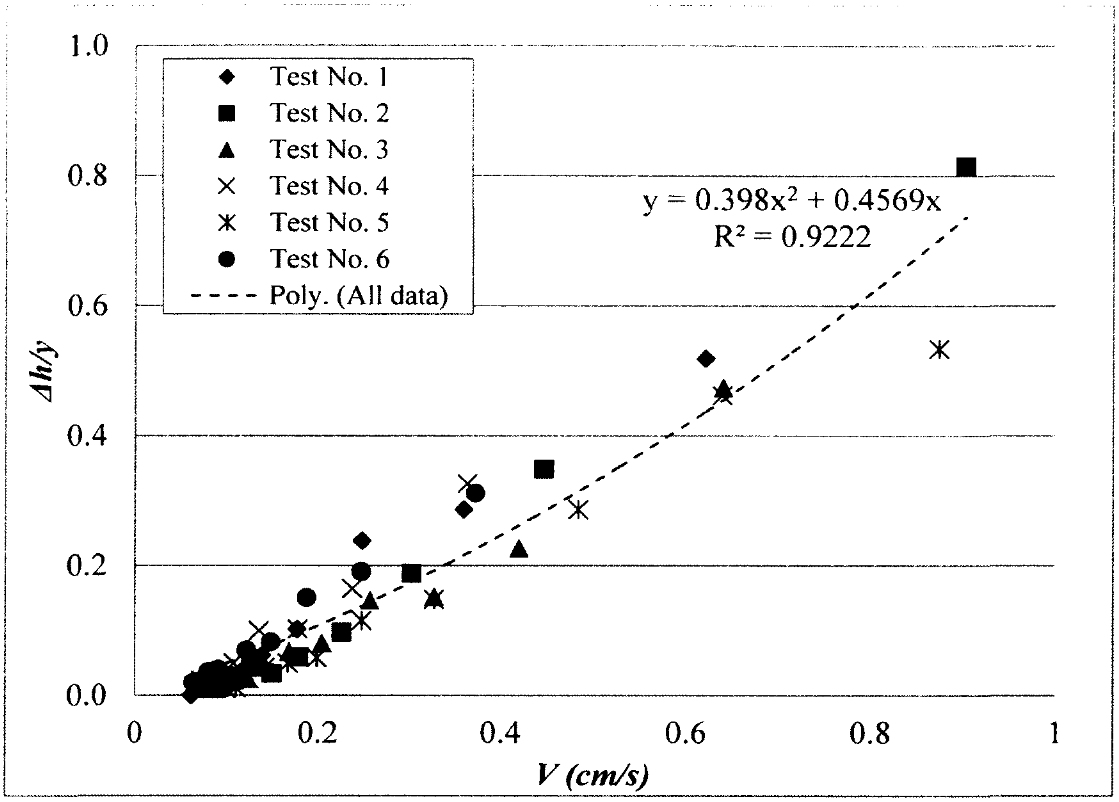

Figure 5-20 The relationship of average velocity and the hydraulic gradient.

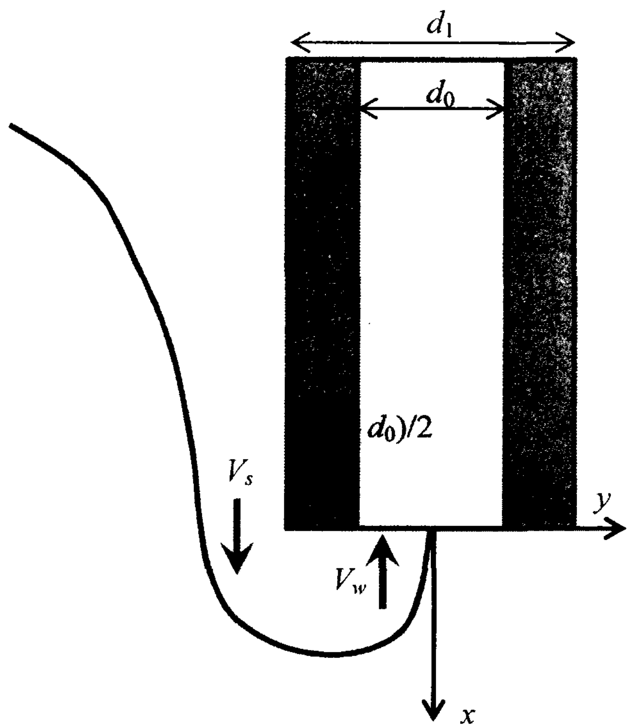

Figure 5-21 The sketch of the water scouring in gel.

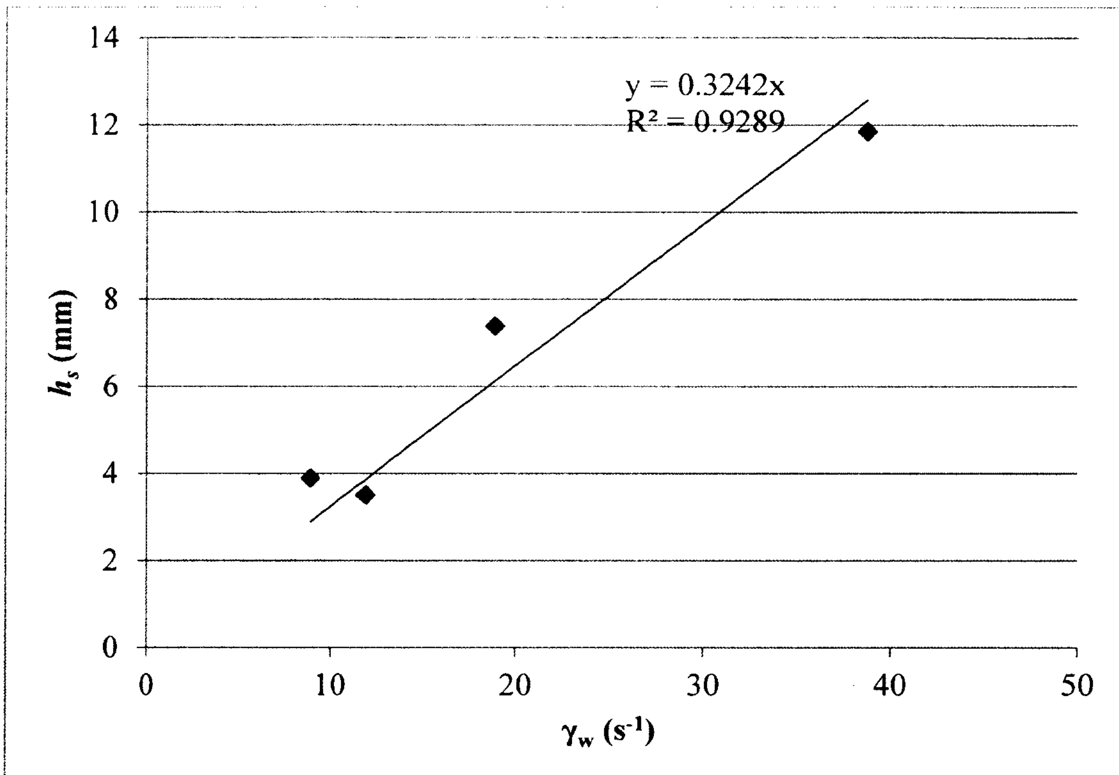

Figure 5-22 The erosion depth of water in gel increases linearly with the shear stress/rate of water.

5.6 References

Alberta Government. "Alberta's Oil Sands." http://www.oilsands.alberta.ca/tailings.html.

Bear, J. (2007). *Hydraulics of groundwater.* Dover Publications, Mineola, N.Y.

Chhabra, R. P. (2007). *Bubbles, drops, and particles in non-Newtonian fluids.* CRC Taylor & Francis, Boca Raton, FL.

Craya, A. (1949). "Theoretical research on the flow of nonhomogeneous fluids." *La Houille Blanche,* 4 44-55.

Davidian, J., and Glover, J. E. (1956). "Development of the non-circulatory waterspout." *Proc Am Soc Civ Eng,* (HY 4), 1038.

Gariel, P. (1949). "Experimental research on the flow of nonhomogeneous fluids." *La Houille Blanche,* 4 56-65.

Hanks, R. W. (1963). "The laminar-turbulent transition for fluids with a yield stress." *AICHE J.,* 9(3), 306-309.

Harleman, D. R. F., Morgan, R. L., and Purple, R. A. (1959). "Selective withdrawal from a vertically stratified fluid." *Proc.Int.Assoc.Hyd.Res., 8th Congress, Montreal,* .

Kocabaş, F., Kişi, Ö., and Ardiçlioğlu, M. (2009). "An artificial neural network model for the prediction of critical submergence for intake in a stratified fluid medium." *Civ.Eng.Environ.Syst.,* 26(4), 367-375.

Kocabaş, F., and Ülker, S. (2006). "Estimation of critical submergence for an intake in a stratified fluid media by neuro-fuzzy approach." *Environmental Fluid Mechanics*, 6(5), 489-500.

Lawrence, G. A., and Imberger, J. (1979). "Selective withdrawal through a point sink in a continuously stratified fluid with a pycnocline." *Tech.Rep ED-79-002*, .

Lubin, B. T., and Springer, G. S. (1967). "The formation of a dip on the surface of a liquid draining from a tank." *J.Fluid Mech.*, 29(PART 2), 385-390.

Marino, M. A., and Luthin, J. N. (1982). *Seepage and groundwater*. Elsevier Scientific Pub. Co, Amsterdam; New York.

Sharp, J. J., Parchure, T. M., and Guo, Z. R. (1996). "Selective withdrawal through an intake fitted with a collar." *J.Hydraul.Eng.*, 122(12), 683-691.

Sharp, J. J., and Parchure, T. M. (1993). "Selective withdrawal using circular partly submerged intake structures." *J.Hydraul.Eng.*, 119(5), 615-627.

Sharp, J. J., and Parchure, T. M. (1991). "Critical submergence in two-layer stratified flow." *J.Hydraul.Eng.*, 117(7), 924-928.

Wilhelms, S. C., Holland, J. P., and Smith, D. R. (1985). "Advances in Selective Withdrawal Through a Point Sink." *21st IAHR Congress*, Melbourne, Australia, 281-286.

Zhou, D., and Feng, J. (2009). "Selective withdrawal of non-Newtonian fluids: surface deformation induced by a sink flow." *Bulletin of the American Physical Society 62nd Annual Meeting of the APS Division of Fluid Dynamics*, .

Zhou, D., and Feng, J. J. (2010). "Selective withdrawal of polymer solutions: Experiments." *J.Non Newtonian Fluid Mech.*, 165(15-16), 829-838.

Chapter 6 Conclusions and Future Studies

This chapter is a summary of the previous chapters and will discuss some recommendations for future research.

6.1 Conclusions

This thesis presents the laboratory studies on sand jets in air and in viscoplastic fluids, as well as the pumping tests on non-Newtonian gels with or without water capping. It presents a lot of interesting experiments and innovations of experimental methods.

In chapter 2, a series of experiments on free falling circular sand jets in air was conducted. Three nozzles sizes, 19.2 mm, 31.1 mm and 63.8 mm were used and sands with various particle sizes, median size of 0.21 mm, 0.38 mm and 0.52 mm, were tested. It was found that:

- The frontal speed of sand jets travelling in air increases with the distance of the front L with negligible air resistance, so it only depends on the acceleration purely due to gravity.
- The variation of the sand jet frontal velocity is independent of the dimension of the nozzle and the size of the sand particles.

- However, the nozzle and particle size ratio is too small (~ 10 or less). the jet would spread out in air, thus the frontal velocity could be different.
- The steady velocities of these sand jets increase while sand concentration decreases when they travel vertically downwards from the nozzle. Their diameters become smaller until approaching an asymptotic value at the location about 120 times the nozzle sizes from the initial uniform section.
- Waves along the jets travel as the same speeds as the jets themselves while the wavelengths are varying at different distances.

In Chapter 3, by changing the size and height of sand jets, experiments were conducted to deposit different sand jets vertically into non-Newtonian viscoplastic fluid. The result shows that:

- The deformation of sand jets in the receiving fluids can be categorized into three types: dripping, jetting or mixing for different entry velocity and size.
- Dripping or a drop will form at the surface of the gel when the jet is small and the velocity is low; while for a big jet with high velocity, the sand jet will continue in the gel to form a confined jet; Furthermore, when the velocity is extremely high and the size of the jet is very big, it will become a dispersed jet with tremendous mixing.

- A conceptual parameter l_m can be used as an index to classify the behavior of sand jets in gel.
- The viscosity of the fluid is also an important factor, as drops are more likely to form in viscous fluid with higher yield stress.
- The frontal speed of the sand drops in the gel was proportional to the distance away from the gel surface.
- The yield-gravity parameter of the deformed drops was found to fall into two groups.

In Chapter 4, based on our laboratory study on pumping a Bingham plastic fluid, it was found that:

- When PCP is applied to lift a Bingham non-Newtonian fluid from a vertical circular pipe, the radial velocity of the fluid towards the intake keeps the same within a conical zone, which is $\leq 15°$ below the intake entrance.
- In outer region, the horizontal velocity is symmetric to a horizontal line, which is $1.4d_0$ below the intake entrance level.
- Intake pipe size has no impact on the velocity field, when it can be simplified as a point sink.
- An analytical method can be used to describe the velocity field of the sheared fluid when it approaches a steady state while pumping, with

assumptions of axisymmetric flow and zero tangential velocity in a spherical coordinate system.

- The deformed area when pumping viscoplastic fluid is proportional to the 1/3 power of the pumping flow rate.

In Chapter 5, withdrawal tests were set up to pump a two-layer Newtonian and non-Newtonian liquid system. The velocity field of the lower layer gel and the interface deformation of two fluids were studied. Summaries include that:

- At the subcritical stage, the pumping discharge is stable once the yield stress of the gel was overcome; but at the supercritical stage, total discharge increases first then decreases when water discharge grows and the mixed fluids decrease in viscosity.
- The deformation rate of the water-gel interface and the critical submergence of the pump intake to prevent water leaking are proportional to the pumping flow rate flow rate but not sensitive to variable intake sizes.
- The critical submergence is proportional to the flow rate to the power of 2/5.
- The non-dimensionalized critical submergence is at least 1.5 times higher than that of two-layer Newtonian flows when withdrawing from the lower or the heavier layer.

- Under the same assumptions as what are in chapter 4, the radial velocity varies at different angels and its variation is independent of the intake size.

6.2 Recommendations

As an extension of the study presented herein, future work is suggested to test more conditions of pumping water-gel system. The parameters that can be varied in each experiment include: the structure of the intake (e.g. with a cap); the water-capping depth; the rheology of the gel and the pumping rate. The measurements include the interface deformations, flow discharges and fluid velocity fields.

Furthermore, to simulate the real case in the field, real MFT is also recommended to use with the same setup in the lab. However, due to the opacity of MFT, some new technologies, such as light scattering technology or other optical instruments are proposed to be utilized in the test for detecting the MFT-water interface changing during pumping process.

The laboratory work is very time-consuming and the scale is limited by the container used in lab. For this reason, CFD modeling should be conducted to develop further understanding of the pumping process in the real cases. It can be calibrated with the experimental data with pumping real MFT or field data in the tailing ponds. In addition, to simulated the layered density and rheology condition of real MFT sitting in the tailings ponds, multilayer systems should be examined. Another important component that would be taken into account is the thixotropic behaviour of MFT.

There is not an explicit way to solve the fluid mechanical equations. To find a practical model or straightforward method to present the ideal pumping schemes, soft computing technologies can be applied. Artificial Neural Network (ANN) and a Fuzzy Logic models can be established and calibrated by CFD data and an empirical expression can be worked out for practical uses.

Appendix A Laponite Properties

Laponite is a synthetic clay which can be used as a rheology additive. Laponite particles are in disk geometry, with diameter around 25 nm and thickness of 1 nm. Its general formula is $Na^{+0.7}$ $[Si_8Mg_{5.5}Li_{0.3}H_4O_{24}]^{-0.7}$ with a particle density of 2.53 g/cm^3 (Paula *et al.* 2009). Figure A-1 shows a Laponite particle and its crystallographic structure. The schematic stages of addiction Laponite to water is presented in Figure A-2.

In order to simulate the rheological behaviour of MFT, the Laponite gels of 2.5% and 3.0% concentration in demineralised water are tested using Brookfield rotational viscometer DV-II+ (see Figure A-3) at the room temperature, giving different duration of dispersion time. The sets of vane spindles and disk spindles, as shown in Figure A-4, were applied to measure the yield stress and the viscosity respectively. Figure A-5 is an example of the measurement data for determining yield stress and all measurements for different samples. The peak value of the curve was obtained and used for the computation based on the size of the vane spindle applied. The method described by Mitschka (1982) is used to calculate the shear rate ($\dot{\gamma}$) - shear stress (τ) flow curves based on the rheological measurements, as shown in Figure A-6.

With different dispersion time, the rheology of the gel varied. However, Bingham plastic non-Newtonian model can be used to fit all obtained rheological data.

$$\tau = \tau_0 + \mu_p \dot{\gamma} \tag{A-6}$$

wherein τ_0 is the yield stress and μ_p is known as plastic viscosity. The best fitted parameters for different samples are presented in Table A-1. The value of μ_p decreases with the dispersion time intensively from 0.08 to 0.002 Pa·s and 0.03 to 0.001 Pa·s for 3.0% and 2.5% gels individually, as shown in Figure A-7. Being a pseudoplastic material, Laponite gel is a strongly shear-thinning fluid. As detected in our tests, it became more and more shear-thinning over the time, provided that the plastic viscosity became dozens of times smaller.

On the other hand, the change of the yield stress with time carries an opposite trend (see Figure A-5). During our observation period, τ_0 increased from almost 0 to 70.45 Pa for the 2.5% gel, and raised from 9.76 to 132.64 Pa for samples of 3.0%. Particularly, 2.5% Laponite behaves like a viscous Newtonian fluid at the second day after mixing, given its yield stress is close to zero and the shear rate – shear stress follows a linear relationship.

Table A-1 Rheological parameters for different Laponite samples based on the Bingham plastic model.

Time (h)	2.5% Laponite			3.0% Laponite		
	τ_0' *(Pa)*	τ_0 *(Pa)*	μ_p *(Pa·s)*	τ_0' *(Pa)*	τ_0 *(Pa)*	μ_p *(Pa·s)*
24	0.004821	0	0.0794	9.762287	10.391	0.0336
48	1.918891	3.3885	0.0583	12.72216	15.216	0.0182
72	9.820052	7.3635	0.023	33.92577	20.956	0.0116
96	16.65558	9.7849	0.017	39.22667	23.946	0.0107
120	21.49275	13.159	0.0094	47.99726	28.725	0.0053
144	27.46831	19.241	0.0021	48.67192	32.902	0.0013

a)

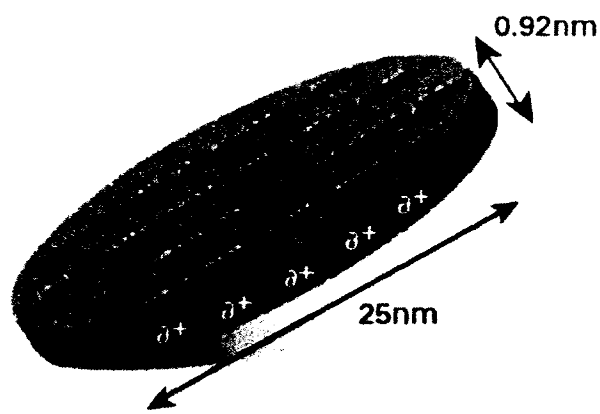

b)

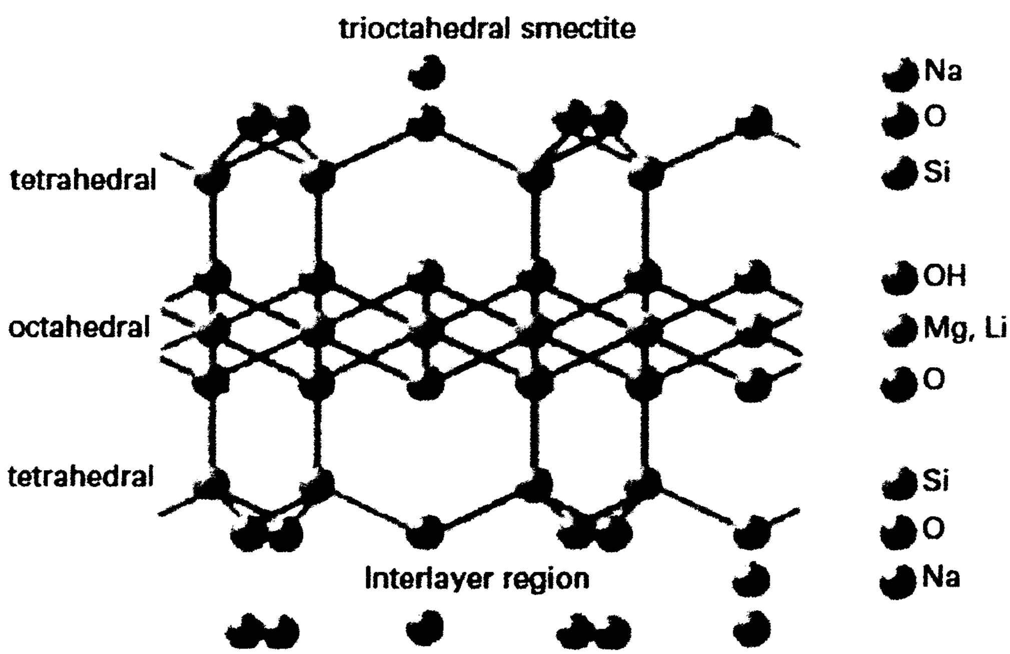

Figure A-1 a) Single Laponite Crystal; b) Idealised Structural Formula

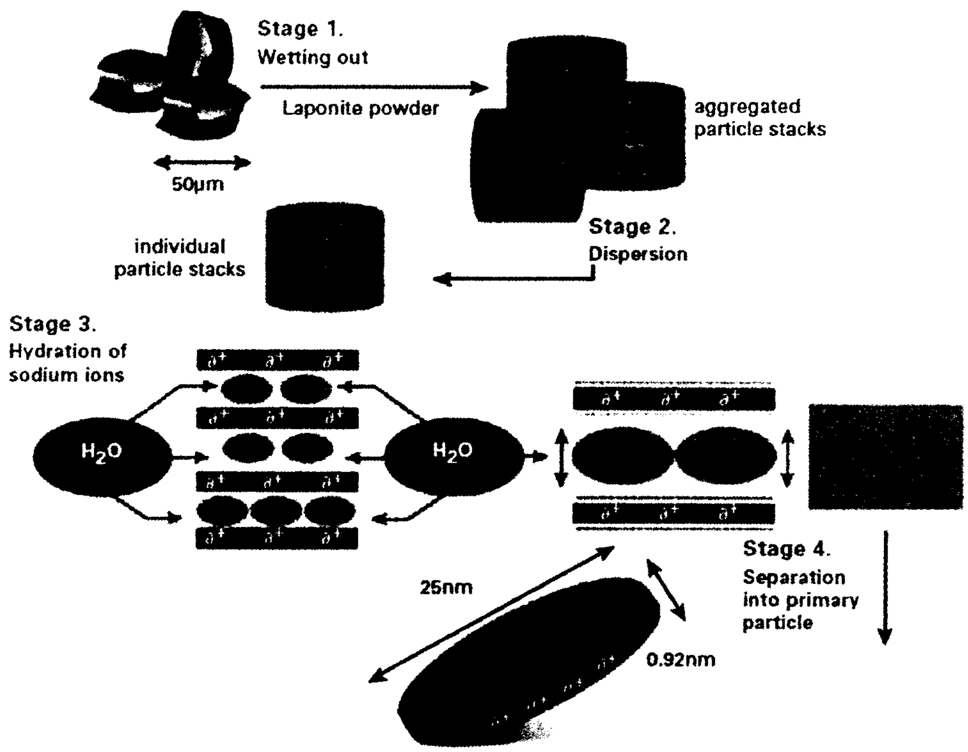

Figure A-2 Schematic stages of addiction Laponite to water

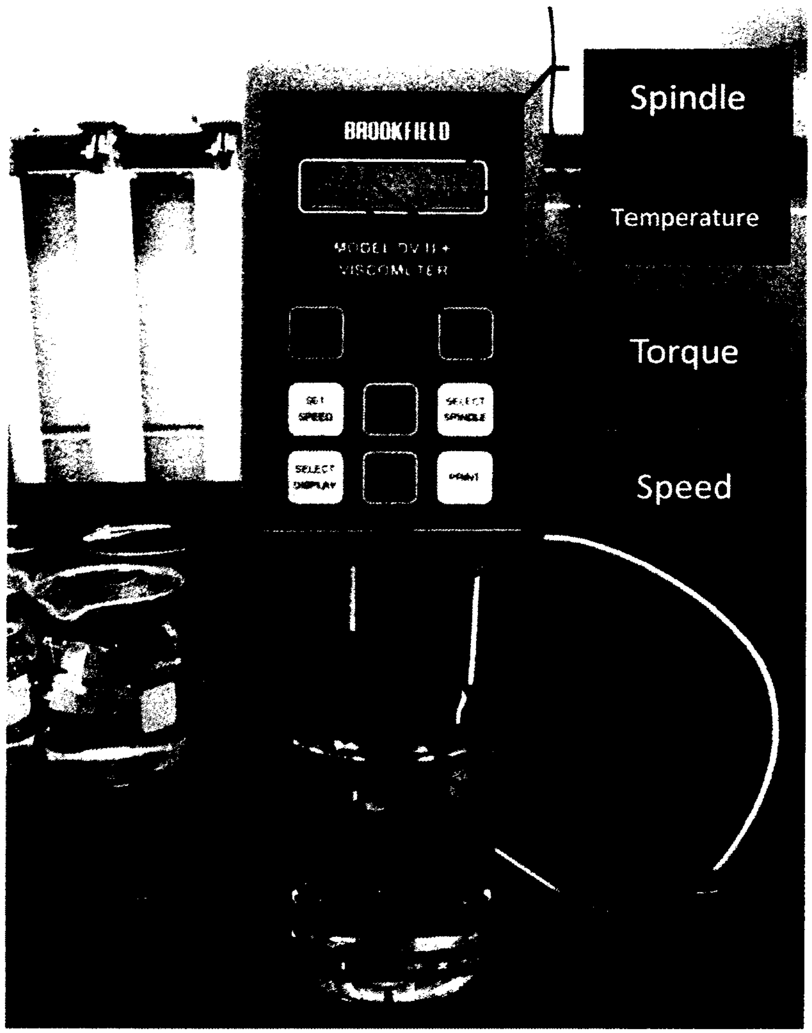

Figure A-3 Brookfield DV-II+ Programmable Viscometer.

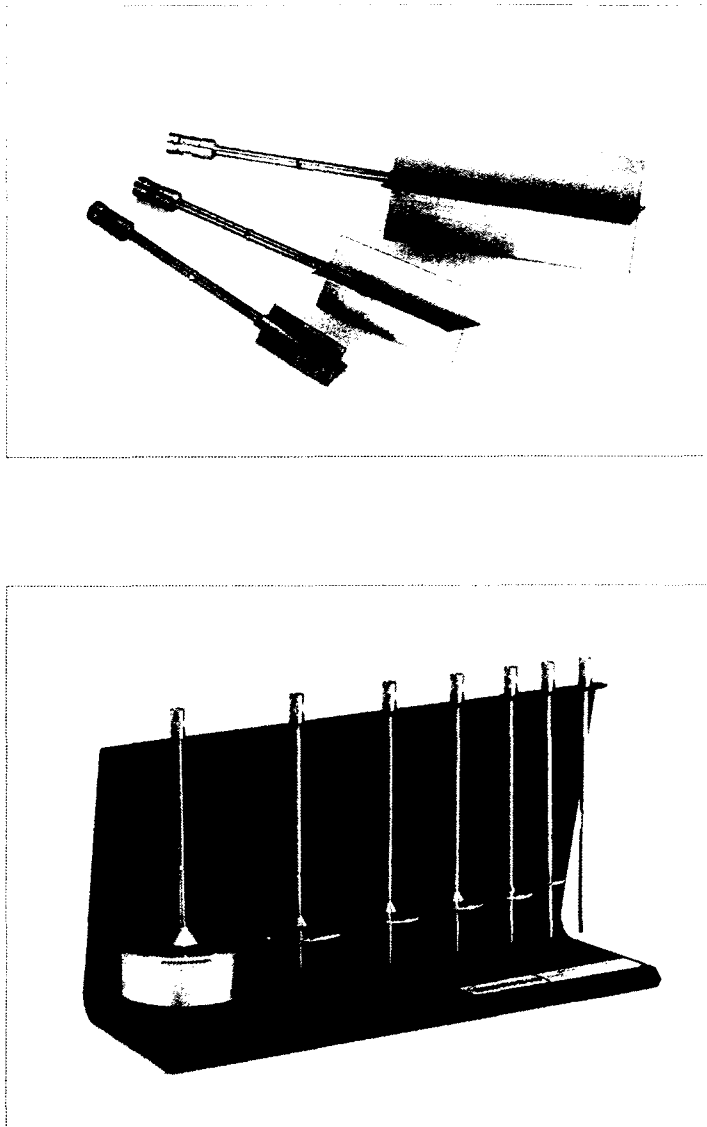

Figure A-4 The sets of vane spindles and disk spindles of Brookfield DV-II+ Viscometer.

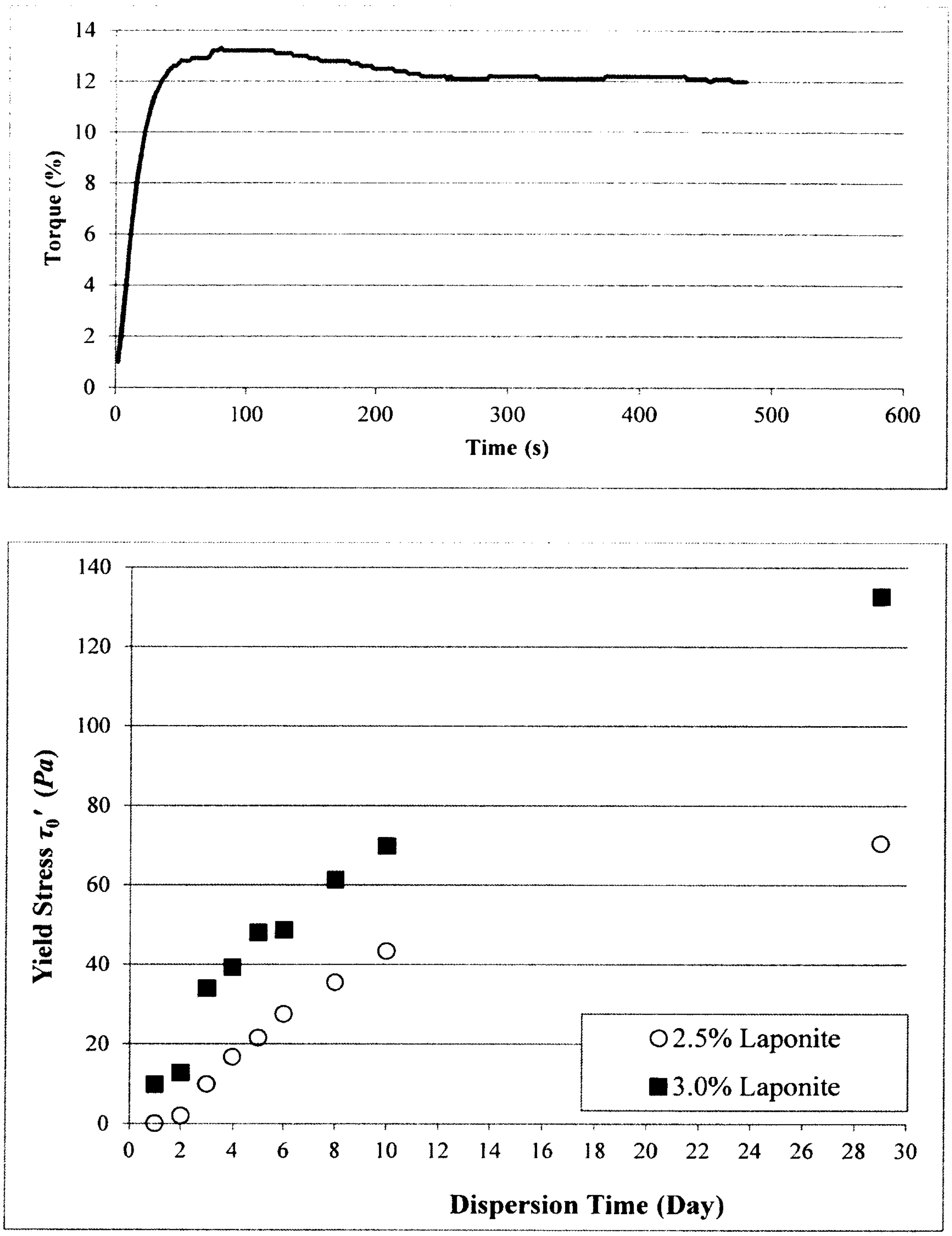

Figure A-5 a) A sample vane shear test measurement for 48 hours old 3.0% Laponite gel; b) The yield stress measurements of 2.5% and 3.0% Laponite gels.

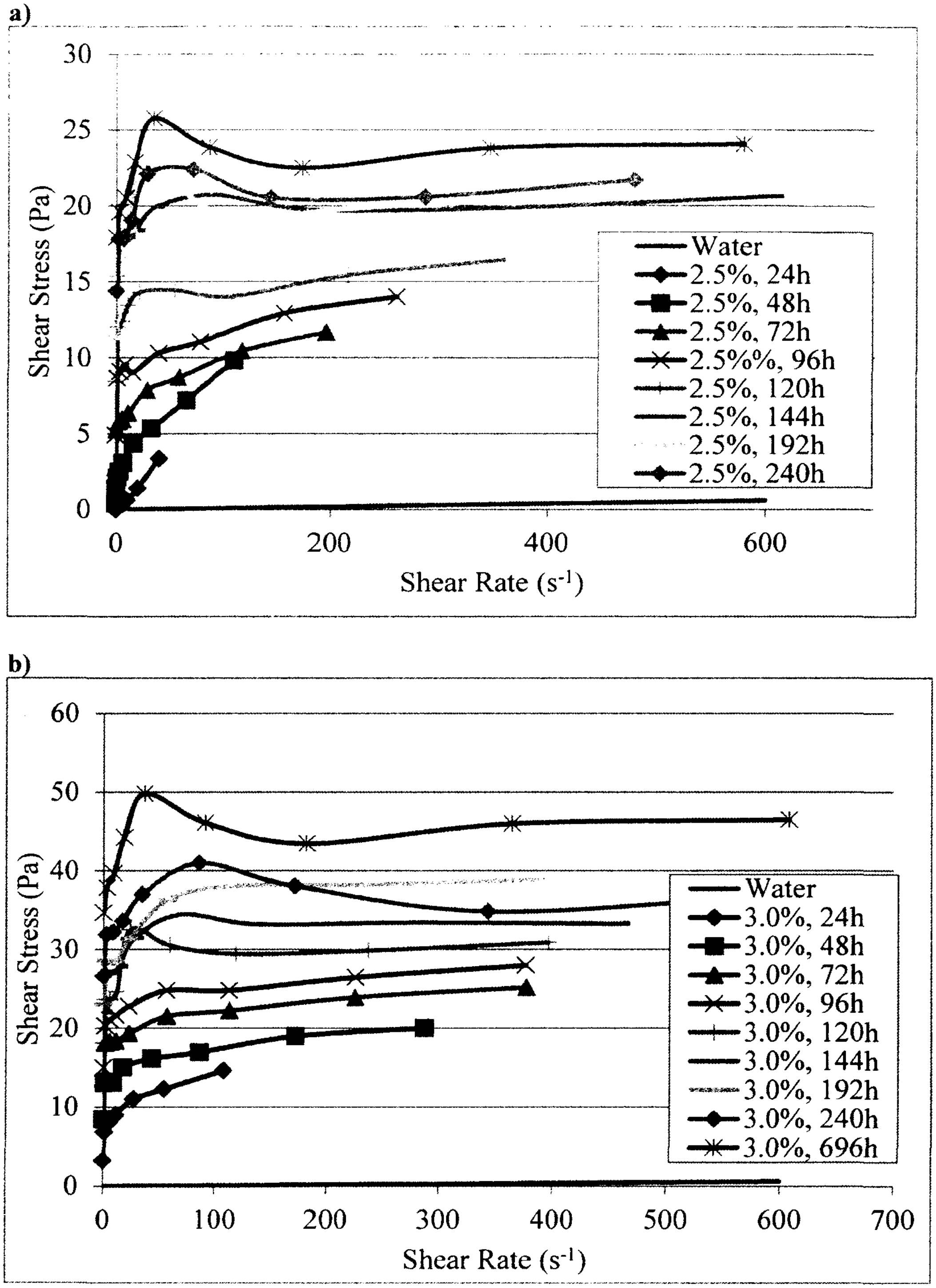

Figure. A-6 Laponite gel viscosity measurements: (a) 2.5% gel flow curve in different dispersion time; (b) 3.0% gel flow curve in different dispersion time.

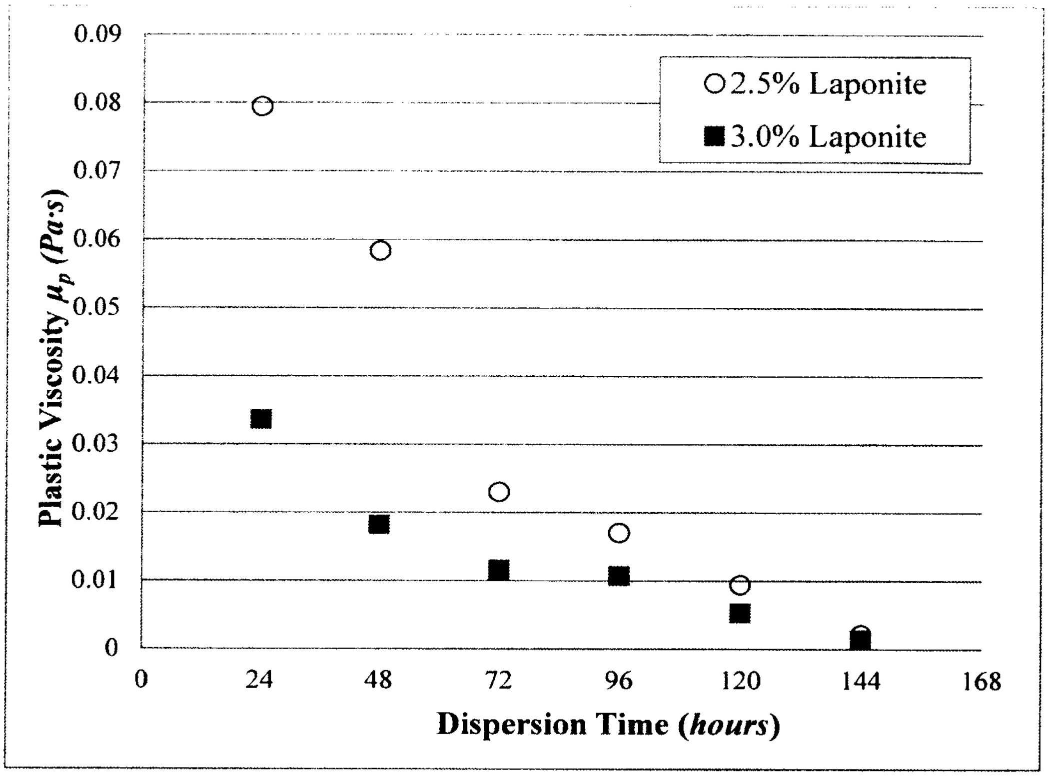

Figure A-7 2.5% and 3.0% Laponite gels become more and more shear thinning with time.

Appendix B PCP Efficiency

To calibrate the flow rate for pumping Laponite, different sizes of intake pipes were tested from the pumping rate from 100 to 1100 rpm. The results were presented in Figure B-1 along with the measurements of pumping water under the same conditions. In our test range, it is shown that PCP system is more efficient for pumping very viscous fluids compared with pumping water. When pumping gel, wider intake pipe has a bigger capacity for delivery under the same pumping rate.

When the rotor starts to run in a PCP, a cavity is created and the fluid in the intake or well is pushed by the pressure into the pump until the cavity closed (Zhou and Yuan 2008a). Ideally, the production of a PCP is proportional to the rotation rate of the pump rotor. However, the internal leakage, also called slip, from the outlet to the inlet is not negligible. The pump model, the clearance between rotor and stator, the fluid viscosity under the operation condition and differential pressure are all important factors affecting slip rate (Zhou and Yuan 2008b). In our study, the fluid viscosity is the only main factor to define slip because all experiments were conducted using the same pump.

For pipe flow, energy loss was mainly caused by friction. It was illustrated that the pressure loss for a power law fluid in a circular pipe $\Delta P \propto LQ^n / r_0^{3n+1}$. In our case, assume pump head is the sum of pressure loss ΔP and the lifting distance ΔZ: $H_p = \Delta P + \Delta Z$, then for a given pumping rate R, $Q \propto r_0^{3n+1/n} = r_0^{13}$. Data in Figure B-1 are not following this trend. Thus the differences in pumping capacity with different intake pipe sizes are not completely caused by the friction loss along the pipe.

In a circular pipe with a radius r_0, the velocity profile of a power law laminar fluid is given by

$$V = V_0\left(\frac{3n+1}{n+1}\right)\left[1-\left(\frac{r}{r_0}\right)^{n+1/n}\right] \tag{B-1}$$

where $V_0 = \frac{Q}{\pi r_0^2}$ is the mean velocity in the pipe. The shear rate across the pipe is

$$\dot{\gamma} = \frac{dV}{dr} = -\frac{V_0}{r_0}\left(\frac{3n+1}{n}\right)\cdot\left(\frac{r}{r_0}\right)^{1/n} \tag{B-2}$$

For a shear-thinning fluid, n < 1, so the maximum shear rate is at the wall of the pipe:

$$\dot{\gamma}_{max} = \frac{dV}{dr} = -\frac{Q}{\pi r_0^3}\left(\frac{3n+1}{n}\right) \tag{B-3}$$

which is proportional to $1/r_o^3$. Therefore, the shear rate along the pipe is very sensitive to the change in the pipe size. Small decreases in the size could result in dramatic rise of the flow shear rate.

Laponite gel is a type of thixotropic fluid, whose viscosity is also depending upon the shearing history of the flow besides the shear rate of the movement. When sheared under the same condition for certain time, the viscosity of the gel will decrease. Additionally, the more it has been sheared, the less viscous it would become. In a PCP system, if the Laponite gel has been intensely sheared before it entered the inlet of the pump, the viscosity of the gel is expected to decrease. A smaller intake pipe delivers a higher sheared flow, resulting in a less viscous flow entering the pump.

The actual flow rate Q_a induced by PCP at a pumping rate R, with a displacement q per rotation can be calculated by

$$Q_a = R \cdot q - S \qquad \text{(B-4)}$$

Empirically, volumetric slip (S) of PCP varies inversely with the viscosity of the fluid, which is $S \propto \frac{1}{\sqrt{\mu}}$ (Karassik *et al.* 2008). Under the same pumping rate, production is lower for pumping water than pumping gel, and a smaller intake pipe has lower capacity as shown in Figure B-1.

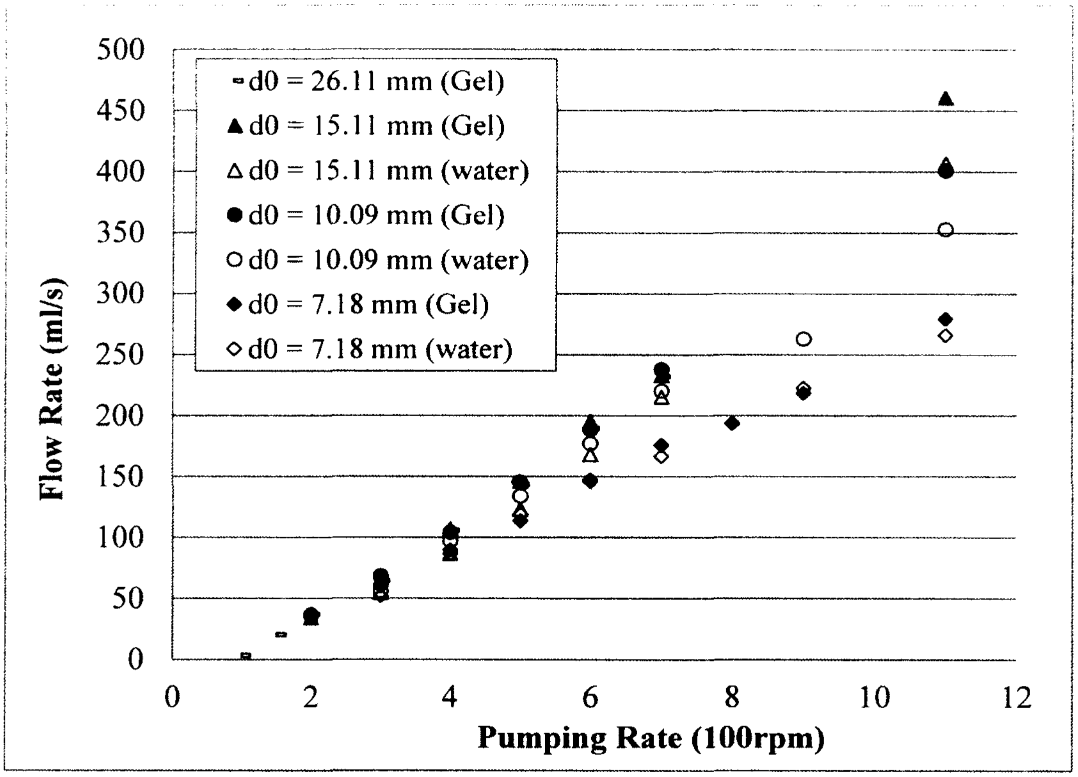

Figure B-1 Comparison Flow rate measurements of pumping water and pumping pre-mixed 3.0% Laponite by different sizes of intake pipes.

References

Karassik, I. J., Messina, J. P., Cooper, P., and Heald, C. C. (2008). *Pump handbook.* McGraw-Hill, New York.

Mitschka, P. (1982). "Simple conversion of Brookfield R.V.T. readings into viscosity functions." *Rheologica Acta,* 21(2), 207-209.

Paula, F. L. O., Silva, G. J. d., Aquino, R., Depeyrot, J., Fossum, J. O., Knudsen, K. D., Helgesen, G., and Tourinho, F. A. (2009). "Gravitational and magnetic separation in self-assembled clay-ferrofluid nanocomposites." *Brazilian Journal of Physics,* 39(1a), 163-170.

Zhou, D., and Yuan, H. (2008a). "Design of progressive cavity pump wells." 36-47.

Zhou, D., and Yuan, H. (2008b). "Slip calculation of rotational speed of electrical submersible progressive cavity pumps." 12-20.